Fakultät für Medizin

Image Quality Improvement in Optoacoustic Tomography

Antonia Longo

Vollständiger Abdruck der von der Fakultät für Medizin der Technischen Universität München zur Erlangung des akademischen Grades einer Doktorin der Naturwissenschaften genehmigten Dissertation.

Vorsitz: Prof. Dr. Marcus Makowski

Prüfer*innen der Dissertation:

1. Prof. Dr. Vasilis Ntziachristos
2. Prof. Dr. Björn Menze

Die Dissertation wurde am 18.01.2022 bei der Technischen Universität München eingereicht und durch die Fakultät für Medizin am 07.06.2022 angenommen.

Technische Universität München

Fakultät für Medizin

Lehrstuhl für Biologische Bildgebung

Image Quality Improvement in Optoacoustic Tomography

Antonia Longo

Dedicated to my parents,

Olga and Remo.

Abstract

Optoacoustic (OA) imaging is an emerging medical imaging modality that uses pulsed light excitation and ultrasound detection to visualize biological tissues with excellent optical contrast and high resolution at penetration depths far exceeding that allowed by optical detection. As such, OA imaging affords unique anatomical, functional, and molecular contrast compared to other medical imaging modalities.

Over the last two decades, advancements in OA imaging technologies have enabled ever more preclinical and clinical applications.

Despite the significant advances, several factors may reduce the quality and information content of OA images, leading to suboptimal contrast and accuracy. For the translation of OA technologies into clinical practice, there is a strong demand for high-quality medical images that can support clinicians in the detection, diagnosis, and prediction of diseases as well as eventually in therapy guidance.

The aim of the work presented here is to define and develop standard enhancement techniques to improve image quality and amplify structures of interest in OA imaging, thus enabling the operator to detect anatomical features more easily.

Firstly, we propose a new transducer design that incorporate an optical coating to accurately detect the broadband OA signals and increase image signal-to-noise ratio (SNR) and penetration depth in clinical OA systems. Secondly, we develop an automatic motion correction algorithm to address image quality degradation in OA imaging introduced by *in vivo* physiological movements, in particular breathing motion in living mice. Finally, we introduce frequency-band model-based (fbMB) reconstruction as a framework to untangle frequency components in OA and generate images with scale-specific contrast, thereby enabling structures of all sizes to be rendered with high fidelity. The effectiveness of the proposed methods to enhance image contrast and visualization is demonstrated in both phantoms as well as *in vivo* preclinical and clinical OA images. We discuss and present the challenges of developing standard methods to assess the biological accuracy of image improvement tools for *in vivo* OA applications.

By combining instrumentation development with new image processing tools, we produce OA images with improved contrast and fidelity, which reveal anatomical structures *in vivo* with

unprecedented detail. These image quality improvements ultimately broaden the biological applications of OA imaging techniques.

Our advancements in signal detection, motion correction, and image reconstruction also allow further enhancements in spectral unmixing and quantification in OA imaging, thus demonstrating the strong interconnection between visual perception and quantification accuracy.

In conclusion, the developed tools represent a valuable method of choice for image quality enhancement in OA imaging. The improved image visualization and interpretation of OA images will support the translation of OA technologies from laboratories to the clinics.

Contents

1 Introduction

1.1 Image quality improvement in medical imaging and its clinical relevance

The field of medical imaging has rapidly expanded over the past decades and is beginning to establish itself in the clinical practice due to the increased clinically relevant information that can be extracted from digital medical imaging.

In the late 16th century, medical imaging made its first great advancement with the invention of the microscope, which would eventually enable visualization of a human cell for the first time a century later. However, only in the 19th century the invention of X-rays enabled scientists to see inside the human body. Yet, the interest of imaging soft tissues, which is not possible with X-rays, led in the 1950s the development of ultrasound technologies. Simultaneously, the invention of tomographic techniques such as CT and PET allowed scientists to retrieve 3D images of different anatomical sections. Later, the concern on patient's exposure to ionizing radiation enabled MRI to rapidly establish for imaging soft tissue and organs.

What has driven the translation of these medical imaging methods from research labs to the clinics is the tremendous improvement in the image quality. This is largely due to the progress in the basic research and the underlying technologies, which has led physicians to better visualize the structures of interest in the patient body.

Image visualization still plays a crucial role in research, diagnosis, monitoring, and treatment of medical diseases in the clinical practice. In fact, major improvements image quality can be seen as the initial trigger for clinical translation of these imaging technologies, and ongoing efforts to improve image quality remain a hot topic in the medical field.

Therefore, enabling physicians to recognize anatomical structures of interest with high accuracy and details can advance diagnostic accuracy and detectability as well as ultimately improve the healthcare outcomes for patients.

Several factors still affect the quality and the information content of biomedical imaging, and image degradation results from the interplay between different sources.

Image degradation processes include, but are not limited to, the basic physics of image formation, the maximum permissible exposure of the patient and safety concern, the image formation chain from signal detection to image reconstruction, the system operation, and finally the position of the organ of interest. A good knowledge of these sources, as well as the quantification of their impact on image accuracy, is essential to drive the development of new systems and new image processing techniques for image enhancement.

An inherent challenge is that image quality in medical imaging is assessed by human observation in a subjective manner, which is based on personal perception and experience. Therefore, a key goal is to develop standard methods to enhance image quality and assure that the objective assessment is consistent with the subjective assessment.

1.2 Image quality improvement in optoacoustic tomography: opportunities and challenges

Within recent decades, optoacoustic (OA) imaging has emerged as the newest biomedical imaging approach. Preclinical and clinical applications of OA imaging are rapidly expanding due to the unique capability of the technology to visualize tissue optical contrast with high penetration depth and resolution, thus overcoming the limitation introduced by light scattering into tissue.

Advancements in basic research with the development of new dedicated technologies has allowed OA imaging to become a six-dimension[1] imaging modality that provides a unique anatomical, function and molecular contrast compared to other medical imaging modalities (Fig. 1.1).

The employment of algebraic algorithms for tomographic image reconstruction combined with GPU-based processors has enabled accurate 2D and 3D image formation. The development of fast tunable lasers with high throughput data acquisition hardware has added the time dimensionality to optoacoustics and allowed real-time imaging of dynamic processes, including physiological and hemodynamic changes, or kinetics and biodistribution of contrast agents. The availability of

[1] The term dimension in this context is used to extend the three geometrical dimensions (3D) to the time dimension (4D), the optical wavelength dimension (5D), and the ultrasound frequency dimension (6D), with the latter enabling resolution of chromophores at multiple scales (i.e., physical sizes).

multiple wavelengths for tissue excitation as well as un-mixing algorithms has added the multispectral dimensionality to OA imaging so that biological chromophores can be resolved based on their absorption spectra. Finally, the development of dedicated broadband ultrasound transducers has permitted accurate detection of the rich OA frequency content in order to resolve biological structures of varying scales, ranging from centimeters to tens of microns in resolution.

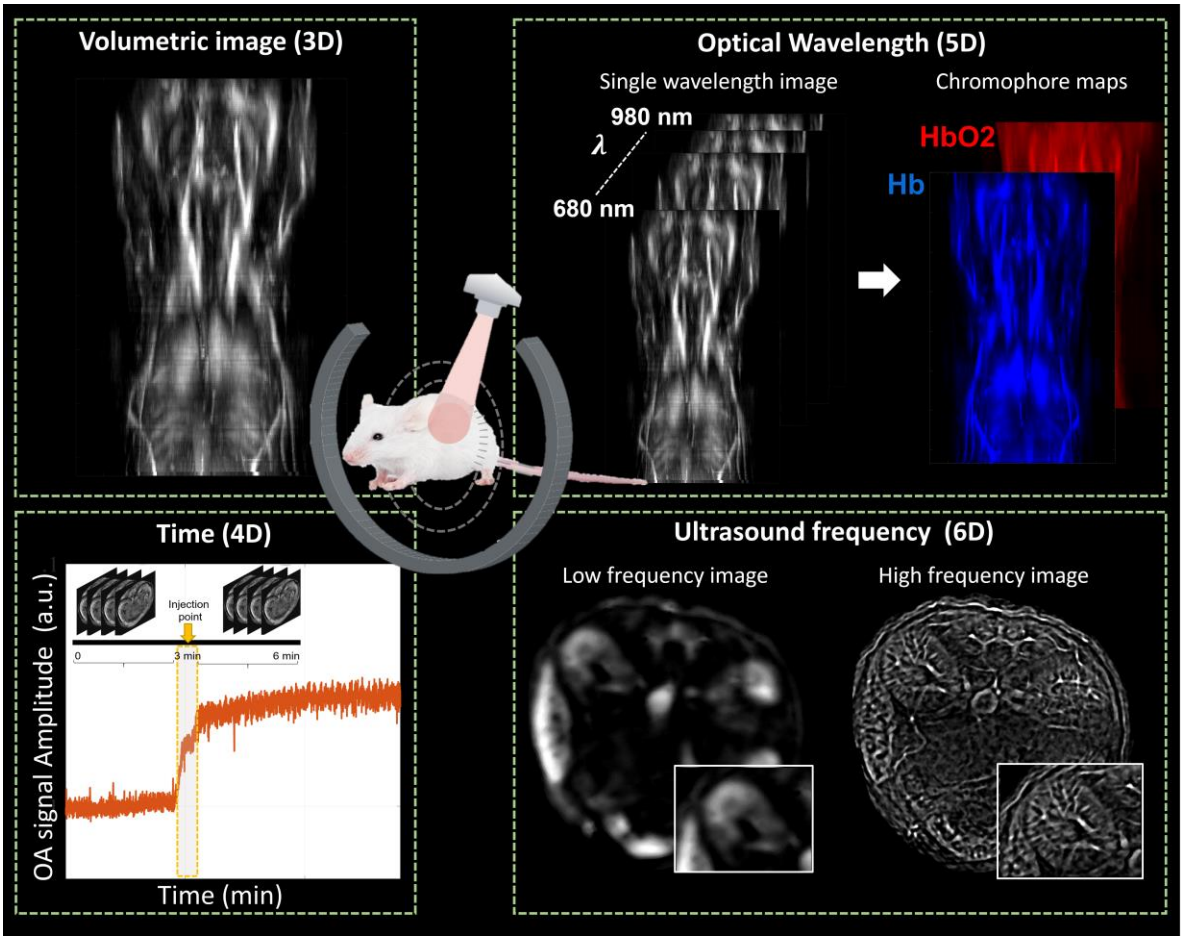

Figure 1.1. OA imaging as a six-dimensional imaging method for preclinical research. Volumetric imaging (3D) in real-time (Time, 4D) at multiple wavelengths (Wavelength, 5D) of structures with a wide range of scales (Frequency, 6D).

Despite the significant advances in the past two decades, several factors still contribute to degradation of image quality in OA imaging, leading to the acquisition of images with suboptimal contrast and fidelity.

OA images exhibit depth-dependent signal-to-noise ratio (SNR) primarily due to the attenuation of light as it propagates through tissue. At frequencies at the tens of MHz or higher, sound attenuation also contributes to signal loss with depth. Consequently, OA images are characterized by high signal intensity from superficial tissues that appear oversaturated and by lack of contrast and visibility of deeper structures.

Furthermore, OA signals have a broadband frequency content that encodes information about structures on different physical scales (i.e., size). These OA signals require specific methods and procedures to accurately capture, process and render the rich information content. Indeed, the power of the OA signals scales with the size of the structures being imaged, resulting in a frequency-dependent SNR and images where small structures may be obscured by the high SNR of low frequency contributions. Therefore, processing and rendering all frequencies together bias the visual perception of an image towards larger structures and often fail to accurately visualize small anatomical details.

Additionally, further degradation factors in OA imaging may arise from the specific imaged tissue and its localization, from *in vivo* physiology, as well as from the operation of the imaging system, which requires expertise and well-trained users.

Ongoing research in Multispectral Optoacoustic Tomography (MSOT) currently focuses on technology advancement, image processing, reconstruction algorithms, light fluence correction and un-mixing detection algorithms to resolve molecular targets. Although the progress in these fields strongly affects the final image quality, substantially less effort has been spent in image enhancement and improved visualization. A lingering challenge in preclinical and clinical MSOT is the lack of tools that allow operators to increase image contrast and then amplify structures of interest – which would allow operators to detect the features of interest for diagnosis more easily.

Image quality improvement is essential to enable high-fidelity information extraction from MSOT images. Since image visualization pays a critical role in disease diagnosis and treatment, improving image quality in OA is an essential goal for the translation of this technique into clinical practice.

1.3 Thesis objectives

The objectives of this work can be summarized as follows:

(1) Defining and developing standard methods to improve image quality while assuring biological accuracy in OA imaging.

The novelty of the current work is to provide image enhancement approaches that improve the signal detection accuracy by leveraging the physics of the OA signal and overcome the *in vivo* imaging challenges to enhance OA image quality. To reach this objective, we propose different improvement methods that tackle the OA imaging formation chain at different levels: OA signal detection, OA image reconstruction, and OA *in vivo* imaging.

First, we propose a new transducer design to reduce noise and improve OA signal detection accuracy. The aim is to increase image SNR, contrast, and penetration depth in clinical OA images.

Next, we address image degradation and quantification issues intrinsically related to physiological variability during *in vivo* imaging by proposing a new automatic breathing correction algorithm.

Finally, we develop a new reconstruction framework that exploits the physics of the OA signal (broadband frequency content and multiscale information) to render the rich OA information content with high fidelity and contrast. The improved image reconstruction enables visualization of anatomical structures with unprecedented levels of detail. The implemented method represents the unique solution to the longstanding problem of rendering the broadband frequency content in OA imaging.

(2) Demonstrating the efficacy of the proposed methods to enhance OA image visualization in both OA phantoms and *in vivo* biological applications.

(3) Demonstrating that the achievement of OA image quality has the side benefit of also improving the image quantification.

(4) Providing a critical assessment of image quality enhancement algorithms. We develop a standard method for the *in vivo* validation of vasculature enhancement algorithms to evaluate their biological accuracy in OA imaging.

1.4 Thesis outline

The present work is structured into five chapters.

Chapter 2 provides the theoretical and technical background for OA imaging – from OA signal generation and propagation to image formation and quantification. Here, we also discuss general aspects of instrumentation and provide an overview of the existing commercially available OA systems used in the current dissertation, MSOT inVision 256-TF and MSOT Acuity Echo (iThera Medical GmbH, Germany). The aim of the chapter is to introduce the reader to the topic and provide them with the necessary background for the subsequent chapters.

Chapter 3 presents and discusses different image degradation processes in OA, which involve each step of the imaging chain, from the physics of the OA signal to the instrumentation and image formation. Degradation factors related to the specific imaged tissue as well as from the operation of the imaging system are also discussed. This chapter describes original findings in OA imaging, and it is meant to provide a guide for *in vivo* clinical and preclinical imaging design and operation.

Chapter 4 presents novel image improvement approaches developed during the thesis. The effectiveness of the proposed methods towards the enhancement of image contrast and SNR while preserving biological accuracy in OA imaging is demonstrated and validated with both phantoms and different *in vivo* applications. The proposed techniques aim to establish standard methods for visual quality enhancement in OA tomography.

Chapter 5 discusses the challenges and implications of developing validation methods to assess image quality improvement tools and their accuracy in OA imaging. We propose a new *in vivo* validation method to evaluate the performance of the Hessian-Based Frangi vesselness filter, a post-processing algorithm used to enhance vasculature in OA imaging. We evaluate whether image enhancement is performed at the expense of biological fidelity. For the first time, we provide recommendations to ensure appropriate use of Frangi and other vessel enhancement filters to avoid misinterpretation of post-processed OA images.

Finally, Chapter 6 summarizes the main research contributions of this dissertation and provides an outlook onto future developments and directions in OA imaging to improve the clinical impact of OA technologies.

2 Theoretical and technical background

In this chapter, the underlying physics of OA imaging is presented, from OA signal generation and propagation to tomographic image formation and quantification. Technical aspects of OA imaging systems are also provided.

2.1 Optoacoustic principles

2.1.1 The optoacoustic effect

The optoacoustic (or photoacoustic) effect is based on the generation of acoustic waves following the absorption of ultrashort laser pulses. The optoacoustic phenomenon was first reported in the late 19th century by Alexander Graham Bell. However, due to the availability of commercial pulsed laser technologies in the nanosecond range and the development of wideband ultrasound detectors, application of this effect in the biomedical field has intensified only in the past two decades. OA imaging based on this phenomenon has demonstrated great potential to visualize living biological tissues in multiple preclinical applications, including cardiovascular disease research [1], neuroimaging [2], cancer [3, 4] and pharmacokinetics research [5]. Furthermore, the development of real-time hand-held imaging systems has enabled clinical use of optoacoustics [6] for breast imaging [7, 8], dermatological imaging [9-12], vasculature imaging [13, 14], musculoskeletal imaging [15, 16], gastrointestinal imaging [17, 18], endocrinology and metabolism imaging [19, 20] and endoscopy [21].

The schematic of an OA imaging system is shown in Fig. 2.1a. The tissue is illuminated with short laser pulses in the range of 10-100 ns. The absorbed light within the object is converted into heat, and the temperature rise leads to thermoelastic expansion, which is in turn followed by an increase in pressure. As a result of the increased pressure, broadband ultrasound waves are generated and can be detected with ultrasound transducers. The amplitude of the detected pressure waves reflects the local energy absorption inside the tissue. By tomographic detection and reconstruction, the distribution of the absorbers within the tissue can be estimated [22].

Of particular importance for biomedical applications is the use of multispectral excitation to resolve the different optical absorbers inside the tissue based on their unique spectral signature (Fig. 2.1b) by using different unmixing algorithms [23]. Multispectral optoacoustic tomography (MSOT) has been shown increased sensitivity in detecting chromophores of biological importance

compared to single wavelength methods [24, 25]. MSOT involves the illumination of the tissue at different wavelengths in the near infrared region (NIR) of the spectrum – a range of wavelengths over which hemoglobin absorption and tissue scattering is low compared to the UV (ultraviolet) and visible range – thus enabling deep light penetration at high spatial resolution [26]. Endogenous chromophores, such as hemoglobin, lipid, water, and melanin, provide strong optical contrast and enable extraction of functional and structural information from the imaged tissue. To further enhance OA contrast, several exogenous contrast agents based on organic (Indocyanine green-ICG, IRDye800, methylene blue), metallic, and inorganic (carbon nanotubes, quantum dots) small molecules and semiconducting nanoparticles have been introduced in OA imaging. This has allowed targeted molecular imaging, as could be used in drug delivery or therapy [27].

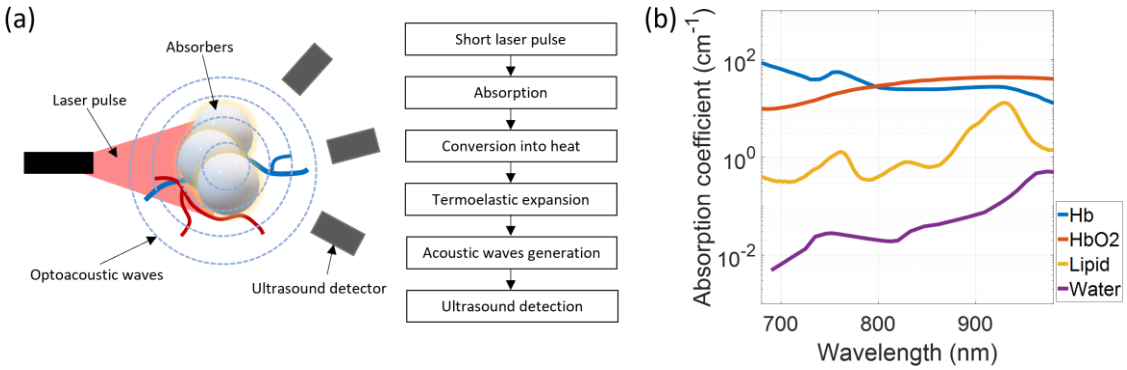

Figure 2.1. Schematic of OA imaging systems. (a) the laser pulse illuminates the sample, and the absorbed electromagnetic energy is converted into heat. Acoustic waves are generated due to thermoelastic expansion of the sample and detected with ultrasound sensors. (b) Absorption spectra of major endogenous contrast agents in biological tissue at normal concentrations (source: https://omlc.org/spectra/). Multiwavelength illumination as in Multispectral Optoacoustic Tomography (MSOT) can be used to resolve different absorbers based on their spectral characteristics with high sensitivity inside the imaged tissue.

2.1.2 OA signal generation and wave propagation

In OA imaging, a short laser pulse is typically used to excite the tissue, resulting in the generation of broadband OA waves that propagate and are detected by the ultrasonic transducer. There are two important time scales for OA signal generation: the thermal relaxation time and the stress relaxation time. If the duration of the laser pulse is shorter that the thermal relaxation time (i.e., the time that takes to the heat to diffuse to neighboring tissue) and stress relaxation time (i.e., the

time it takes for the OA waves to propagate) the laser excitation satisfies both thermal and stress confinements. Under these conditions, the relationship between the initial acoustic pressure distribution p_0 at a given position r in the tissue and the absorbed optical energy can be written as:

$$p_0(r) = \Gamma H_r(r) = \Gamma \mu_a(r) \Phi(r) \tag{2.1}$$

Where $\mu_a(r)$ is the optical absorption coefficient of the tissue (cm^{-1}) and $\Phi(r)$ is the local optical fluence (energy per surface, J/cm^2). Γ is a dimensionless parameter called the Grüneisen coefficient, which represents the conversion efficiency of heat to pressure within tissue [28].

After the generation of the initial pressure p_0, the acoustic waves propagate inside the material at the speed of sound of the medium. Under the hypothesis of acoustically homogeneous medium, the propagation of the induced pressure wave $p(r,t)$ is described by the wave equation [29]:

$$\frac{\partial^2 p(r,t)}{\partial t^2} - c^2 \nabla^2 p(\boldsymbol{r},t) = \Gamma \frac{\partial H(\mathrm{r},\mathrm{t})}{\partial t}, \tag{2.2}$$

where c is the speed of sound in the medium, Γ is the Grüneisen parameter, which is assumed constant, and H is the energy absorbed in tissue per unit volume and per unit time. In case of short-pulsed laser illumination, the temporal dependence of H can be approximated in the acoustic regime with a δ-distribution, so that $H(r,t) = H_r(t)\delta(t)$.

The solution of Eq. 2.2 can be described in terms of Green's function for the wave equation [28, 30]. Considering an object Ω as an OA source, the solution of the wave equation for object Ω can be estimated by assuming that each point $\boldsymbol{r'}$ of the object Ω is a source of OA waves, given by the following Green's function G:

$$G(\mathbf{r},\mathbf{r}',\mathrm{t}) = \frac{\delta\left(t - \frac{|\boldsymbol{r}-\boldsymbol{r}'|}{c}\right)}{4\pi|\boldsymbol{r}-\boldsymbol{r}'|}. \tag{2.3}$$

Eq. 2.3 represents the elementary wave generated at $\boldsymbol{r'}$ at t=0, propagating outwards in a spherical shell. The solution to Eq. 2.3 at a given point $\boldsymbol{r}$ can be written as:

$$p(\mathbf{r},\mathrm{t}) = \frac{\Gamma}{4\pi c^2}\frac{\partial}{\partial t}\left[\int_{\Omega} H_r(\mathbf{r}')\frac{\delta\left(t-\frac{|\boldsymbol{r}-\boldsymbol{r}'|}{c}\right)}{|\boldsymbol{r}-\boldsymbol{r}'|}d\mathbf{r}'\right], \tag{2.4}$$

where the integral is estimated along the whole object. Eq. 2.4 represents the Huygens Principle for OA, since it describes the OA pressure field generated by a source Ω at point $\boldsymbol{r}$ as a superimposition of elementary waves generated at points $\mathbf{r}'$ on the source.

2.1.3 Acoustic wave propagation related phenomena

The generated acoustic waves propagate through and interact with tissue. Biological tissues are heterogeneous viscoelastic solids with complicated structures that support many different types of acoustic waves (i.e., Compression waves, Shear waves, Reyleigh waves, Lanb waves, etc.) and acoustic propagating phenomena (i.e., reflection, refraction, dispersion, diffraction, scattering, mode conversion, etc.) [31]. However, for the sake of simplification, since tissue has a high-water content, the wave propagation in liquid is often considered. Under this approximation, four main acoustic phenomena correlated with the wave propagation inside the tissue can be considered: acoustic reflection and refraction at the boundaries between two media; acoustic dispersion; and attenuation.

<u>Acoustic reflection and refraction</u>

Acoustic reflection and refraction occur at the interface between two media with different acoustic properties. Reflection occurs for all incident angles and generates reflected waves in the first medium. Refraction takes place when the incident wave encounters a boundary at the interface of two media with a certain angle and result in a change in the trajectory in the second medium. Fig. 2.2 reports a schematic of acoustic reflection and refraction at the interface between two liquid media.

Reflection and refraction depend on the acoustic impedance of the medium, which is defined as $Z = \rho c$, with ρ and c representing the density and the speed of sound of the medium, respectively. Z is measured in Rayls ($Pa \cdot s \cdot m^{-1}$) and is in the order of 10^6 Rayls for water and biological tissue.

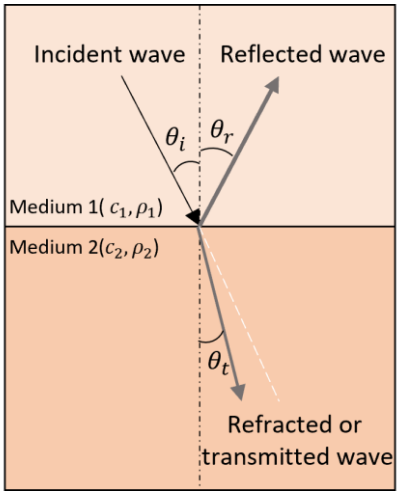

Figure 2.2. Schematic of acoustic reflection and refraction at the interface between two liquid media.

Reflection between two media is described by the law of reflection, which states that the angle of incident wave θ_i equals the angle of reflection θ_r:

$$\theta_i = \theta_r \tag{2.5}$$

Refraction between layers of different acoustic impedance is described by Snell's law, which is given by:

$$\frac{\sin(\theta_i)}{\sin(\theta_d)} = \frac{c_1}{c_2} = n \tag{2.6}$$

Or

$$\theta_t = \arcsin\left(\frac{c_2}{c_1}\sin\theta_i\right) \tag{2.7}$$

Where θ_i and θ_t are the angle of incidence and the angle of refraction. In biological tissue, the refraction index n~1, and therefore acoustic refraction in OA imaging is usually neglected by assuming forward propagation of sound waves in tissue [32].

In the case of a normally incident wave in the interface between two media, the amount of energy reflected and transmitted as a percentage of the original energy is expressed as:

$$R = \left(\frac{Z_2 - Z_1}{Z_2 + Z_1}\right)^2 \tag{2.8}$$

And

$$T = \frac{4Z_1Z_2}{(Z_2 + Z_1)^2} \tag{2.9}$$

For high acoustic impedance mismatch between tissues, a large amount of energy is reflected, while a limited amount is transmitted in the second medium. In biological tissue, acoustic reflection can occur at different interfaces, i.e., between skin and the outside of the body, between soft tissue and bone, and between surrounding tissues and the lungs. While acoustic impedance mismatch and reflection phenomena are the key mechanisms of contrast in ultrasound imaging, in OA imaging, they result in image artifacts. These artifacts can mislead quantification and interpretation and compromise image penetration depth. This effect will be discussed in detail in Sec. 3.4.2

Acoustic attenuation and dispersion

Due to the viscoelastic properties of biological tissue, acoustic waves propagating in tissue are subject to attenuation and distortion. The acoustic attenuation can be described by the equation [33]:

$$p(r) = p_0 e^{-\alpha(f)r} \tag{2.10}$$

with the initial pressure distribution p_0, the propagation distance in cm *r*, and the attenuation coefficient $\alpha(f) = \alpha_{0f}|f|^n$ $(dBcm^{-1})$, which has a power-low dependence with the frequency. In biological tissue, n has typical values ranging between 1 and 2, and α_{0f}~0.5 $dB\ MHz^{-1}\ cm^{-1}$ in the frequency range of ultrasonic imaging [33].

As a result of the frequency-dependent attenuation, acoustic waves not only decrease in amplitude as they propagate inside the medium, but their wavefronts are also distorted. Due to acoustic dispersion, the frequencies are attenuated differently, and the detected time domain signal after wave propagation results broaden leading to a loss of resolution.

Nevertheless, in OA macroscopy where frequencies below 20 MHz are considered the acoustic attenuation can be neglected. At these frequencies, the optical attenuation in the tissue is stronger

and the signal distortion introduced by the transducer properties is generally predominant compared to acoustic attenuation. This topic will be further discussed in Sec. 2.2.2.5.

2.1.4 Acoustic and optical inverse problem

The challenge in OA imaging is to retrieve the optical absorption distribution μ_a in the tissue from the measured acoustic pressure $p(r,t)$ at all detectors. The inverse problem from measured OA signal to absorbers can be separated into two parts: the acoustic inverse problem, which tackles the propagation and detection of the generated acoustic waves, and the optical inverse problem, which relates to the light propagation inside the tissue.

In the acoustic inversion problem, the initial pressure distribution p_0 is retrieved from Eq. 2.4 and the relation $p_0 = \Gamma H_r$; in the optical inversion problem, the absorption coefficient μ_a is estimated from the initial pressure $p_0 = \Gamma \mu_a \Phi$, Eq. 2.1.While the former is a linear inverse problem, the latter is a highly complex nonlinear problem due to the fluence, which is unknown and depends on the distribution of both scattering and absorption coefficients in the tissue, $\Phi(r, \lambda; \mu_a, \mu_s)$ [34].

From an imaging perspective, the resolution of the acoustic invers problem is relevant in reconstructing the OA image from the measured acoustic signal, whereas the resolution of the optical invers problem is related to the quantification of different chromophores inside the tissue.

2.2 Tomographic OA imaging

2.2.1 OA sources in tomography

2.2.1.1 Time and frequency domain characteristics

The analytical solution of the OA wave equation (Eq. 2.4) for uniformly illuminated spheres of different sizes is reported in [28] and illustrates the most important features of OA signals. Fig. 2.3 reports the characteristics of the simulated OA signal for three spheres with radii of 480, 280, and 120 μm.

First, the OA signal has a characteristic bipolar shape due to thermoelastic expansion (Fig. 2.3b), i.e., pressure rise due to compression (positive peak) followed by pressure drop due to rarefaction (negative peak). Second, the amplitude of the OA waves is directly proportional to the size (i.e., physical scale) of the object so that small-scale features have lower SNR compared to large-scale features (scale-dependent SNR). Third, due to pulsed laser excitation, the spectrum of the OA

signal is broadband, with peak emission frequency and bandwidth inversely proportional to the source size (Fig. 2.3c). Thus, the frequency content of small absorbers is more shifted towards the high frequencies, which requires the use of high frequency sensors to resolve them.

Notably, the emission spectra of objects of different sizes located in the same field of view overlap (frequency spectra entanglement) due to the linearity of Eq. 2.4.

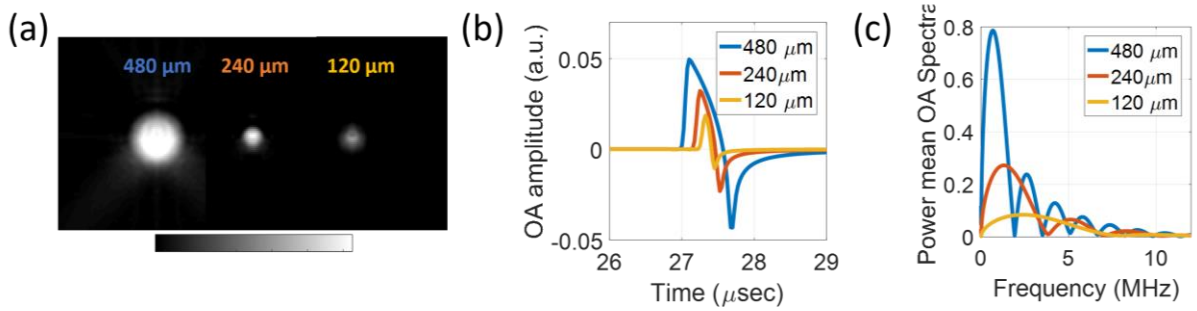

Figure 2.3. Time and frequency domain characteristics of OA signal. (a) Uniformly illuminated absorbing spheres of varying sizes, 480, 280 and 120 µm. Generated OA signal in (b) time and (c) frequency domain.

These general characteristics of the OA signals, in particular scale-dependent SNR and frequency entanglement, pose two challenges in OA imaging: resolving small absorbers from large absorbing structures and disentangling the different OA scales in the signal domain. These effects will be discussed in Sec. 4.3.

2.2.1.2 Directivity

The pressure wave generated from a point-like OA source is coherent and propagates following a spherical wavefront. However, diffraction phenomena arise from the interference between wavefronts from neighboring point-like sources [35]. Therefore, the shape, the orientation, and the aspect ratio of the OA absorber, which consists of different point-like sources, affect the directivity pattern of the generated acoustic waves.

Fig. 2.4 reports the polar plot of the emitted energy from OA sources with varying aspect ratios of 1 (S1) and 5 (S2) located in the center of the field of view at 10-, 40- and 60-mm distance Notably, the directivity of the generated acoustic waves increases with the increasing object aspect ratio and

for larger distance. While objects with aspect ratio 1 emit a characteristic spherical wave, objects with high aspect ratio emit in a directive radiation pattern.

In *in vivo* imaging, due to the high structural complexity of the absorbers present in the image field of view, the OA signals are emitted in all directions. Therefore, an enclosed detection surface is required to accurately acquire the entire OA signal and avoid structures to be distorted or invisible in the final image. This is known as the limited-view problem in OA imaging and will be discussed in Sec. 3.3.6.

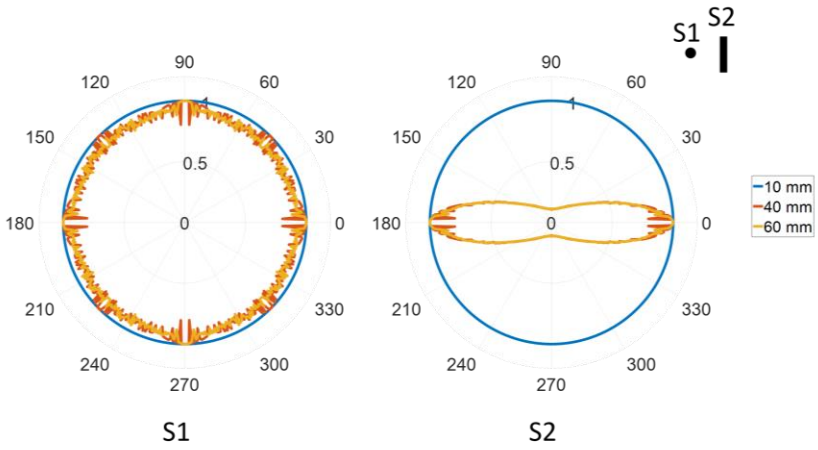

Figure 2.4. Directivity pattern of the OA signals generated from absorbing objects of different aspect ratio: a spherical OA source with aspect ratio 1 (S1) and a vessel-like OA source with aspect ratio 5 (S2). The OA sources are in the center of the field of view and the directivity pattern is reported at 10-, 40- and 60-mm distance from the objects.

2.2.2 Technical aspects of OA tomographic systems

2.2.2.1 Laser technologies

To efficiently generate OA signals, the pulse duration of the laser employed must be on the nanosecond scale. Furthermore, high energy and high repetition rate lasers are necessary for good OA SNR and real-time functional imaging. For these reasons, Q-switched solid-state lasers based on neodymium-doped laser crystals, e.g., Nd:YAG, are usually employed in OA imaging, with optical parametric oscillators (OPOs) as conversion stages for wavelength tuning in the NIR region. The OPO technology can offer several hundreds of millijoules energy per-pulse and fast wavelength switching, thus enabling good image SNR at high penetration depth and fast-scanning imaging [35].

2.2.2.2 Maximum permissible exposure

To guarantee safe OA application in living subject, the maximum permissible exposure of human subjects to lasers is regulated by the safety standards set by the American National Standards Institute (ANSI) [36]. The ANSI laser safety limits depend on the pulse duration, optical wavelength, and exposure duration. The maximal permissible skin exposure (MPE) for a nanosecond laser up to a repetition rate of 10 Hz in the NIR region (700-1050nm) is expressed as [37]:

$$MPE^{(1)}(mJcm^{-2}) = 20mJcm^{-2}10^{2(\lambda-700nm)/1000nm} \quad (2.11)$$

$$MPE^{(3)}(mWcm^{-2}) = 200mWcm^{-2}10^{2(\lambda-700nm)/1000nm} \quad (2.12)$$

and depends on both the energy per pulse $MPE^{(1)}$and the averaged power $MPE^{(3)}$. At 700 mm for 10 Hz repetition laser, the maximum pulse energy is set to 20mJ, and the averaged power is limited to 200 mW.

2.2.2.3 Optoacoustic signal detection

The detection of OA waves is the critical component in OA imaging systems. For accurate acquisition, the detection device requires a broad detection bandwidth from kHz to hundreds of MHz, a detection sensitivity in range of Pa and sub-Pa [38-40] and a collection of data from an enclosed detection surface, i.e., tomographic acquisition. Despite all the ongoing development on optical sound detection [38] as well as on PMUTs [41] and CMUTs [42] detectors, a piezoelectric transducer array remains the most used technology for real-time OA tomographic imaging. These detectors are based on the piezoelectric effect, a physical principle in which an electric voltage is detected in response to an applied mechanical strain, and vice versa.

Fig. 2.5a reports a schematic of a single piezoelectric transducer. The piezoelectric material is sandwiched between two electrodes to measure the generated electric voltage. The thickness and the speed of sound of the piezoelectric material determine the central frequency of the transducer. Generally, a matching layer with specific characteristics – a thickness of ¼ wavelength λ and acoustic impedance with intermediate value between that of the tissue and piezoelectric material – is placed in front of the active element to reduce the impedance mismatch and maximize the acoustic transmission from the tissue to the active element. For a transducer with a single matching layer, the optimal acoustic impedance is given by $Z_{ML} = \sqrt{Z_0 Z_T}$, with acoustic impedances of the piezoelectric material Z_0 and of the tissue Z_T. A backing material is placed in the back of the active

element to attenuate the acoustic reverberations generated from the reflected waves, which cause ripples in the detected signal and result in a loss in resolution. Although the backing material enables broadband signal detection, the strong attenuation effect is responsible of loss in detection sensitivity.

The electroacoustic behavior of a transducer can be described as a three-port network following the Krimholtz, Leedom and Matthaei (KLM) model reported in Fig. 2.5b. The piezoelectric element is connected to the backing (B) and to the receiver electronics (R), represented as loadings in terms of their electrical impedances Z_B and Z_R respectively, and to the medium (M) which is represented as a voltage source V_M in series with an impedance Z_M . The piezoelectric element can be assumed as a resonator with a first harmonic given by the vibration frequency $f_r = c_{pz}/2d$, which depend on both speed of sound (c_{pz}) and thickness (d) of the piezoelement.

Among all piezoelectric materials, piezo-composite materials [43], which usually consist of piezoelectric ceramic inside an electrically isolating polymer matrix (typically epoxy), have the advantage of providing some flexibility to the transducer. This results in an easier production of different sensor shapes. Several types of piezocomposites have been investigated, but today, the 1-3 type piezocomposite is mostly used to build ultrasound probes [44].

One of the main limitations of commercially available piezoelectric transducers for OA applications is that they are usually opaque and interfere with the illumination required in the OA setups. The effect of the interference between transducers and pulsed light will be extensively discussed in Sec. 4.1.

Detector electrical impulse response

OA signal is broadband and comes with a rich frequency content due to the ultra-short illumination pulses. Advanced OA systems use broadband acoustic detectors to ensure that no structural information is lost.

The electrical impulse response of the acoustic detectors, i.e., central frequency and bandwidth, is a crucial parameter for OA imaging systems, as this determines the maximum achievable resolution and penetration depth and ultimately the intended biological and clinical applications.

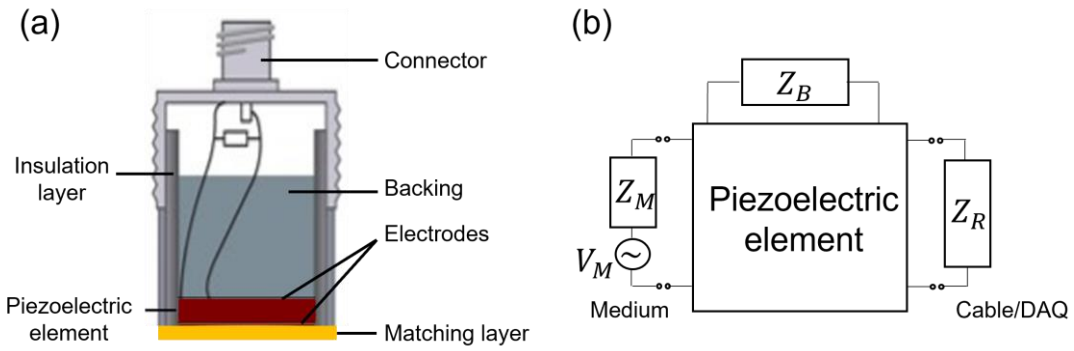

Figure 2.5. OA signal detection. (a) Schematic of the piezoelectric transducer and (b) equivalent three-ports circuit based on the KLM model.

For example, in OA microscopy and mesoscopy, where optical absorbers between 10 and 300 um resolutions are of interest, detectors with a frequency response between a few MHz and 150 MHz are employed [45], albeit at reduced image penetration depth of 1-10 mm. Alternatively, detectors with a central frequency of 4-5 MHz and 100% bandwidth are used for deep tissue imaging in OA macroscopy, thus enabling researchers to image structures from centimeters to hundred-microns resolution up to 3 cm penetration depth.

The electrical impulse response of the transducer acts as a band pass filter on the detected OA signal and can be modeled with a convolution:

$$p_d(r,t) = p(r,t) * EIR(t) \tag{2.13}$$

where EIR (t) represents the electrical impulse response of the detection system in time, which is spatially invariant and independent from the source. By tuning the piezo element, the matching layer, the backing material as well as the electronics of acquisition, a broader acquisition bandwidth can be achieved.

Detector sensitivity field

Focused detectors are usually employed in OA imaging due to their ability to focus higher sensitivity in a small region in the field of view, called focal zone. In OA macroscopy, cylindrically focused transducers (Fig. 2.6a) are favored since this geometry enables signal detection from a wide reception angle in the image plane and rejects out-of-plane signal [46-48]. Fig. 2.6 reports the sensitivity field from a clinically focused transducer in the elevational direction YZ orthogonal

to the image plane XY (Fig. 2.6b) and in the image plane XY (Fig. 2.6c). The sensitivity field of a detector is obtained by plotting the energy of the detected OA signal generated from a point source located in different positions in the space. The -6dB curve of the sensitivity field in the image plane XY defines the image field of view, while the width of the focal zone in the elevational direction YZ determines the slice thickness.

For a cylindrically focused transducer, a formula to estimate the width (FWHM z in Fig. 2.6 b) and the length (FWHM y in Fig. 2.6b) of the sensitivity field is derived by [49]:

$$width = \frac{1.1c_s}{f_c(1-\cos(\theta/2))} \tag{2.14}$$

And

$$length = \frac{0.5c_s}{f_c \sin(\theta/2)} \tag{2.15}$$

With c_s the speed of sound in the medium and θ the detector aperture (Fig. 2.6a).

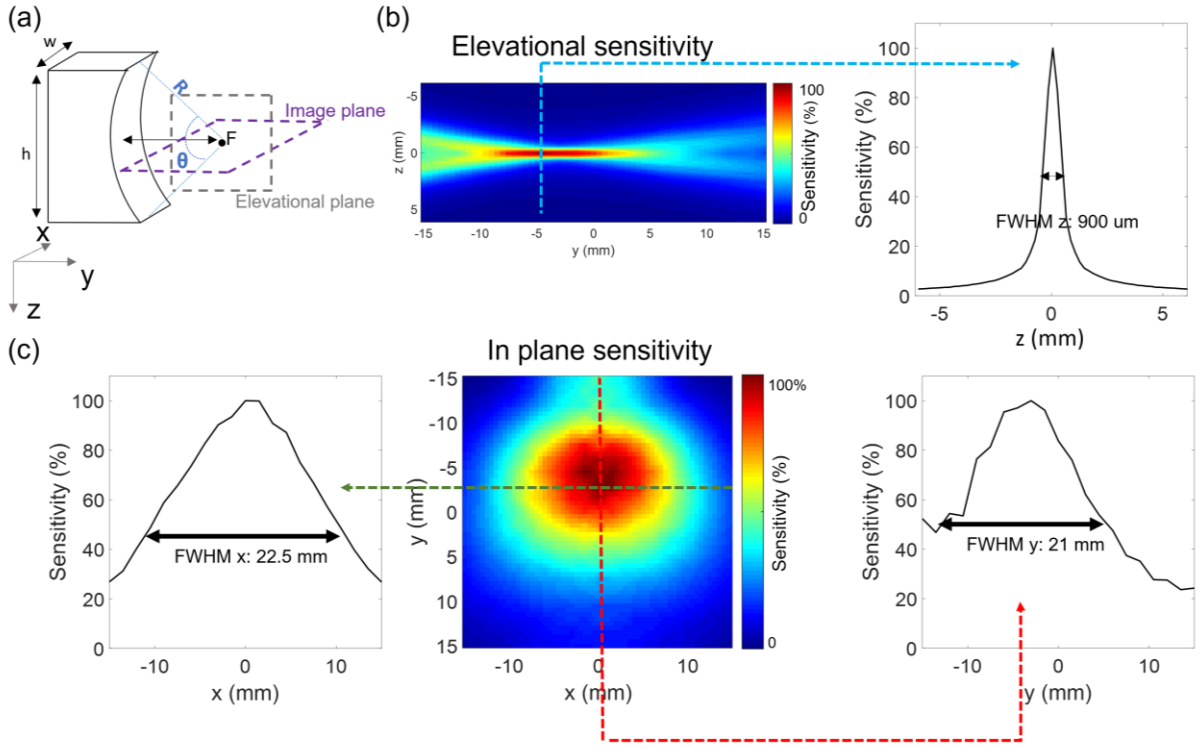

Figure 2.6. Sensitivity field of a cylindrically focused transducer. (a) Cylindrically focused transducer with elevational direction radius R, imaging plane radius F, element width w, element length (elevational height) h and element aperture θ. Sensitivity field in (b) elevational plane YZ and (c) image plane XY for a detector with w=0.725 mm, h=15 mm, F=40 mm and R=37 mm.

From Eq. 2.14 and Eq. 2.15, the dimension of the image field of view and the focal zone is in general given by the transducer shape and frequency. The smaller the transducer aperture or the higher the frequency of the signal, the higher the achievable resolution and penetration depth.
It is common practice to select transducers based on their sensitivity at the central frequency. However, the signal acquired in OA imaging is broadband, and due to the frequency-dependent sensitivity field, at low frequencies the transducer is sensitive to an amount of out-of-plane signal. The detected out-of-plane signal can introduces distortions in OA images. This effect will be discussed in detail in Sec. 3.3.4.

Detector spatial impulse response

Detectors with big element sizes are preferrable in OA imaging, as they provide higher SNR due to the larger sensitivity area. However, the use of larger detectors introduce distortion in the recorded OA signal since different points of the detector surface detect the signal at different time points according to the distance to the source.

Mathematically, this can be expressed as a spatial averaging of the OA signals acquired from the single point source $\boldsymbol{r'_d}$ over the surface S of the detector [49, 50]:

$$p_d(t) = \int_s p(\boldsymbol{r'_d}, t) dS(\boldsymbol{r'_d}) \tag{2.16}$$

For an OA point source $p_{ps}(\boldsymbol{r'_d}, \boldsymbol{r}, t)$ located at position $\boldsymbol{r}$, the integral in Eq.2.16 can be written as a 1D convolution, following [50]:

$$\int_s p_{ps}(\boldsymbol{r'_d}, \boldsymbol{r}, t) dS(\boldsymbol{r'_d}) = SIR(\boldsymbol{r'_d}, \boldsymbol{r}, t) * p_{ps}(\boldsymbol{r_d}, \boldsymbol{r}, t) \tag{2.17}$$

Where:

$$SIR(\boldsymbol{r'_d}, \boldsymbol{r}, t) = \frac{1}{2\pi} \int_S \frac{\delta(t - \frac{|\boldsymbol{r'_d} - \boldsymbol{r}|}{c_s})}{|\boldsymbol{r'_d} - \boldsymbol{r}|} dS(\boldsymbol{r'_d}) \tag{2.18}$$

is the spatial impulse response of the transducer element located at $\boldsymbol{r_d}$, which is time and spatially variant.

Fig. 2.7 shows the distortion introduced by the detector's spatial impulse response on OA signal detection for absorbing microspheres located in different positions of the field of view. A cylindrically focused transducer (40 mm element curvature, 37 mm elevational radius, and 128

elements with 0.735 mm x 15 mm single element size) is considered, and the position of the four microspheres relative to the focal point of the transducer are reported in Fig. 2.7a. For a source located in the focal point of the transducer (P1), the acoustic signal is detected at each surface point of the transducer at the same time and the spatial impulse response is a delta function, thus the the final measured pressure signal is accurately detected. For sources located out of the detector focus (P2 in the image plane, P3 and P4 in the image out-of-plane in Fig. 2.7b), the detected signals are broadened and distorted due to the different time of arrival at each surface point, thus leading to a reduction in the image resolution which increases with the distance from the center of detection.

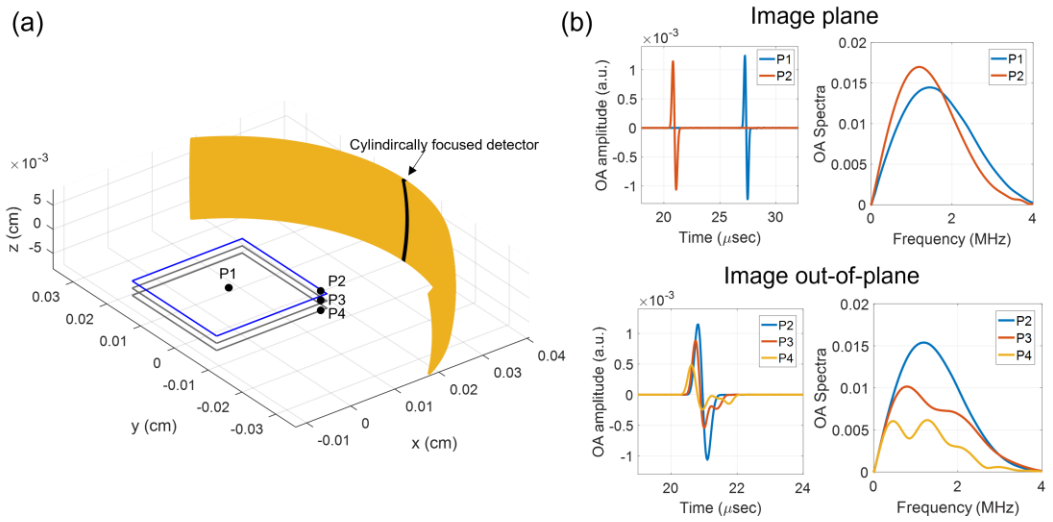

Figure 2.7. Detector spatial impulse response and signal distortion. (a) Schematic of a curved array of cylindrically focused detectors (40 mm element curvature, 37 mm elevational radius, and 128 elements with 0.735 mm x 15 mm single element size) and OA sources (microspheres) located in different positions P of the field of view. (b) OA signals in time and frequency domain for sources located in the image plane (P1 Vs P2) (top) and out-of-plane (P2 Vs P3 vs P4) (bottom).

The image quality degradation in *in vivo* OA images introduced by the finite size of the detector, i.e., spatial impulse response, will be further discussed in Sec. 3.3.2.

The convolution between the electrical impulse response (EIR) and the spatial impulse response of the transducer is termed total impulse response (TIR). The detected OA signal from a band-limited finite-size detector can be written as:

$$p_d(r,t) = p(r,t) * TIR(r,t) = p(r,t) * EIR(t) * SIR(r,t) \qquad (2.19)$$

2.2.2.4 Spatial resolution

The spatial resolution of an OA imaging system is primarily determined by the detector frequency and bandwidth. However, additional factors contribute to limiting the maximum achievable resolution, such as the detector size and shape, and the laser pulse duration.

In-plane image resolution

The in-plane image resolution refers to the minimum size of the absorber that can be resolved in the image field of view and is determined by the axial and lateral resolution (Fig. 2.8a).

The axial resolution of an OA imaging system is the resolution along the acoustic axis of the transducer and depends only on the transducer frequency bandwidth. The lateral resolution refers to the resolution perpendicular to the acoustic axis of the detector and depends on both transducer frequency bandwidth and transducer element size.

Under the hypothesis of full view detection, point detectors, continuous spatial sampling, and constant speed of sound, the expression to estimate the axial resolution is given by [51]:

$$R_{bw} \approx 0.8 c_s / f_{co} \tag{2.20}$$

where c_s is the speed of sound and f_{co} is the cutoff frequency of the transducer. The axial resolution is space invariant.

For a circular scanning geometry with a detector with identical curvature properties as the detection surface, the lateral resolution of an OA imaging system can be written as [51, 52]:

$$R_{lat}(r) = \sqrt{{R_{bw}}^2 + R_{ap}(r)^2} \tag{2.21}$$

Where R_{bw} is the axial resolution and R_{ap} is the aperture resolution defined as:

$$R_{ap}(r) \approx \frac{r}{r_o} D \tag{2.22}$$

with *r* the distance between the point source and the center of the scan geometry *r*, r_o the radius of the scan area and D the dimension of the detector.

Fig. 2.8b reports the in-plane image resolution for a cylindrically focused transducer with element size of 0.735 mm x 15 mm, 40 mm element curvature and 37 mm elevational radius. Notably, the

lateral resolution is spatial variant, has its minimum in the center of rotation of the transducer array ($R_{lat}(r) = R_{bw}$), and degrades for OA sources located far from the center of detection.

Elevational resolution

The elevational resolution of an OA imaging system refers to the thickness of the two-dimensional section captured in the transducer elevational direction. It is defined as the full width at half maximum (FWHM) of the detector sensitivity in the elevation direction orthogonal to the image plane. Fig. 2.8c reports the elevational resolution map for a cylindrically focused transducer with element size of 0.735 mm x 15 mm, 40 mm element curvature and 37 mm elevational radius.

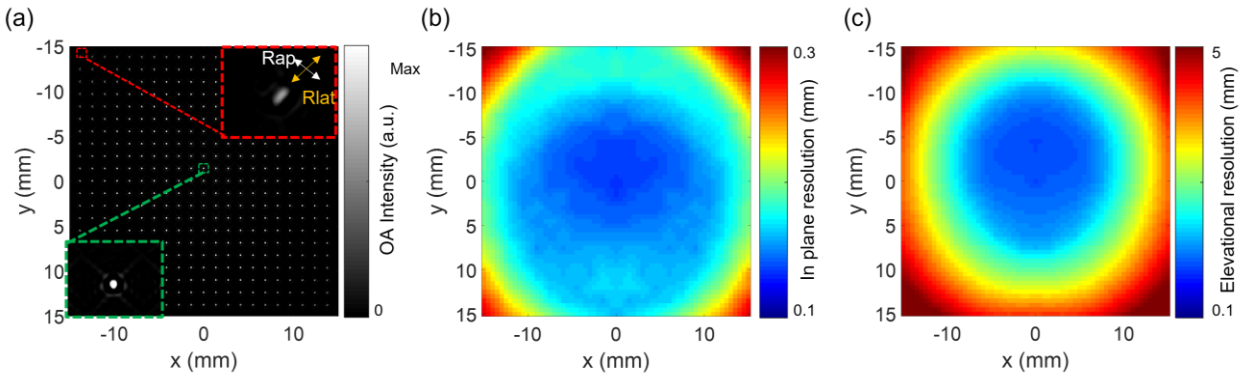

Figure 2.8. Spatial resolution. (a) Axial and lateral resolution of microspheres located in different positions of the 30 x 30 mm field of view. OA system resolution in the (b) image plane (c) elevational plane for a cylindrically focused transducer with element size of 0.735 mm x 15 mm, 40 mm element curvature and 37 mm elevational radius.

2.2.2.5 Image penetration depth

In pure optical imaging techniques, the maximum penetration depth (~ 1 mm in biological tissue) is strongly limited by the photon scattering process in the tissue, which also contributes to image blurriness and resolution loss. In OA imaging, a greater image penetration depth at high resolution can be achieved due to the detection of acoustic waves, in which acoustic scattering is much weaker compared to light scattering in biological tissue.

Nevertheless, the maximum achievable penetration depth in OA imaging is still primarily limited by light propagation inside the tissue, which depends on both absorption and scattering coefficients of the tissue and is wavelength dependent. According to the light diffusion theory [53], the laser

fluence distribution inside a homogeneous medium far from the boundaries decays exponentially and can be expressed as:

$$\Phi(r) = k\Phi_0 e\exp(-\mu_{eff} r) \tag{2.23}$$

where *k* depends on optical properties of irradiated tissue, Φ_0 is the fluence incident to the surface, and μ_{eff} is the effective optical attenuation coefficient $\mu_{eff} = \sqrt{3\mu_a(\mu_a + \mu_s')}$. Eq. 2.23 is valid under the conditions that 1) the scattering coefficient is higher that the absorption coefficient and 2) the object is located at a certain distance greater than $1/(\mu_a + \mu_s')$, which is called transport mean free path (MFP) from the beam. In the visible and NIR region, the former condition is satisfied for all tissues, while the latter is satisfied for a distance more than 1-2 mm.

The optical penetration depth in tissue is defined as the penetration at which the light fluence has decreased by 1/e and is given by:

$$\delta = \frac{1}{\mu_{eff}} = \sqrt{\frac{MFP'}{3\mu_a}} \tag{2.24}$$

For a general soft tissue with an absorption coefficient between 0.1-0.5 cm^{-1} and a reduced scattering coefficient between 10-20 cm^{-1} in the NIR region [54, 55], the optical penetration depth is about 5 mm, and at 1 cm depth the signal is already dropped by 87%. Therefore, OA signals from deeper tissue is weaker compared to signals from the surface, thus requiring an appropriate strategy to capture and process this large signal dynamic range.

For signals at tens of MHz, frequency-dependent acoustic attenuation also limits the imaging penetration depth. By comparing the acoustic attenuation equation (Eq. 2.10 in Sec. 2.1.3) and the fluence equation (Eq. 2.23), the frequency f_c at which the effect of acoustic attenuation equals the optical attenuation is given by:

$$f_c = \frac{\mu_{eff}}{\alpha_o} \tag{2.25}$$

Therefore, for detected frequencies higher that f_c, acoustic and optical attenuation equally contribute to limit image penetration depth. For example, considering a standard value of μ_a=0.2 cm^{-1}, μ_s=10 $cm^{-1}$and $\alpha_0 = 0.5\ dBMHz^{-1}$, the frequency f_c is calculated to be 43 MHz. Hence, at macroscopic scales where frequencies below 20MHz are acquired (i.e., OA tomography), the

effect of acoustic attenuation can be neglected, and the image penetration depth is mainly dependent on the diffuse light propagation in tissue. Fig. 2.9 shows the OA signal drops with depth due to acoustic attenuation (at 4 MHz) versus optical attenuation (at 800 nm) in breast bulky tissue, demonstrating that the optical properties of imaged tissue play a crucial role in image penetration depth in OA tomography. However, despite these results, it has been demonstrated that optoacoustic imaging can reach several centimeters' penetration depth by optimizing the wavelength and the light delivery configuration as well as maximizing the transducer sensitivity in the image field of view.

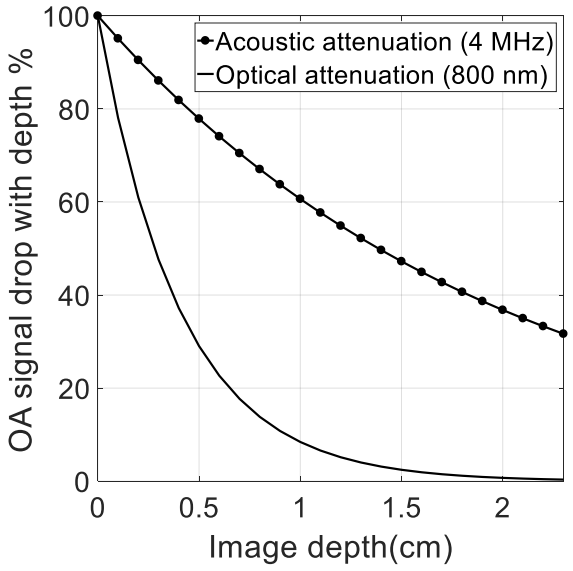

Figure 2.9. OA signal drops with depth in breast bulky tissue: acoustic vs. optical attenuation.

2.2.3 Tomographic image formation and quantification

2.2.3.1 Image reconstruction

The aim of tomographic image reconstruction in OA imaging is to provide a visualization of the absorber distribution inside the tissue, given a set of OA signals measured at certain transducer positions. Several algorithms have been reported for OA image reconstruction to solve the underlying acoustic inverse problem between pressure and absorption [22]. These methods can be classified in analytical and algebraic algorithms.

Among the analytical algorithms, back-projection algorithms are commonly employed due to their computational efficiency and simplicity [56, 57]. Although these algorithms are very fast and enable OA imaging in real-time, due to the approximation considerations in the solution, they can lead to image artifacts and quantification inaccuracy for functional and molecular imaging applications.

On the other hand, algebraic algorithms such as model-based approaches [58, 59] reconstruct an image using optimization algorithms in which the error between the measured signal and the signal theoretically predicted by the forward model is minimized. One of the advantages of these methods is that by incorporating the detection and tissue properties (i.e., transducer properties [60-62], acoustic inhomogeneity [63], or fluence [64]) into the model, optoacoustic images are reconstructed with high accuracy at the expense of the higher computational complexity.

Back-projection algorithm

Back-projection algorithms project each detected ultrasound signal from the detector to the image field of view based on the time-of-flight of the acquired signal. The back-projection is repeated for each detected signal, and the summation of the reversed signals in the image field of view provides the initial pressure distribution p_0 inside the tissue.

The analytic solution to retrieve the initial pressure distribution p_0 from the OA wave equation (Eq. 2.4) is given by the universal back-projection formula in [56]. For spherical detection surface, this can be written as:

$$p_0(\boldsymbol{r}) = \int_{\Omega_0} \frac{d\Omega_0}{\Omega_0} \left[2p(\boldsymbol{r_0}, \bar{t}) - 2\bar{t} \frac{\partial p(\boldsymbol{r_0}, \bar{t})}{\partial \bar{t}} \right]_{\bar{t}=|\boldsymbol{r}-\boldsymbol{r_0}|} \tag{2.26}$$

where $d\Omega_0$ is a solid angle for a detection element with dS_0 representing the infinitesimal detector surface and n_s^0 its perpendicular unit vector with respect to a reconstruction point **r:**

$$d\Omega_0 = \frac{dS_0}{|r-r_0|^2} \left[\frac{n_s^0 (r-r_0)}{|r-r_0|} \right] \tag{2.27}$$

The term $\frac{d\Omega_0}{\Omega_0}$ is a weighting factor that partially account for the directivity of the detector. Notably, the derivative term in Eq. 2.26 represents a ramp filter in the frequency domain, which considerably amplifies the high frequency components suppressing the low frequency signal.

Model based algorithm

In model-based approaches, the acoustic inverse problem is expressed as a linear system of equations with the initial pressure values as unknowns given the measured signal.

The discretization of Eq. 2.4 leads to a matrix equation of the form of [58]:

$$p = Mx, \tag{2.28}$$

where p is the broadband pressure signal recorded; x is the unknown distribution of optical absorption; and M is the linear operator that maps the unknown initial pressure to the recorded signal. The inversion of Eq. 2.28 is achieved by minimizing the squared error:

$$x^* = \arg\min_x \|p - Mx\|_2^2 . \tag{2.29}$$

A common problem when using standard model-based inversion is the appearance of negative values due to the bipolarity of the OA signal, which have no physical meaning since optical absorption can only be positive or zero. Furthermore, the OA inversion problem may be ill-posed, leading to the appearance of additional spurious negative values introduced during the inversion process as part of the minimization. For these reasons, non-negative constraints are included in the algorithm to guarantee physical integrity of the solution [65], i.e., positive optical absorption:

$$x^* = \arg\min_{x \geq 0} \|p - Mx\|_2^2 . \tag{2.30}$$

In contrast to unconstrained inversion, Eq. 2.30 cannot be solved analytically, and only iterative methods are applicable. Furthermore, since the problem in Eq. 2.30 is ill-posed and leads to inversion uncertainty, it requires additional regularization to impose additional constraints.

Thereby, Eq. 2.30 is modified by adding a Tikhonov regularization term, i.e.:

$$x^* = \arg\min_{x \geq 0} \|p - Mx\|_2^2 + \lambda \|Lx\|_2^2, \tag{2.31}$$

where λ is the regularize parameter, $\|\cdot\|_2$ is the L^2-norm. The matrix L can be selected as the identity matrix, which gives preference to solutions with a small norm, and penalizes any content

in the data that is not in agreement with the model, such as noise. Regularization is required to achieve a stable and unique solution.

The regularized problem in Eq. 2.31 can be formulated to the same form as Eq. 2.29:

$$x^* = \arg\min_{x \geq 0} f(x) = \arg\min_{x \geq 0} \left\| \tilde{p} - \widetilde{M} x \right\|_2^2, \tag{2.32}$$

with

$$\tilde{p} = \begin{pmatrix} p \\ 0 \end{pmatrix} \tag{2.33}$$

and

$$\widetilde{M} = \begin{pmatrix} M \\ \lambda L \end{pmatrix} \tag{2.34}$$

In this work, the Projected Conjugate Gradient [65] is used as non-negative least square (NNLS) methods to solve Eq. 2.32.

Model-based methods usually require large numbers of repeated sparse matrix-vectors multiplications in an iterative manner, causing significant computational cost. Nevertheless, recent advancements in powerful computational hardware and software have increased the availability of such complex reconstruction algorithms for real-time imaging.

2.2.3.2 Image quantification

Of particular importance in MSOT imaging is spatially resolving different intrinsic or extrinsic chromophores in tissue based on their spectral signature. The identification of different chromophores inside the tissue from images acquired at different wavelengths is achieved by solving the optical inverse problem through spectral unmixing algorithms.

The aim of spectral unmixing algorithm is to find the concentration $C_k(\boldsymbol{x})$ of k chromophores with known molecular absorption coefficient spectra $\alpha_k(\lambda)$, given the absorbed energy images $H(\boldsymbol{x}, \lambda)$ at different wavelengths λ:

$$H(\boldsymbol{x}, \lambda) = \mu_a(\boldsymbol{x}, \lambda) \Phi(\boldsymbol{x}, \lambda;\ \mu_a, \mu_s) \tag{2.35}$$

with Φ the light fluence in the absorbing medium. The absorbing coefficient $\mu_a(\boldsymbol{x},\lambda)$ can be written as the sum of their k chromophores with their respective molar absorption coefficient $\alpha_k(\lambda)$ and concentration $C_k(\boldsymbol{x})$:

$$\mu_a(\boldsymbol{x},\lambda) = \sum_{k=1}^{K} C_k(\boldsymbol{x})\alpha_k(\lambda) \tag{2.36}$$

Hence, combining Eq. 2.35 with Eq. 2.36 yields:

$$H(\boldsymbol{x},\lambda) = \Phi(\boldsymbol{x},\lambda;\ C_k,\mu_s)\sum_{k=1}^{K} C_k(\boldsymbol{x})\alpha_k(\lambda) \tag{2.37}$$

The unique spectral signature of each chromophore, i.e., the molar absorption coefficient α_k at different wavelengths, is generally well known. However, one challenge in the optical inverse problem is represented by the wavelength-dependent optical fluence attenuation with depth $\Phi(\boldsymbol{x},\lambda)$ which distorts the optoacoustic spectrum of absorbing chromophores compared to the nominal spectrum in a phenomenon well known as 'spectral coloring'. An additional challenge for retrieving $C_k(\boldsymbol{x})$ from Eq. 2.37 is that the unknown fluence Φ nontrivially depends on the chromophore concentration $C_k(\boldsymbol{x})$, and the relation between $H(\boldsymbol{x},\lambda)$ and $\mu_a(\boldsymbol{x},\lambda)$ is highly non-linear. To tackle this problem and retrieve the initial concentration map of a specific chromophore, different methods have been developed [23, 66], but a detailed overview is outside of the scope of this thesis.

In this work, the method of choice to retrieve the spatial distribution of the chromophores from the multispectral data is the linear spectral unmixing algorithm, which assumes that the nonlinear behavior in Eq. 2.37 can be consider linear if the changes are small. Under this simplification, the fluence can be considered constant and Eq. 2.37 can be written as [67, 68]:

$$H(\boldsymbol{x},\lambda) \propto \sum_{k=1}^{K} C_k(\boldsymbol{x})\alpha_k(\lambda) \tag{2.38}$$

And it is possible to setup a system of linear equations which takes the form of:

$$P = CS \tag{2.39}$$

Where P is the measurement matrix with dimension $m \times n$, where m are the number of single wavelength images and n the number of pixels in the image. S is a $m \times k$ matrix in which the columns contain the spectral signature of the k distinct chromophores. C is the unknown matrix

containing the concentration of each distinct absorber in the mixed pixel, which can be trivially retrieved from:

$$C = S^{+}p \tag{2.40}$$

Where S^{+} is the Moore-Penrose pseudo-inverse of the spectral matrix S.

2.2.4 Commercial pre-clinical and clinical OA systems

2.2.4.1 Preclinical MSOT inVision 256-TF

MSOT inVision 256-TF (iThera Medical, Munich, Germany, Fig. 2.10a) is a commercially available optoacoustic imaging system developed for pre-clinical applications, i.e., small animal imaging. This system acquires cross-section images with high resolution and penetration depth, *in vivo* and in real-time. The design of the light illumination and acoustic signal detection is optimized to reach an image penetration depth up to 2-3 cm.

The key aspects of the system and its functionality are shown in Fig. 2.10. The system features 360° ring illumination enabling a homogeneous illumination of the tissue, and a 270° acoustic detection to allow a faster placement of the sample (Fig. 2.10b). A tunable OPO laser provides high energy (100 mJ) excitation pulses with a duration of 5-10 ns in the wavelength range of 680-980 nm at 10 Hz repetition rate (InnoLas Laser, Germany). For tissue illumination, 10 arms of a fiber bundle are attached to both sides of the transducer and arranged at an angle of 13° to the image plane.

For acoustic detection, 256 cylindrically focused transducers with a central frequency of 5MHz and 100% bandwidth (-6 dB) in receive mode are used and organized in a concave array of 270° angular coverage and 40 mm radius of curvature (Imasonic, France). A 256-channel analog-to-digital converter is used to digitize the transducer signals at a sampling rate of 40 MS/s with an amplitude resolution of 12-bits.

The system provides an axial resolution of 120 µm, an elevational resolution of 1 mm in the focus, and an image field of view of 22 mm (FWHM of transducer sensitivity).

For pre-clinical imaging, the small animal is positioned in the animal holder, which provides anesthesia supply and is wrapped in a thin layer of polyethilene membrane to avoid direct contact between the mouse and the coupling medium, i.e., water or heavy water (Fig. 2.10c). Following the preparation and the positioning of the animal, the animal holder is inserted into the imaging chamber filled with water for acoustic coupling. The mouse holder can be translated by means of

a linear mechanical stage to enable imaging of multiple transverse slices for 3D whole-body imaging (Fig. 2.10d). The software viewMSOT enables fully automated image acquisition.

The system has already shown great potentials in preclinical applications such as breast cancer [69], neuro imaging [2, 70, 71], cardiovascular diseases [72, 73], metabolic diseases [74] and inflammation [75-77].

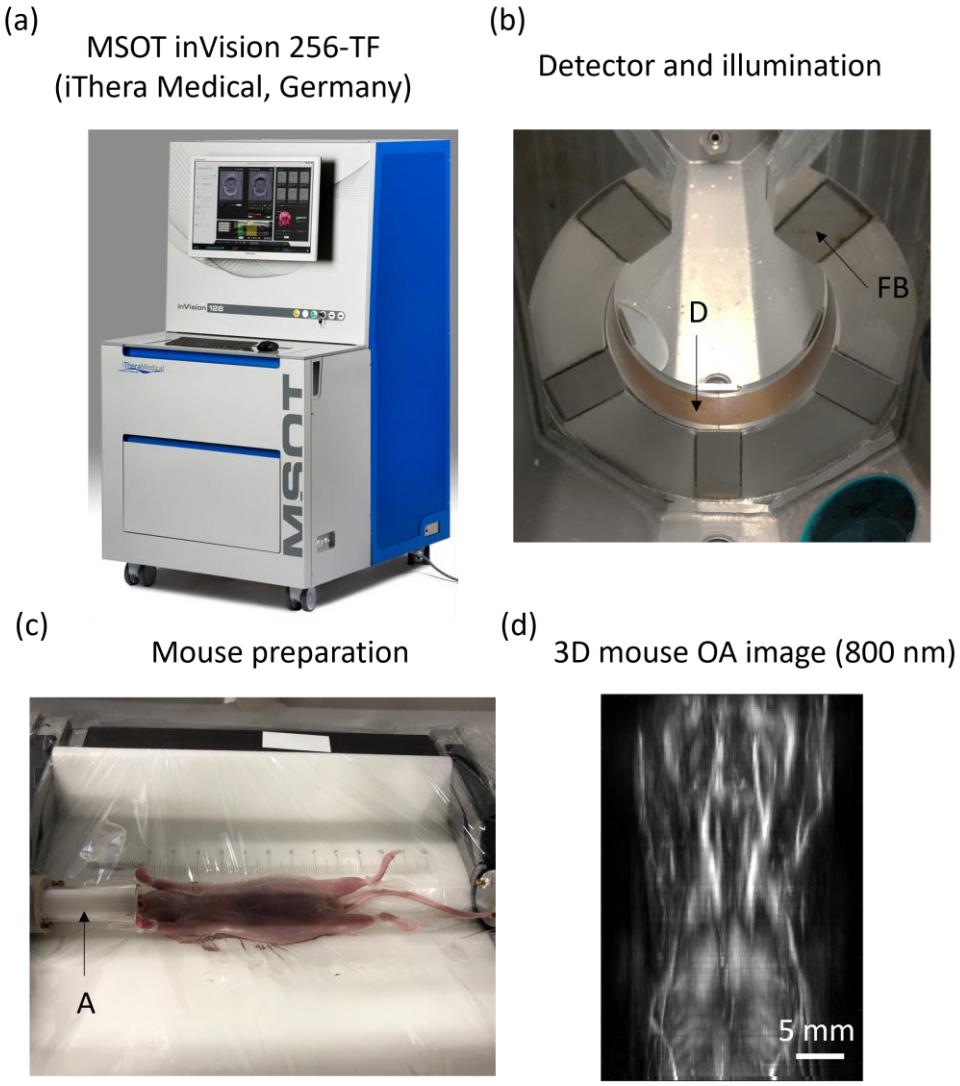

Figure 2.10. Preclinical OA system MSOT. (a) Commercially available MSOT inVision 256-TF (iThera Medical, Munich, Germany) for small animal imaging. (b) Detector (D) and illumination geometry with fiber bundle (FB). (c) mouse preparation and anesthesia supply (A). (d) 3D *in vivo* OA image of mouse at 800 nm.

2.2.4.2 Clinical MSOT Acuity Echo

The MSOT Acuity Echo (iThera Medical, Germany) is a commercially available hybrid ultrasound-optoacoustic (US-OA) imaging system for clinical applications. The key features of the system are reported in Fig. 2.11. The system has shown promising results in clinical trials involving Crohn's disease [17, 18], melanoma [78], breast cancer [79, 80], muscular diseases [16], vascular diseases [14, 81], metabolic diseases, and endocrinology [19, 82].

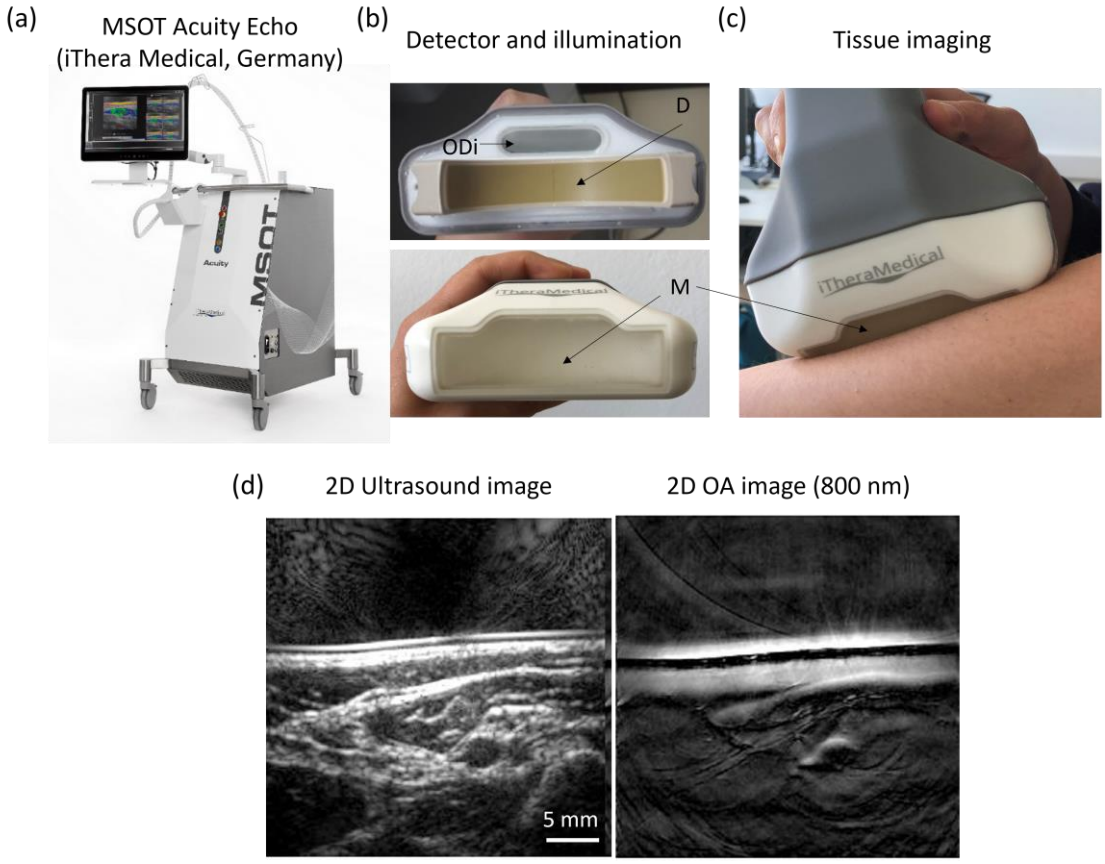

Figure 2.11. Clinical hybrid ultrasound-MSOT system. (a) Commercially available clinical MSOT system Acuity Echo (iThera Medical, Munich, Germany). (b) Handheld probe with the optical diffuser (ODi) for tissue illumination, curved array (D) for ultrasound detection and membrane (M) for tissue coupling. (c) Operation of the handheld probe for clinical imaging of the upper arm and (d) corresponding ultrasound and OA (800 nm) reconstructed images.

The OA imaging system is based on a 25 Hz pulsed OPO laser, which provides a maximum of 30 mJ peak pulse energy and a range of wavelengths between 660-1300nm (InnoLas Laser, Germany). For tissue illumination, a rectangular optical fiber output (Fig. 2.11b) attached to one

side of the transducer (short axis) interfaces with an optical diffuser. The light is therefore delivered obliquely (24° inclination) and relies on the light scattering inside the tissue to illuminate the whole field of view.

For acoustic detection, a concave array transducer (Imasonic, France) with 256 elements along an arc spanning 125° is used (Fig. 2.11b). The radius of the transducer array is 40 mm, and each element is cylindrically focused on the image plane with a radius of curvature of 40 mm. The central frequency of the transducers is 4MHz and with a bandwidth (-6 dB) of 100% in receive mode (optoacoustic mode) and 50% in transmit-receive mode (ultrasound mode). Due to the curved acquisition geometry, an acoustic coupling medium that is acoustically and optically transparent is positioned in from of the array to propagate the generated OA signal from the tissue to the ultrasound sensing element. The system is then confined in an optically and acoustically transparent membrane (Fig. 2.11b, c) to avoid leakage of the coupling medium onto the tissue. The system provides an axial resolution of 140 µm, an elevational resolution of 1.1 mm in the focus, and a good sensitivity up to 3 cm depth in OA mode. The system provides co-registered US-OA images of different anatomical sections (Fig. 2.11d).

3 Image quality degradation in OA tomography

In this chapter, different sources of image quality degradation in OA tomography are presented and discussed. A review of common approaches for image quality improvement in OA tomography is reported.

3.1 OA signal dependency

3.1.1 Scale-dependent SNR

Due to the broadband characteristic of the signal, OA images are inherently multiscale, which enables showing structures from millimeter to hundreds micrometer resolution simultaneously in the same field of view. However, there is one major challenge to broadband acoustic signal detection and processing in optoacoustics that contributes to degradation of image quality and quantification: the scale-dependent SNR.

As discussed in Sec. 2.2.1.1, the amplitude of the emitted OA signals scales with the size of the absorbing object, i.e., small-scale features have lower SNR compared to large-scale features. This has two direct consequences in OA images: first, the contrast of small structures is obscured by

the high signal from bulky absorbing object; second, the quantification of finer-scale absorbers can be compromised by the negative values from coarser ones.

Fig. 3.1 reports an example of image quality degradation in *in vivo* OA image from a mouse kidney section due to scale-dependent SNR. The reconstructed image in Fig. 3.1a (OA image) contains the full broadband OA information content and can be decomposed as the sum of images at different physical scales, e.g., an image containing OA signals from bulky tissues and organs (Large scale in Fig. 3.1a) and an image containing OA signals from microvasculature and small anatomical details (Small scale in Fig. 3.1a). Moreover, each scale contributes to the broadband OA signal with different frequency content, as shown in Fig. 3.1b, c. Notably, the dynamic range of the images is limited by the specific SNR of the size of the imaged objects and is lower for a small-scale image due to the weak OA signal. Consequently, when the full information content is rendered together (Multiscale), the contrast and visual perception of small structures is compromised by the dominant signal amplitude from large objects.

Nevertheless, the high OA signal from large absorbers can also compromise image quantification. As shown in Fig. 3.1c, d, the negative values of the OA signal from large-scale structures can superimpose with the weak OA signals from small-scale features when they are in proximity of coarser ones (red arrows), thus leading to inaccurate image quantification when spectral unmixing algorithms are applied.

In conclusion, the scale-dependent SNR – which is an intrinsic property of the OA signal – degrades OA images and results in image blurriness, with visual perception and quantification biased towards the larger structures. This is highly undesirable in medical imaging, where the entire frequency content is important, as it carries information about structures on different scales. Separate, distinct frequency components have been considered in Ultra-broadband Raster-Scan Optoacoustic Mesoscopy (RSOM) [45] and in OA microscopy [83]. However, simple separation of the frequency bands using signal processing filters neglects the broadband nature of the OA signal as well as the frequency content entanglement and may result in artifacts (i.e., ring artifacts). A correction for the scale-dependent SNR in OA imaging is proposed and discussed in Sec. 4.3.

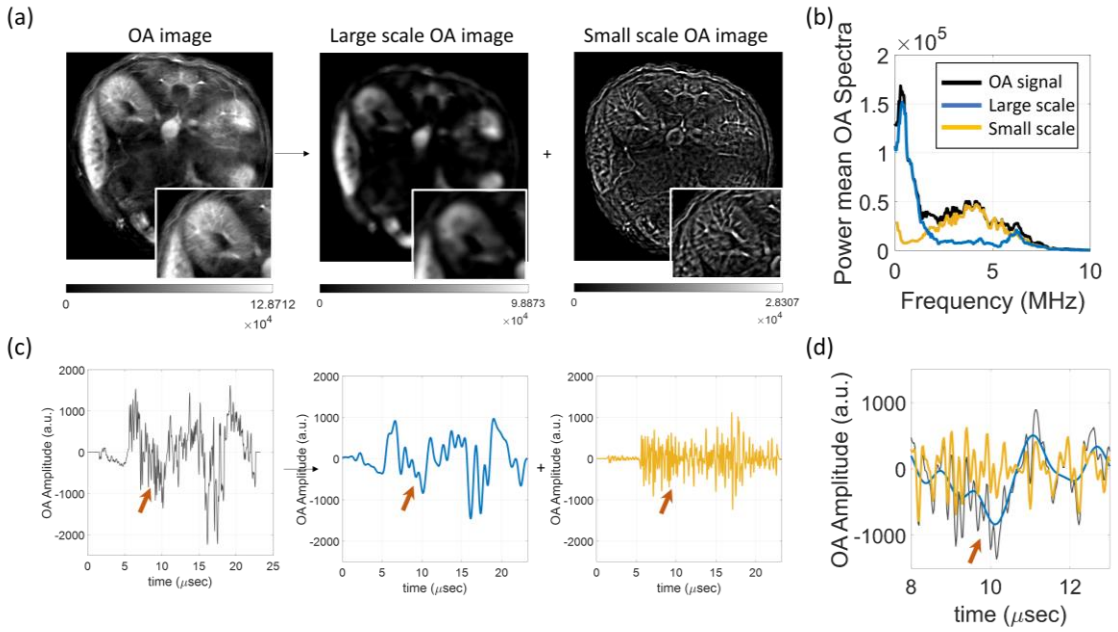

Figure 3.1. Image quality degradation in *in vivo* OA images of mouse kidney section due to scale-dependent SNR. (a) Reconstructed OA images of an *in vivo* mouse kidney section showing structures of different physical scales (i.e., sizes) with relative dynamic range. (b) OA signal in the frequency domain and (c) time domain for the images at different physical scales. (d) Example of negative values of the OA signal from large structures obscuring the weak OA signal from small features (Red arrows).

3.2 System dependency

3.2.1 Illumination geometry

OA imaging systems require high optical efficiency and the optimization of the tissue illumination (i.e., the light delivery system) is crucial to obtain high SNR at deeper penetration depth. New strategies have been developed to explore different illumination geometries with the goal of improving image quality and contrast by changing the beam directivity and shape [84, 85]. Fig. 3.2 shows standard illumination schemes employed in OA imaging, which can be divided into bright (Fig. 3.2a) and dark (Fig. 3.2b) field beam configurations. In the bright field configurations, the laser beam is coaxially aligned with the acoustic field so that the illuminated image plane corresponds to the plane where the transducer has its maximum sensitivity. Usually, bright field configurations are obtained by employing optically transparent transducers [86] or transducers with a central hole [87-91] or by using optical and acoustic reflectors to coaxially redirect the beam/acoustic waves [92, 93]. However, due to their complexity in the design, bright-field

illuminations cannot be easily integrated into standard preclinical and clinical OA systems that employ cylindrically focused transducers and require a dark-field illumination schema.

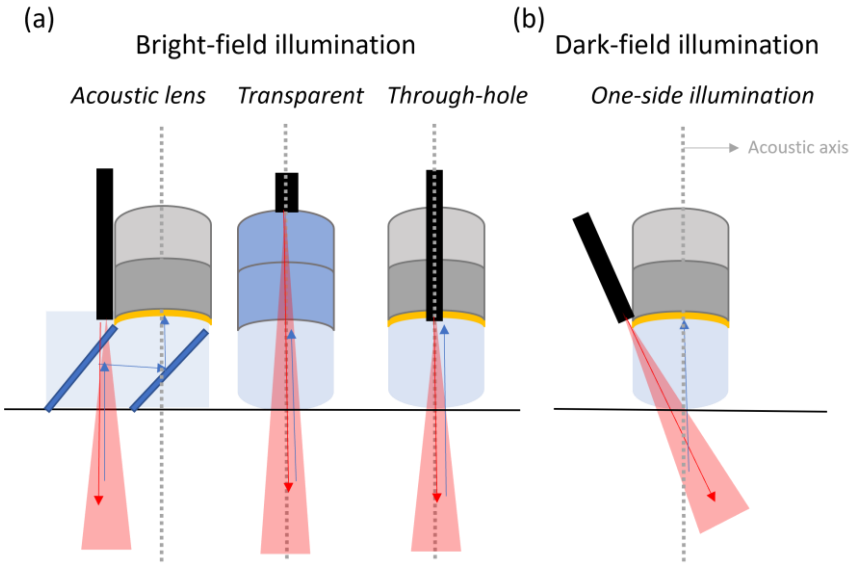

Figure 3.2. Schematics of standard illumination geometries used in OA systems. (a) Bright field illuminations. (b) Dark field illumination.

In the dark-field configuration, the illumination beam is attached to one or both sides of the transducer in the elevational plane (transducer short-axis), and the light is delivered obliquely to the image plane relying on the tissue scattering to illuminate the entire field of view.

To maximize the amount of fluence in deep tissue and minimize the illumination of out-of-plane tissue, the design of the beam angle, focus, and shape should be carefully considered [94]. To better understand this problem, the effect of different beam geometries on light distribution inside tissue at 800 nm is reported in Fig. 3.3. The light distribution was estimated by using Monte Carlo simulations (MCmatlab tool [95]). An OA synthetic phantom consisting of a transversal vessel embedded in bulky breast tissue was considered.

As shown in Fig. 3.3a, side-illumination geometries with higher beam angle (30° and 15°) lead to weaker fluence and low penetration depth inside the tissue compared to perpendicular illumination (0°). Furthermore, when the beam is focused on the intersection between the sample surface and the transducer short axis (CoS configuration in Fig. 3.3b) rather than deep in the tissue (1 and 2

cm depth configuration in Fig. 3.3b), this configuration enables a high fluence in the image plane and reduced out-of-plane illumination. Finally, reducing the beam width in the elevational direction (Fig. 3.3c) can increase the fluence in the image plane, although this approach can lead to a hot spot of light on the tissue surface and no benefit towards reducing out-of-plane illumination due to the high scattering properties of tissue.

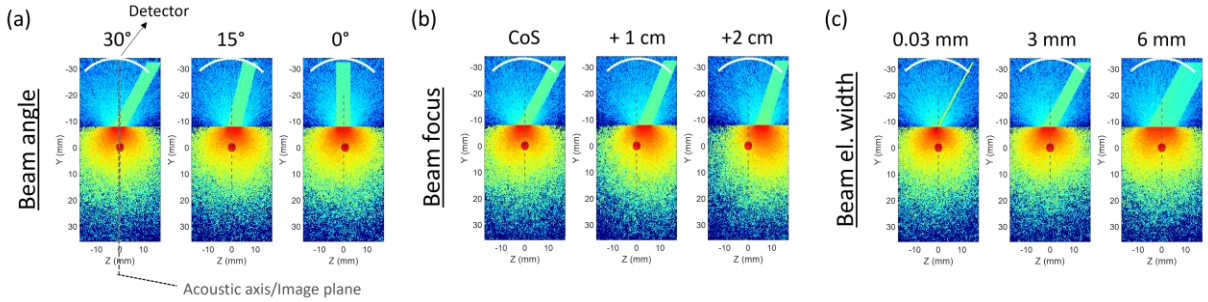

Figure 3.3. Effect of different beam geometries on light distribution in an OA phantom in the elevational plane. (a) Effect of different beam angles. (b) Effect of different beam focus parameters in the intersection between the sample surface and the transducer short axis (CoS), and at 1 and 2 cm depth of the sample (+1 cm and +2 cm configurations). (c) Effect of different beam widths in the elevational direction. The gray dashed lines indicate the acoustic axis or image plane, i.e., the plane where the transducer sensitivity is at its maximum.

As demonstrated, the beam geometry in OA systems has a clear influence on the fluence distribution inside the tissue and ultimately on the image SNR and penetration depth. Therefore, if the light beam is not optimized, this can degrade image quality, thus limiting the possible biological applications of OA systems.

3.2.2 Detector electrical impulse response

Advanced OA systems use broadband acoustic detectors to acquire the entire OA frequency content and ensure that no structural information is lost. This can be achieved by finely tuning the electrical impulse response (EIR) of the detector in receive mode, which is a combination between the electro-acoustic behavior of the transducer (backing material, piezocomposite, and matching layer) and the hardware of data acquisition (DAQ). Fig.3.4a demonstrates that by increasing the electrical impedance of the DAQ, the frequency response of the detector broadens despite the reduction in the central frequency.

(a)

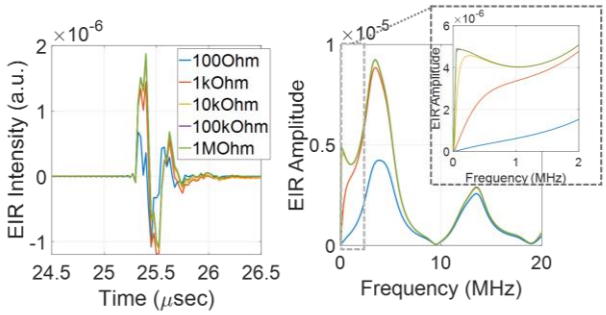

	100 Ohm	1 kOhm	10 kOhm	100 kOhm	1 MOhm
Fc (MHz)	3.89	3.5	3.48	3.48	3.48
BW (%)	84%	99%	101%	151%	151%

(b)

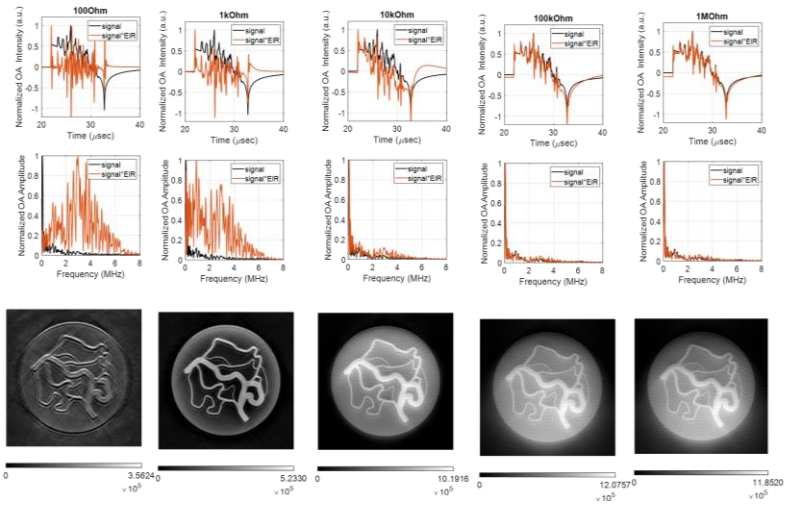

Figure 3.4. Effect of different detector EIR. (a) Transducer EIR with central frequency (Fc) and bandwidth (BW) for different DAQ electrical impedances. (b) Effect of EIR on OA signal detection and reconstructed images.

The dependency between detector EIRs and structural content in OA tomography is demonstrated in Fig.3.4b, where an OA synthetic phantom containing features of different physical sizes, i.e., small vessel-like structures embedded in a bulky absorbing object, was considered. Prior to reconstruction, the OA signals of the phantom were convolved for the different EIRs reported in Fig.3.4a to simulate the distortion introduced by the detector EIR on OA signal detection and image reconstruction. As shown in the figures, for low electrical impedance, the detector EIR behaves as a band pass filter, and low frequencies (which carry information of bulky objects) are not accurately detected. This leads to sharper reconstructed images, as signals from small

structures and edges are enhanced. In contrast, by increasing DAQ electrical impedance (higher than 100 kΩ), the detection bandwidth of the transducer is broadened. This allows the detector to also be sensitive to low frequencies, which are particularly important in biological applications where bulky absorbers are of primary interest. Therefore, to assure broadband signal detection and avoid information loss during acquisition, high electrical impedances in the DAQ are required.

Notably, even when the detectors are manufactured with sufficiently broadband response, the physical limitation in the bandwidth results in an inaccurate detection of the N-shape of the OA signal, which can lead to a loss of image resolution and the appearance of spurious negative values. Moreover, a non-flat frequency response of the transducer can compromise OA image quantification by nonuniformly weighting each frequency signal component.

Different deconvolution approaches have been proposed in OA tomography to retrieve the original OA signals from Eq. 2.13 and thereby improve OA image quality and resolution. Previous work has examined corrections for the EIR in animal systems with large-angle projections [96, 97], which showed resolution improvements in the reconstructed images.

In conclusion, this chapter illustrates the importance of having an adapted and sufficiently large detection bandwidth to accurately detect OA signals and avoid information loss. Sensitivity to low frequencies, which is achieved by increasing the input impedance, is necessary to visualize and quantify signals in large structures and organs as well as detecting slowly varying phenomena light attenuation inside the tissue. The ability to capture high frequencies is fundamental to achieving high resolution and therefore resolve small absorbers. Failing to detect the necessary frequencies leads to inaccurate reconstructions and an erroneous representation of part of the signal.

3.2.3 Finite size of the detector and spatial impulse response

The spatial impulse response of the detector represents a source of image quality degradation in OA imaging. If not corrected, this leads to significant reconstruction inaccuracy. The effect of the detector's spatial impulse response on OA reconstructed images of an *in vivo* mouse kidney section is reported in Fig. 3.5. Two different detection geometries were considered: a first configuration (a) with 270° angular coverage, 256 elements, and single element width of 0.736 mm (inVision 256-TF); a second configuration (b) with 270° angular coverage, 128 element, and double element width of 1.4 mm, which was simulated by averaging the signals from two adjacent detectors from configuration (a). The reconstructed images clearly show that larger detection elements lead to

inaccurate image reconstruction of small structures and image distortion, while smaller detectors enable imaging with better resolution and higher image fidelity. While smaller transducers could result in more accurate image reconstruction – albeit at reduced sensitivity – recently proposed methods have focused on including the spatial impulse response SIR (Section 2.2.2.3) of the detectors in the reconstruction algorithms to improve OA image quality.

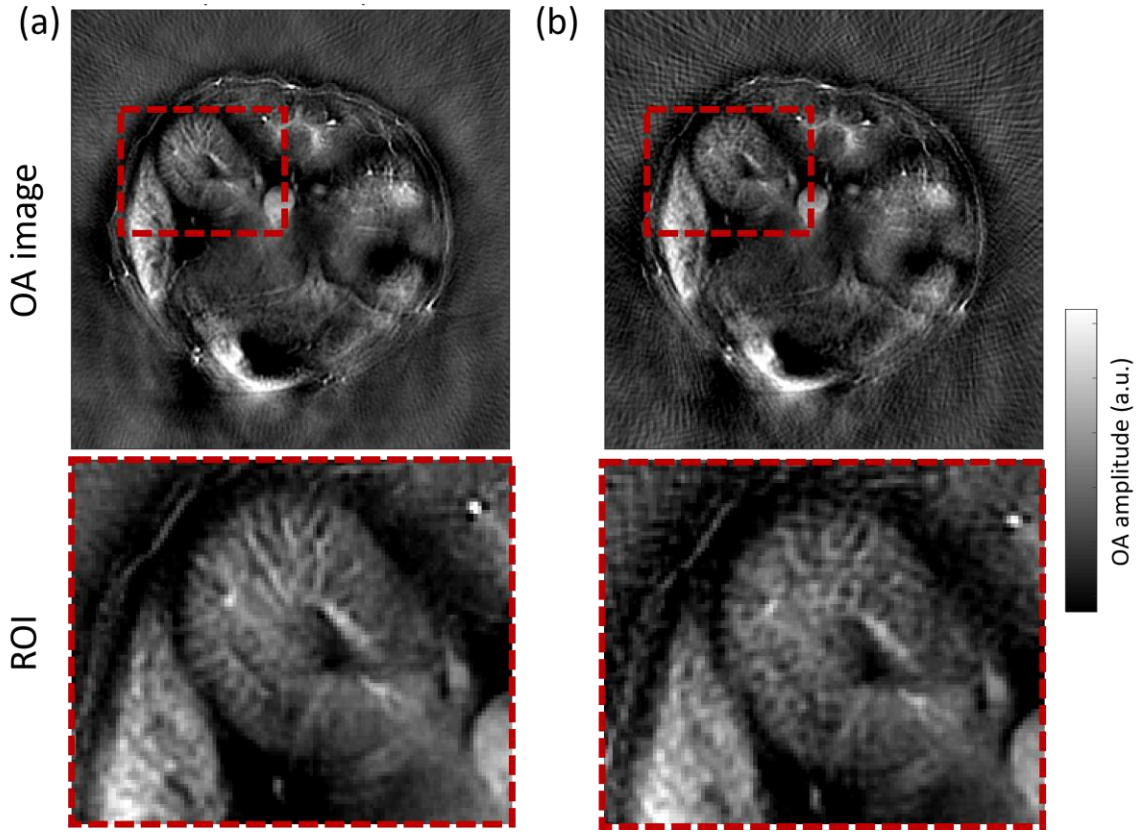

Figure 3.5. Effect of spatial impulse response and finite size of the detector. Reconstructed OA images of mouse kidney sections acquired using detectors with different element widths, (a) 0.736 mm and (b) 1.4 mm.

The effect of SIR correction has been firstly investigated on full-projection animal systems showing improved image quality and artifact reduction [47, 61, 98]. A further improvement in the image spatial resolution in small animal imaging systems was also demonstrated by proposing a complete TIR correction schema that includes both the detector EIR and SIR in the reconstruction algorithm. Finally, recent works have been focused on TIR correction under non-uniform speed of

sound and in limited view acquisition geometries, thereby demonstrating improved image quality and accuracy in OA clinical images [60, 62].

3.2.4 Frequency-dependent detector sensitivity and out-of-plane signal

An additional source of image quality degradation in optoacoustics is detected out-of-plane signals. As light propagates in highly scattering medium (such as biological tissue), it is diffused in all directions. A fraction of the photon energy is also absorbed from chromophores located at different image planes, generating the so called out-of-plane signals. Although cylindrically focused transducers are usually employed in OA tomography to reject out-of-plane signals, the detectors are still sensitive to an amount of out-of-plane signal at low frequencies due to the frequency dependent sensitivity field. Fig. 3.6a shows the sensitivity of a cylindrically focused transducer in two different frequency bands: a low frequency band between 0-1.3 MHz (Low f) and a high frequency band between 1.3-13 MHz (High f). As demonstrated, the transducer has both good sensitivity in the image plane and good focus in the elevation direction at high frequencies above 1.3 MHz (High f). In contrast, at low frequencies below 1 MHz (Low f), the resulting image is less focused in the elevational direction, and out-of-plane signals are detected.

When projected into the reconstructed image, the detected out-of-plane signals lead to image artifacts and distortion. Fig. 3.6b illustrates an example of structure distortion in a synthetic OA phantom containing three absorbing microspheres, one positioned in the image plane (yellow sphere) and the other two at 1.7 mm and 3.4 mm far from the image plane (blue spheres). As shown in the reconstructed images in Fig. 3.6b, the out-of-plane microspheres appear blurred and out of focus compared to the in-plane microsphere.

Fig. 3.6c reports the detected OA signals for the three microspheres in time and frequency. The signals from the microspheres out of the image plane are spread and distorted compared to the in-plane microsphere. Furthermore, their frequency contents contain only low frequency components due to the out-of-plane sensitivity of the transducer only at low frequencies.

Out-of-plane signals have been separated from in-plane signals by axially displacing the transducer array and by de-correlating images acquired at different out-of-plane positions with the in-plane image [99, 100]. However, such approaches are impractical, as they require the displacement of the transducer and do not consider the frequency-dependence of the detector’s sensitivity.

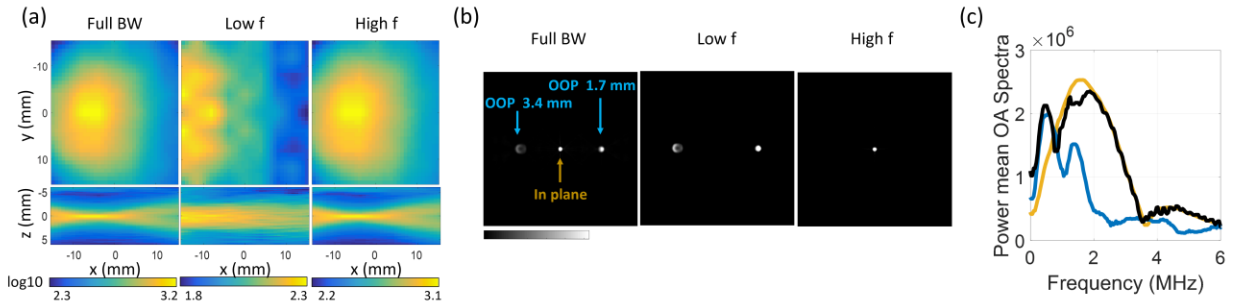

Figure 3.6. Frequency-dependent sensitivity field and effect of out-of-plane signals. (a) Frequency-dependent transducer sensitivity field in the image plane XY and in the elevational plane ZX. (b) OA image showing in-plane and 1.7 mm and 3.4 mm out-of-plane (OOP) microspheres. (c) OA spectrum of the in-plane microsphere in yellow and low-frequency-shifted spectrum in blue for the out-of-plane microspheres. Full bandwidth (Full BW); Low frequencies (Low f); High frequencies (High f).

3.2.5 Insufficient spatial sampling

In agreement with the Nyquist theorem, to accurately reconstruct an OA absorber in certain position of the field of view, the spatial sampling of the detector surface must be at least twice the maximum frequency of the generated OA signal from the absorber to obtain the maximum resolution achievable by the OA system and to avoid aliasing artifacts.

For circular acquisition geometry, the condition to be respected is $r_o \Delta\varphi_0 < \delta/2$, where r_o is the radius of the detection surface, $\Delta\varphi_0$ is the angular sampling period of the detector surface, and δ is the size of each single element (sub element) the detector has been sampled [101].

In standard array configurations used for real-time OA tomographic imaging, i.e., in inVision 256-TF with 270° angular coverage, 256 elements and 40 mm radius of detection surface, due to physical constraint, it is not possible to design the transducer with enough densely spaced elements. Consequently, aliasing artifacts are expected in the image, and the sparser the transducers the stronger the artifacts. Fig. 3.7a shows an example of stripe artifacts resulting from insufficient spatial sampling in *in vivo* OA images of a mouse kidney section acquired with inVision 256-TF.

An easy method to reduce aliasing artifacts due to sparse signal acquisition in OA tomographic images is to add virtual projection by interpolating measurements from two adjacent detectors, as

shown in Fig. 3.7b. Notably, the interpolation does not add any information content to the image and results in image blurriness.

More complex solutions have been proposed to reduce aliasing artifacts by using compressing sensing [102, 103] or deep learning methods [104, 105], demonstrating increased image quality in *in vivo* imaging.

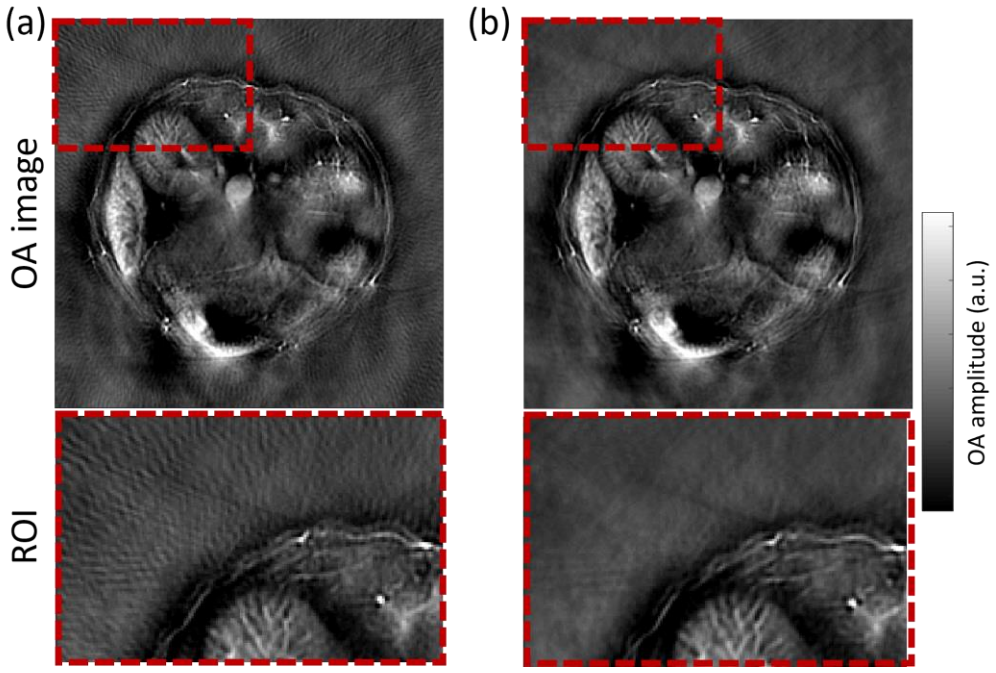

Figure 3.7. Effect of insufficient spatial sampling and aliasing artifact reduction. OA reconstructed image of *in vivo* mouse kidney section showing (a) enhanced stripe artifacts in the image background due to insufficient spatial sampling and (b) reduced stripe artifacts after data interpolation.

3.2.6 Limited view detection

To accurately reconstruct an object, OA signals should be collected from a detection surface that fully encloses the sample (Sec. 2.2.1.2). However, in practical applications, this cannot be achieved. In preclinical systems for small animals imaging, a reduced transducer angular coverage facilitates the positioning of the sample in the imaging chamber. In clinical systems, handheld detectors that partially enclose the tissue enable to image different body parts. In practice, due to limited view detection, structures with certain directivity may appear invisible or can be only

partially reconstructed. The condition under which an object is visible for a given detection geometry is that for each boundary point, the normal of the curve passing through that point intersects the detection curve [106]. If this condition is nor verified, the wavefront is not detected and therefore will appear blurred in the reconstruction.

Fig. 3.8a reports the effect of limited view detection in *in vivo* OA images from a mouse liver section reconstructed by considering different transducer angular coverage, 360°, 270° and 125°. Notably, anatomical structures in certain positions of the field of view are either not accurately reconstructed or appear invisible in OA detection. An example is represented by the vessels in the lower part of the liver section, which are accurately reconstructed with 360° angular detection (green arrows) but appear blurred and smeared with lower angular detection geometries of 270° and 125° (orange arrows). The 2D Fourier transform of the reconstructed images in Fig. 3.9b show the spatial information lost due to limited view detection. In particular, the 2D spectra of the reconstructed images is uniformly distributed across all directions with 360° detector angular coverage and lacks information at angles not covered by the detection surface with limited view acquisition (270° and 125°).

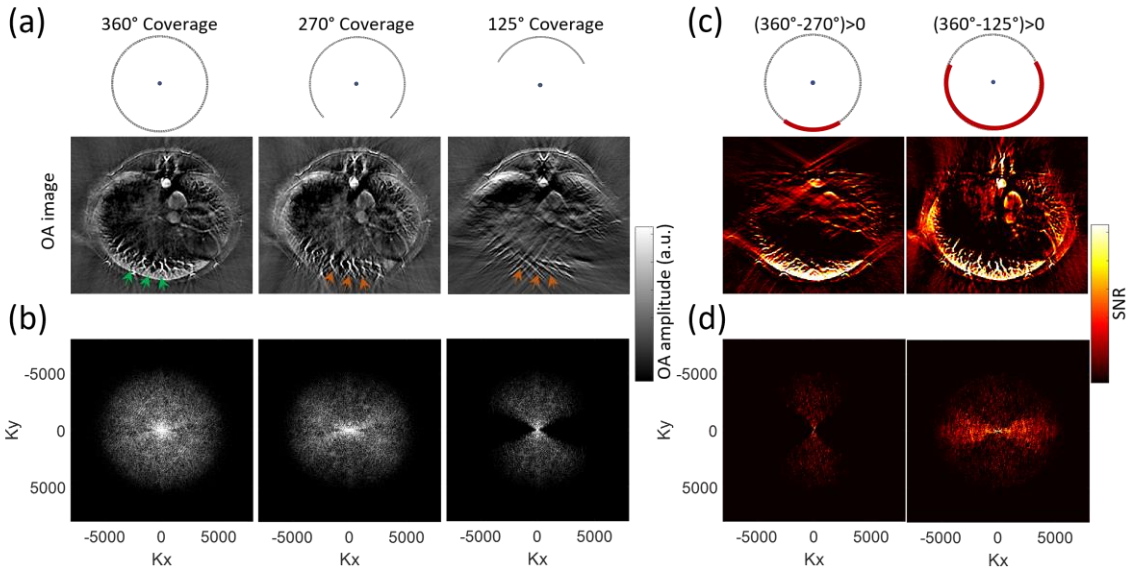

Figure 3.8. Effect of transducer angular coverage and limited view artifacts. (a) Reconstructed OA images and (b) 2D Fourier transform for different transducer angular coverage, 360°, 270° and 125°. (c) Reduction of image SNR for 270° and 125° transducer angular coverage, compared with 360° transducer detection geometry. (d) Spatial information lost due to limited view detection compared to full view detection.

Different methods have been proposed to account for the effect of limited view detection in OA imaging [107, 108]. These methods include iterative image reconstruction algorithms based on total variation (TV) regularization [109, 110], wavelet sparsity constraints [111], and deep learning approaches [112, 113] to improve image quality in limited-view acquisition geometry.

3.2.7 Electromagnetic interference

Image quality in OA can be severely degraded by electromagnetic interference (EMI) or parasitic noise between different hardware components. A common effect of EMI is the appearance of ring artifacts in the reconstructed OA images (Fig. 3.9a), a problem also reported for other medical imaging modalities [114].

However, in acquisitions where multiple frames are required, EMI results in OA signal intensity flickering between frames, which can lead to stripe artifacts or inaccurate image quantification. For example, when 2D images are acquired at consecutive positions and stacked together to create a 3D volume, the intensity flickering between frames results in stripe artifacts, as reported in Fig. 3.9b (800 nm). Furthermore, in multispectral acquisition where OA images are acquired at different wavelengths, the EMI can affect image quantification (Fig. 3.9b, Hb and HbO2 maps).

While shielding the different hardware components can suppress some electromagnetic noise, this solution is device-specific and strongly affected by the environment. Furthermore, due to the broadband nature of the noise, there is no method to efficiently filter the noise while preserving the entire broadband OA information content [115].

Frame averaging and different regularization techniques [116-118] have been considered for reducing electrical noise. While the former leads to resolution loss and reduced image frame rate, the latter may result in inaccurate image reconstruction. A recent denoising approach based on deep learning has shown great potential for noise removal in OA images by improving image contrast and spectral unmixing performance in real-time [115].

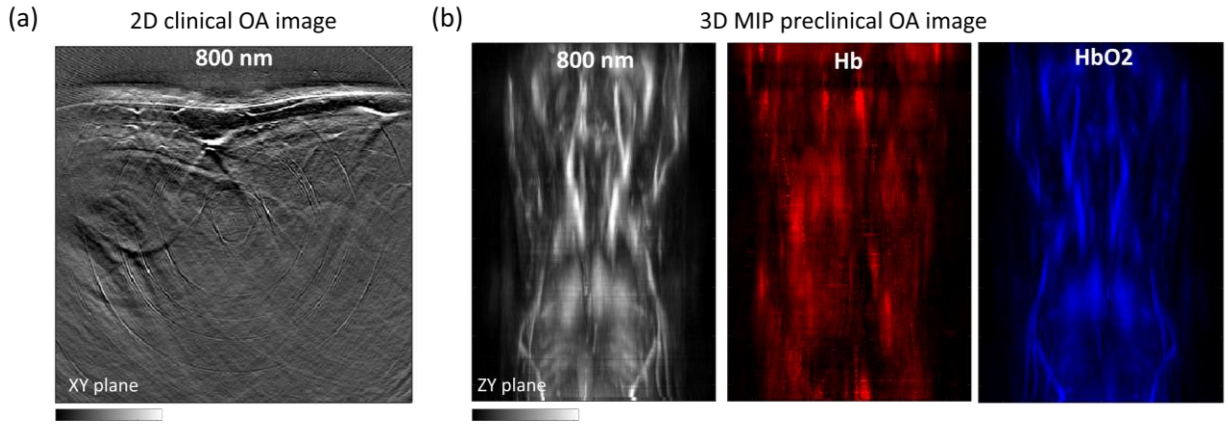

Figure 3.9. Artifacts in OA images due to electromagnetic noise. (a) Ring artifacts in 2D clinical image of the human neck region. (b) Stripe artifacts in 3D Maximum intensity projection (MIP) images of *in vivo* mouse section due to intensity flickering between adjacent frames, for single wavelength (800 nm) and multiwavelength (deoxygenated hemoglobin Hb and oxygenated hemoglobin HbO2 maps) acquisitions.

In conclusion, a denoising strategy that can achieve EM noise suppression with minimal signal loss is of great interest in OA imaging, as it will result in increased system sensitivity and thus enable detection of molecular agents with lower absorption or at low concentrations inside the tissue.

3.3 Signal and image processing dependency

3.3.1 Signal processing

Signal averaging is the most common signal pre-processing techniques to reduce noise and improve SNR in OA images. However, as already discussed in the previous section, signal averaging reduces the imaging frame rate and for moving samples results in increased image blurriness.

Signal deconvolution methods, such as inverse filtering, Wiener deconvolution, and Tikhonov L2-norm regularized matrix inversion methods, have been proposed to improve OA image resolution by deconvolving the signal for the illumination pulse and/or for the ultrasound transducer electrical impulse response.

Furthermore, signal filtering or Wavelet transform-based filtering methods are also employed in OA imaging to separate different structure components and reject noise [11, 45, 83]. Fig. 3.10

reports the effect of different high pass filter cutoff thresholds on OA image content from an *in vivo* mouse kidney section.

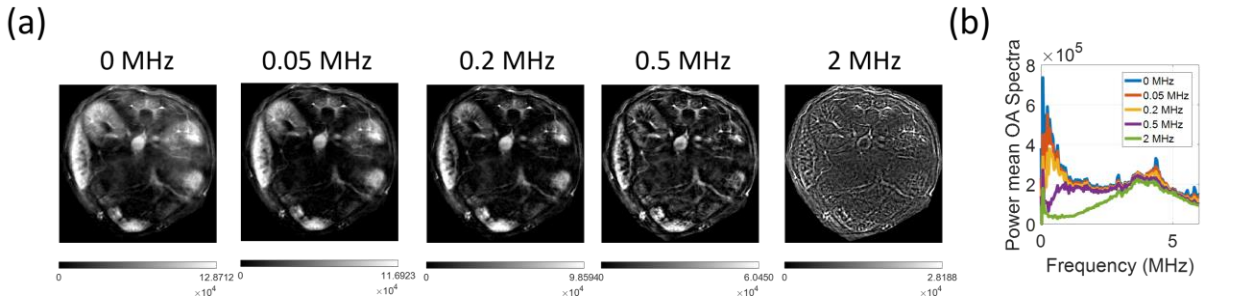

Figure 3.10. Effect of different high-pass filter cutoffs on OA image quality and structural content. (a)OA reconstructed images and (b) respective signal frequency content (Power mean OA spectra) of an in vivo mouse kidney section for different signal frequency cutoffs. "0 MHz" refers to the full bandwidth image where no filter is employed, and the entire OA information content is reconstructed.

As already discussed in Sec. 2.2.2.3, based on the biological application, specific bandpass filters can be applied to the broadband OA signals to reconstruct and enhance only the structures with a certain specific size while discarding other frequency bands that contain noise or unwanted features. For instance, a low frequency filter cutoff could be applied to visualize big organs and bulky tissue, while a high frequency filter cutoff above 2 MHz could enable detection of small anatomical details. Nevertheless, both methods result in a contradiction; they afford visually pleasing images by penalizing either low or high frequency content and ultimately reducing image fidelity. Furthermore, simple separation of the frequency bands using signal processing filters neglects the broadband characteristic of the OA signals and may result in image artifacts (e.g., ring artifacts).

3.3.2 Image reconstruction

Various aspects of OA image reconstruction problems have been investigated and addressed to improve image contrast and resolution, especially for sparse and limited view acquisitions. OA image quality improvement has been achieved by modeling the property of the detector [49, 60, 62] and the underlying OA physics [29], accounting for the acoustic properties of the tissue [119-123], including the light fluence [64, 124, 125], or introducing different regularization schema [123-131].

However, reconstruction techniques for OA tomography systems have yet to account for the broadband and multiscale characteristics of OA signals, which require proper strategy to reconstruct and visualize the rich info content. So far, most OA image reconstruction techniques do not address the broadband nature of OA signals, and standard reconstruction techniques employed in OA tomographic imaging have failed to accurately render the rich multiscale information content of OA data.

Fig. 3.11 reports OA images of *in vivo* mouse brain and kidney sections generated using standard tomographic reconstruction approaches. The universal back-projection algorithm (Universal BP in Fig. 3.11) enhances the high frequency components of the images, i.e., small vasculature and structure edges, and considerably suppresses the low frequency signals from bulky absorbing tissues and large organs. Although images acquired by filtering out the low frequency information appear to be of better quality (as they portray highly detailed features), they inevitably reject some OA information and reduce the fidelity of the object reconstructed, even if the images appear visually pleasing. Therefore, quantification inaccuracy on the reconstructed images is also expected in this scenario, as the different frequency components are weighted differently.

In common delay-and-sum beamforming (BP in Fig. 3.11) and standard model-based algorithm (MB in Fig. 3.11), the rich OA frequency content is directly projected onto a single image. However due to the scale-dependent SNR (Section 2.2.1.1), the reconstructed images appear blurred since the information content is biased towards the low frequencies, and the contrast of small structures is obscured by the high SNR of bulk tissue. Furthermore, the OA signal quantification in small vasculature is compromised due to the negative values from large-scale features hiding the weak OA signals from small absorbers.

In conclusion, enabling visualization of full broadband information content in a single image is still a challenge and an unsolved issue in OA imaging. A novel method that handles each frequency separately could result in better representation of all frequency content, thus increasing the contrast and SNR available for the high frequencies and reducing artifacts. Indeed, as demonstrated in this work, developing a strategy to render this broadband information results in an improved image visualization in OA imaging and ultimately improve the preclinical and clinical impact of OA technologies.

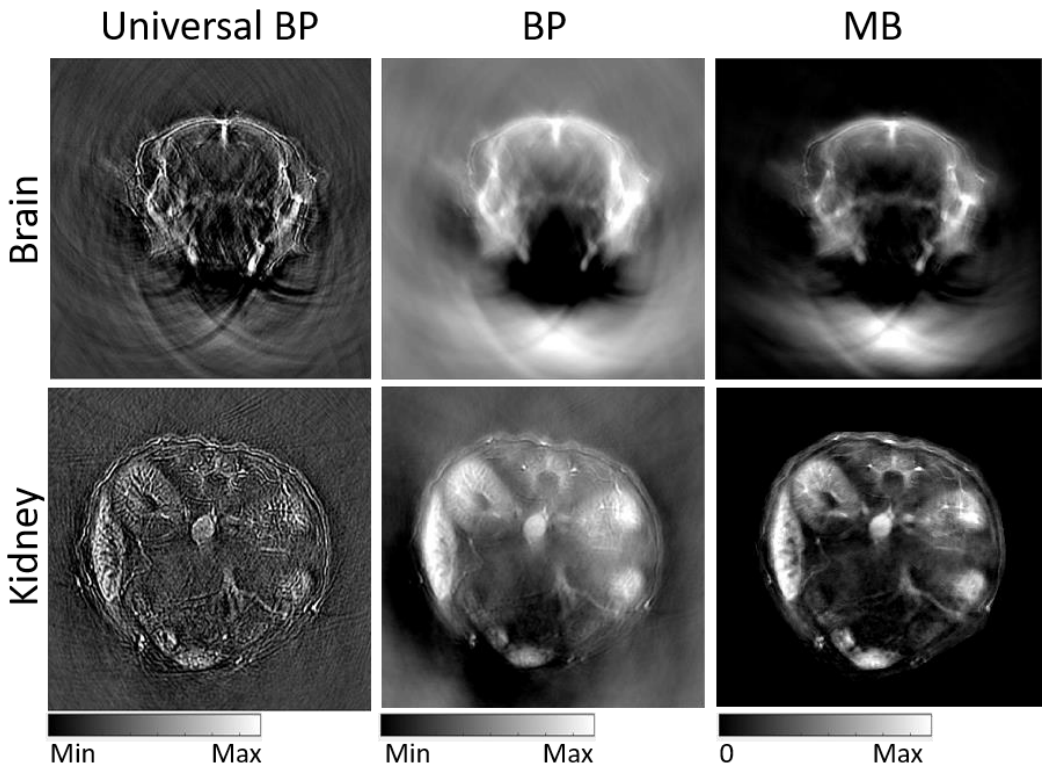

Figure 3.11. Effect of different reconstruction algorithms on OA image quality and structural content.

3.3.3 Image processing

OA images often suffer from low contrast and noise artifacts that strongly depend on the acquisition and reconstruction approach. The development of novel image contrast enhancement tools is essential in preclinical and clinical OA imaging, as they play a critical role in real-time visualization of structures to support accurate diagnosis and disease treatment.

However, artifacts and background signal present major limitations for the development of image post-processing methods in OA imaging. Artifacts appear as structures of interest in the image field of view and can be amplified by enhancement algorithms. Furthermore, enhancement techniques based on pixel intensity are not suitable for OA images because signal intensity varies with depth due to light and sound attenuation.

Several methods have been proposed for 2D and 3D enhancement of vasculature in OA imaging. Multiscale/multiorientation algorithms such as matching filters [132], Laplacian pyramid [133], wavelet transform [134], and Gabor filter [135, 136] are suitable for OA, but require prior selection

of anisotropic kernels and definition of a classification function for segmentation. Methods based on feature modelling, tracking, and artificial intelligence are mainly used for vessel segmentation rather than for contrast enhancement, as required in OA imaging. These approaches are also computationally complex and require *a priori* information to guide the segmentation process. Instead, the Hessian-based Frangi filter is conventionally used for OA image enhancement because it employs a well-defined kernel and vessel classification function, which simplifies its implementation [137].

However, enhancement algorithms may introduce artifacts and amplify noise; therefore, investigation of these tools in the context of accuracy is crucial. Furthermore, since contrast enhancement techniques are nonlinear operators, this cannot be employed for image quantification.

3.4 Tissue dependency

3.4.1 Fluence

The visual quality of OA images is frequently degraded due to uneven light deposition (fluence) inside the tissue; deeper structures are poorly illuminated compared to superficial tissue and exhibit depth-dependent, exponentially decaying SNR. Fig. 3.12a reports the OA signal amplitude drop with depth for different breast tissue types reported in literature.

Since the SNR exponentially decays with depth, superficial layers of the imaged tissue exhibit high signal intensity and appear oversaturated, while the contrast of deep structures and small anatomical details is impaired due to weak signal amplitude. Moreover, signal from lower-absorbing chromophores can be hidden by nearby higher-absorbing chromophores.

Fig. 3.12b shows an example of OA image quality degradation in *in vivo* mouse imaging due to fluence. Notably, in the liver section, the high optical absorption of the superficial layers of the liver prevent light from penetrating, thus reducing the contrast of deep structures. In contrast, a low fluence effect is observed in the lower abdomen section due to the less-absorbing superficial tissue, which results in a more homogeneous contrast over the full image.

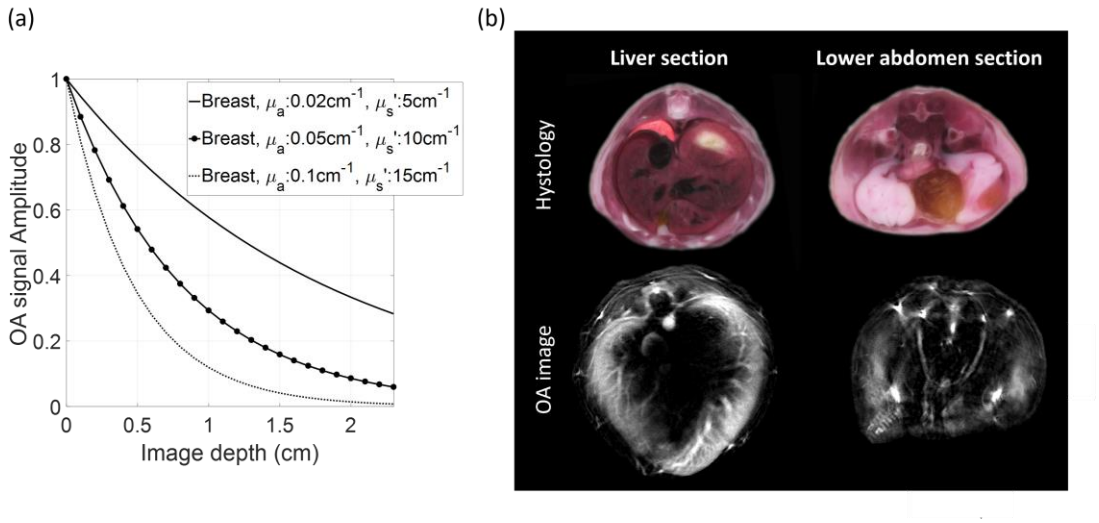

Figure 3.12. Effect of fluence in OA imaging. (a) Exponentially decaying OA signal amplitude with depth for different breast tissue types. (b) Histology images and corresponding OA images of different mouse anatomical sections: mouse liver with high tissue fluence; mouse lower abdomen with low tissue fluence.

Due to light fluence in tissue, OA images are usually characterized by a high dynamic range, i.e., wide intensity range. Depending on the anatomical section being imaged, further processing steps are necessary to improve the perceived image contrast and enhance the entirety of the OA information – from both the brightest and the darkest areas of the image.

More complex postprocessing steps have been proposed to improve the perceived image contrast in OA small animal imaging by applying contrast-limited adaptive histogram equalization [122] or by employing an adaptive gain compensation method [138]. However, the developments of new algorithms to better render OA images by narrowing the intensity range is highly demanded. This is a much more crucial problem for clinical handheld probes in which the tissue illumination is performed from one side only and the laser illumination decays rapidly with depth.

3.4.2 Acoustic propagation

The assumption of wave propagation in acoustically homogeneous medium is usually made in OA imaging for simplification. However, acoustic inhomogeneity inside the tissue can introduce distortion in the acoustic propagation, which results in artifacts in the reconstructed images if the corresponding effects are not corrected. Reconstruction procedures – including acoustic properties within the tissue – may help improve the OA image quality, for instance by retrieving information from the combined ultrasound modality.

Speed of sound variation and acoustic refraction

Conventional reconstruction methods assume a uniform speed of sound to calculate the signal time-of-flight necessary for the reconstruction. However, the precise speed of sound in the imaged medium is unknown, and an incorrect selection of speed of sound can lead to inaccurate image reconstruction. Fig. 3.13a reports OA images from different mouse anatomical sections reconstructed using various speed of sound values. As demonstrated by the variable image quality, the selection of an incorrect speed of sound value results in image distortion, i.e., horseshoe-shaped artifacts on the mouse surface [138] and image resolution loss, which can be mitigated by manual [138, 139] or automatic speed of sound tuning approaches [140].

Nevertheless, significant reconstruction inaccuracies may also arise from speed of sound mismatch between the imaged tissue and the coupling medium. Fig. 3.13b reports the distortion of the reconstructed OA image of a microsphere introduced by speed of sound inhomogeneity between the tissue and the coupling medium when acoustic refraction is neglected. As shown in the figures, fringing artifacts occur in the image, which distort the position and the size of the microsphere. It is important to note that this effect cannot be removed in post-processing.

In small animal imaging systems, it has been shown that the quality of OA reconstructions can be improved by accounting for the heterogeneous speed of sound between tissue and coupling medium (i.e., water) so that the image resolution can be maintained across different tissue depths. Furthermore, since the variation of speed of sound in soft tissues is rarely higher than 10% [32], the assumption of straight propagation of the acoustic rays is acceptable.

However, for clinical handheld systems, it has been demonstrated that refraction at the interface between coupling medium (usually heavy water) and tissue plays a major role in OA image quality, and the assumption of straight ray propagation in not valid anymore. To address this, a reconstruction algorithm that includes acoustic refraction (i.e., bent raytracing) between tissue and coupling medium has been developed. This algorithm shows improved axial and lateral resolution as well as reduced structure distortion in clinical OA images [62]. More sophisticated reconstruction procedures that consider a heterogeneous speed of sound distribution within the tissue may further help improve the OA image quality, for instance by retrieving information from the combined ultrasound images [122]. Although they drastically increase the complexity of image

reconstruction, these approaches are nowadays of great interest for improving OA image quality and accuracy.

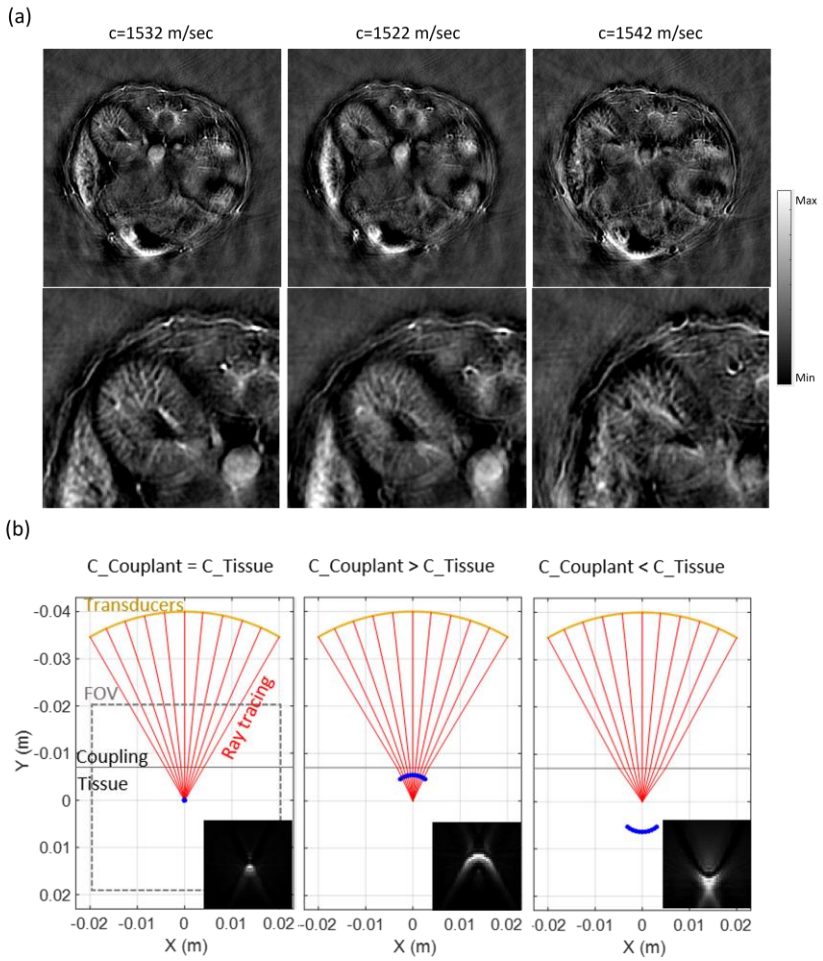

Figure 3.13. Effect of speed of sound selection and acoustic refraction in OA images. (a) Artifacts in *in vivo* OA images of a mouse kidney section due to incorrect speed of sound selection in the reconstruction. (b) Distortion in the OA reconstructed image of a microsphere introduced by speed of sound inhomogeneity between tissue and coupling medium. The microsphere lies in the focal point of a handheld detector (40 mm radius). C_Couplant and C_tissue are the speeds of sound in the coupling medium and tissue, respectively.

Acoustic reflection in tissue

One of the challenges in OA imaging is the occurrence of reflection artifacts arising from acoustic impedance mismatch between different tissues.

As shown in the schematic in Fig. 3.14a, the OA waves generated from the skin and superficial absorbers propagate through the tissue and are reflected in correspondence with structures with different acoustic impedances. The back-reflected waves, when reconstructed, lead to artifacts in the OA images.

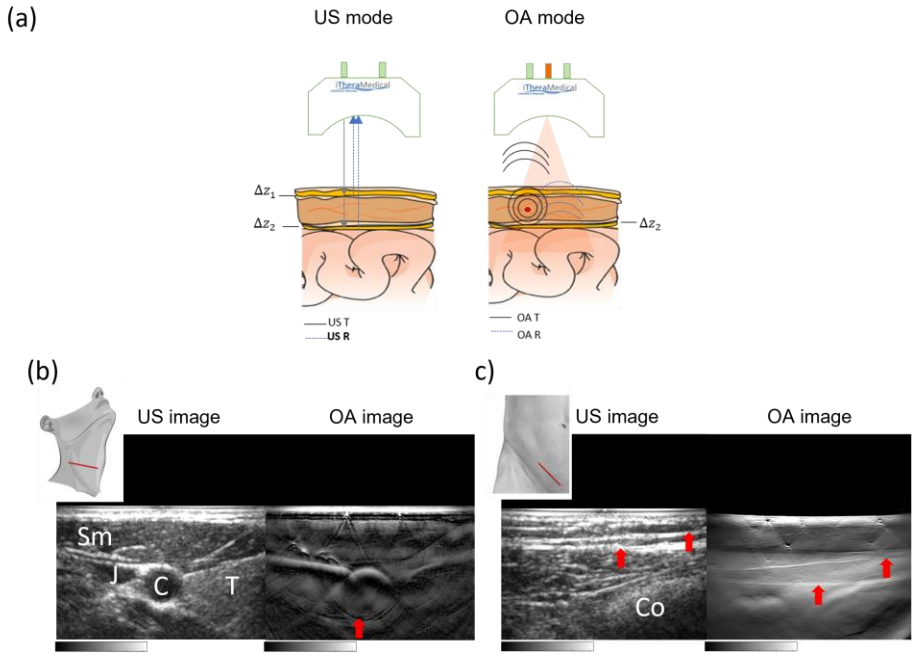

Figure 3.14. Reflection artifacts in clinical OA images. (a) Schematic of acoustic reflection in clinical ultrasound and OA imaging. Reflection artifacts in clinical OA images of (b) longitudinal carotid and (c) abdomen. Carotid (C), Jugular (J), Thyroid (T), Sternocleidomastoid muscle (Sm), Colon (Co).

In small animal OA imaging, strong acoustic reflection artifacts occur in anatomical sections in the proximity of the lungs, intestine, or air cavities. These artifacts are easy to identify, as they result in negative values and appear as fringes or arc artifacts in the reconstructed images [141-142].

However, in clinical images, acoustic reflection has been observed not only in the presence of strong acoustic reflectors (e.g., bones, trachea, or intestine), but also between soft tissues. Fig. 3.14b and c report examples of reflection artifacts (red arrows) in clinical OA images of different anatomical sections of the longitudinal carotid (Fig. 3.14b) and abdomen (Fig. 3.14c). As shown,

acoustic reflection artifacts in clinical images appear as structures of interest in the image field of view and may mislead the image interpretation. Furthermore, since they appear in deep tissue where the OA SNR is very low, these artifacts compromise the signal quantification in regions of interest (ROIs) and limit the imaging penetration depth.

Different methods have been developed in OA images to identify and remove reflection artifacts. Namely, these methods include inducing localized tissue displacement via ultrasound pulse and decorrelating the reflection artifacts [143, 144], weighting the tomographic contribution of each detector with the probability that a signal is affected by acoustic mismatches [145-147], using focused ultrasound or synthetic backpropagation to mimic OA sources and thus identify the reflection artifacts [148], or including multiwavelength spectral information under the hypothesis that the spectrum of OA sources correlates with that of reflection artifacts, which cannot be possible due to light fluence [149]. However, for a variety of reasons, all these methods remain impractical; they may require a well-trained person (for tissue deformation approach), *a priori* knowledge of the OA sources or acoustic reflectors (for focused ultrasound method) or the definition of a threshold (for multiwavelength spectra approach). Furthermore, they are not applicable to real-time applications where identification and removal of reflection artifacts are of fundamental importance to avoid misinterpretation of structures and ultimately misdiagnosis.

3.5 *In vivo* imaging dependency

This chapter illustrates a few practical challenges that can be encountered during *in vivo* imaging that degrade OA image quality.

3.5.1 Position of the organ of interest

Several limitations are encountered when imaging specific organs in OA imaging due to their position and depth, or their proximity to other organs/tissues.

In preclinical images, OA contrast in the mouse brain can be affected by the presence of the skull, which limits light penetration and acoustic wave propagation (1M in Fig. 3.15). Furthermore, the presence of air cavities in the image plane such as lungs (2M in Fig. 3.15) or intestine (5M in Fig. 3.15), can degrade image quality in mouse liver and lower abdomen sections respectively, thus resulting in the appearance of reflection artifacts and dark regions in the image. Low OA contrast

is also expected when imaging anatomical sections with highly absorbing tissue, such as in the liver section (3M in Fig. 3.15), due to light fluence.

In clinical images, the limited view acquisition combined with one-sided illumination and light fluence attenuation can strongly limit the full visibility of organs in the field of view. An example is demonstrated when imaging the carotid artery and the jugular vein in the neck region (3h in Fig. 3.16). These structures exhibit a strong OA signal at the superficial boundary, but this signal decays with depth and thus compromises the integrity and accuracy of the visualized structures. A similar effect has also been observed in OA imaging of muscles (4H in Fig. 3.16), where a large amount of light is absorbed in the superficial layers. This results in saturation of the image's dynamic range and prevents detection of nearby signals from less-absorbing chromophores, i.e., vasculature.

Strong reflection artifacts appear in anatomical sections containing bones, e.g., in the upper or lower extremities (5H in Fig. 3.16), or close to air cavities such as the trachea (2H in Fig. 3.16) and the intestine (6H in Fig. 3.16). Reflection artifacts have also been reported in the abdomen section due to the acoustic mismatch between soft tissues.

Finally, variability among subjects due to factors such as skin type and body type (ectomorph, mesomorph, or endomorph) can also affect image quality in clinical OA imaging.

Therefore, special procedures and image techniques are required to facilitate their visualization. The use of multiple views, ultrasound images guidance, and user's experience can help to resolve some of these ambiguities during image acquisition.

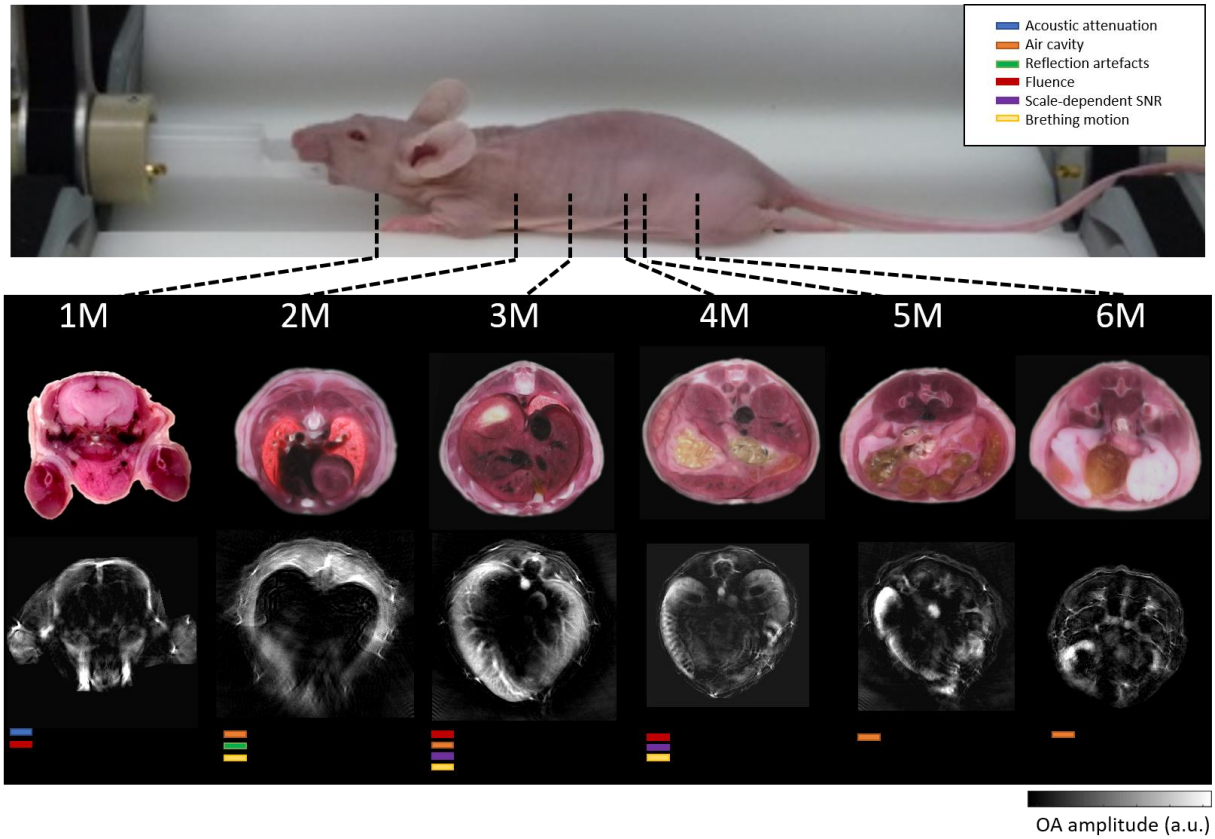

Figure 3.15. Image quality degradation in *in vivo* preclinical imaging. 1M brain section; 2M lungs section; 3M liver section; 4M kidney section; 5M intestine section; 6M lower abdomen section.

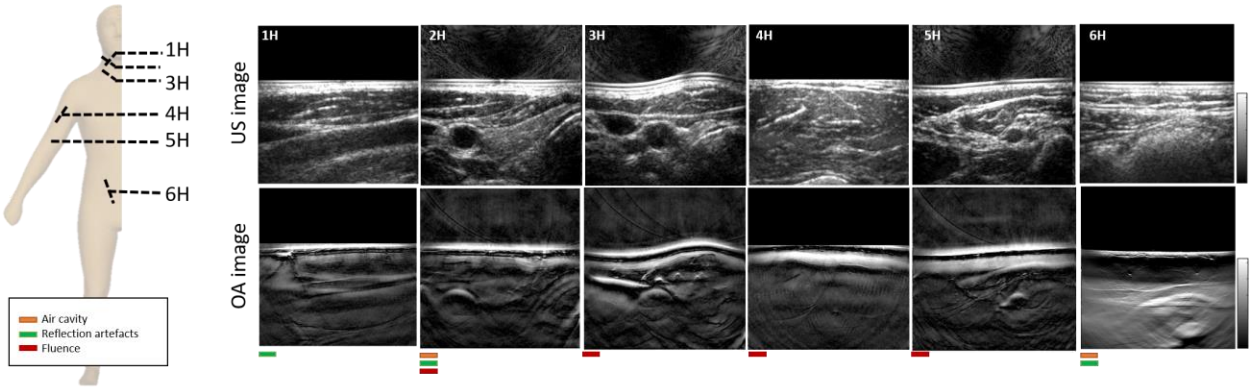

Figure 3.16. Image quality degradation in *in vivo* clinical imaging. 1H transversal carotid; 2H longitudinal carotid, thyroid, and trachea; 3H Jugular and longitudinal carotid; 4H Biceps brachii muscle; 5H Brachial artery; 6H Colon. Presence of hairs

3.5.2 Physiological and functional artifacts

Image artifacts in OA images can arise from physiological and functional activities in *in vivo* imaging. Many of these processes such as cardiac activity, blood circulation, and peristaltic movement – are involuntary and cannot be control by the subject. Therefore, image artifacts are expected in regions close to the chest due to breathing, in regions close to the gastro-intestinal tract due to peristalsis, or in angiographic images due to the pulsatile movement of the arteries.

While physiological changes related to breathing or cardiac cycle typically repeat in a periodic manner and are easy to identify and correct, other physiological and functional processes are more complex and difficult to track due to their variability over time and positions.

3.5.3 Sample preparation

Human and animal safety concerns may require a modification of certain procedures during image acquisition, which could degrade OA image quality. For example, to avoid direct contact between the mouse and the coupling medium in preclinical imaging, the small animal is coupled with ultrasound gel and wrapped in a thin layer of polyethylene membrane. In clinical imaging, the probe is enclosed in ultrasound drapes to avoid direct contact with the patient. Therefore, incorrect mouse preparation or tissue coupling can result in poor image SNR and artifacts. Fig. 3.17a reports an example of image quality degradation in *in vivo* mouse kidney, liver, and lower abdomen sections due to improper coupling (white arrows) and presence of bubbles in the coupling gel (yellow arrows).

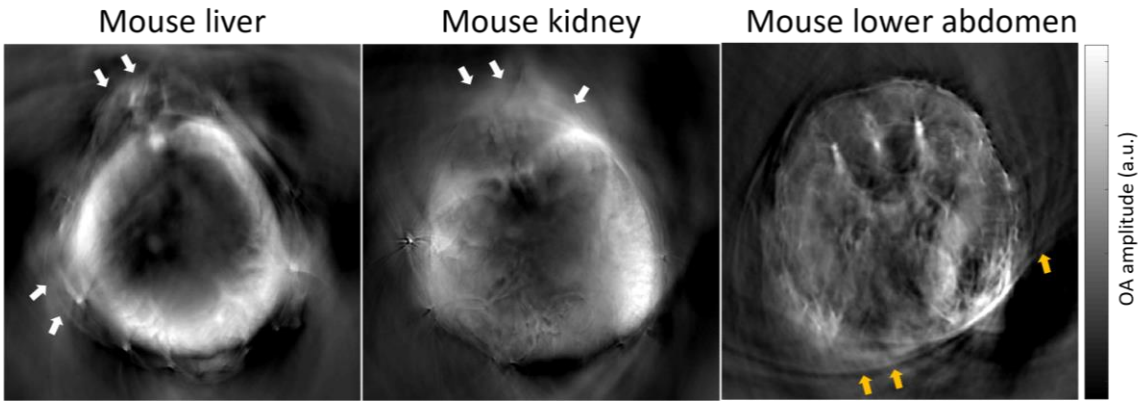

Figure 3.17. Image quality degradation in *in vivo* OA images due to incorrect mouse preparation.

3.6 Conclusions

Image degradation in OA imaging occurs at each level of the imaging chain, from OA signal generation and detection to image visualization. As shown in this section, image quality is often affected by the interplay of many on these sources. It is important to notice that some forms of degradation can be corrected for, e.g., with filters or algorithms, while others cannot. The best approach for image quality improvement is to intervene directly at the source of degradation and prevent it, when possible (e.g., by setting up the experiment correctly and using the best imaging parameters), to avoid propagation and amplification of the errors along the full imaging chain.

4 Proposed image quality improvement approaches

This section illustrates the novel image improvement approaches developed during the course of this thesis. The following proposed methods operate at different levels of the imaging formation chain, from OA signal detection to signal pre-processing and image reconstruction:

1. Transducer optical shielding to improve image quality and SNR in OA tomography (signal detection)
2. Breathing motion quantification and automated correction in preclinical MSOT imaging (signal pre-processing)
3. Disentangling the frequency content in optoacoustic imaging (image reconstruction)

The effectiveness of the proposed methods for visual quality enhancement in OA is demonstrated with both phantoms and *in vivo* experiments. The proposed techniques aim to establish standard methods for visual quality enhancement in OA tomography.

4.1 Transducer optical shielding to improve image quality and SNR in OA tomography

Some of the results presented in this chapter are included in the following patent entitled:

- *"Probe and system for optoacoustic imaging and method for controlling such a probe"* US-2020129074-A1. Stefan Morscher, Josef Konradl, Alexander Urich, Antonia Longo, Patricia Smole.

4.1.1 Introduction

Acoustic detectors employed in typical OA systems are subject to parasitic signals, i.e., OA signals that are generated outside of the measured sample and detected by the same means as the signal of interest.

One key source of parasitic signals in OA imaging is the backscattered light from the excitation pulse, which strongly affects the performance of the detector to accurately acquire OA waves emitted by the sample of interest. The light interference within the ultrasound transducer can have several adverse effects on the acquired OA signals. Among others, these include high amplitude signals that can saturate the detection electronics; generation and propagation of complex acoustic waves along the surface of the detector, i.e., shear waves and shock waves; crosstalk between elements; and thermal effects in the piezocomposite. All these effects lead to artifacts in the reconstructed images, which compromise the image accuracy and its quantifiability.

Common signal and image processing techniques struggle to compensate for those artifacts, as the time of flight and the frequency components of the parasitic signals substantially overlap with the signal of interest. For instance, by filtering certain frequencies, useful information from certain structures of interest can be lost. Furthermore, ad hoc cutoff frequencies should be selected for each detector and each measurement, since the parasitic noise may vary from one detector to another due to different circumstances (e.g., detector manufacturing, detector position, selected wavelength, or laser energy), thus rendering these techniques impractical.

While model-based reconstruction algorithms can partially solve the problem, the low computational speed of these algorithms limits their use in real-time applications. This is crucial for the clinical handheld systems, where the real-time feedback to the operator is essential to enable fast localization of the anatomical region of interest.

Therefore, to overcome these limitations, transducers with an optical coating have been employed to reduce parasitic noise and improve OA signal detection in real-time [150-152]. However, the improvement has only been tested qualitatively.

Herein, we investigate and quantify the parasitic noise generated by the light interference within the transducer in handheld OA detectors and evaluate their effect on OA signal detection and reconstructed images. We propose and test different transducer optical shielding configurations to

reduce parasitic noise while maintaining the acoustic performance of the detector. We demonstrate that the new transducer design reduces image artifacts and provides a two-fold SNR enhancement, which results in substantially increased image contrast in real-time clinical applications.

4.1.2 Light interference within the transducer

Optimal handheld probes for OA clinical applications feature curved acquisition geometry and incorporate the light delivery system in the same compartment (Fig. 4.1a). Thus, an acoustic coupling medium that is acoustically and optically transparent is required to propagate the generated OA signal from the tissue to the ultrasound sensing element. The system is then confined in a membrane to avoid leakage of the coupling medium into the tissue. Acoustic waves generated in tissue propagate backwards through the transducer-matching layer and are converted into electric signals by the transducer piezocomposite.

However, an amount of light delivered into the tissue is backscattered and interferes with the detector, generating parasitic signals that are also detected by the transducer and converted in electrical signals. While primary parasitic signals are often easy to understand based on their geometry and travel time, some of them produce secondary effects that are very hard to understand and correct.

Fig. 4.1b shows an example of parasitic signal in the detected OA signal from a single transducer. First, the excitation energy is deposited on the surface of the acoustic transducer at the interface of the imaged tissue and generates a direct OA signal. The resulting detected signal is characterized by a high amplitude oscillating signal called the First Arriving Signal (FAS) whose frequency spectra resample the frequency response of the transducer (1 and blue box in Fig. 4.1b), followed by low frequencies oscillations that contribute to the complete duration of the OA recording (2 and red box in Fig. 4.1b). While the former can saturate the data acquisition systems, the latter has a direct effect on the OA signal in the field of view (Fig. 4.1b) and can result in spurious negative values in the reconstructed images. Yet, identifying the sources of these low frequencies oscillations is difficult due to the interplay between different physical phenomena, i.e., complex acoustic propagation and thermal effects in the piezocomposite.

Second, the OA signal generated from the transducer surface propagates through the tissue and is reflected at the membrane-tissue interface due to acoustic mismatch. The reflected waves are acquired at double the travel distance between the transducer and the membrane (3 in Fig. 4.1b)

and result in an arc artifact in the bottom part of the reconstructed image, thus limiting the image penetration depth.

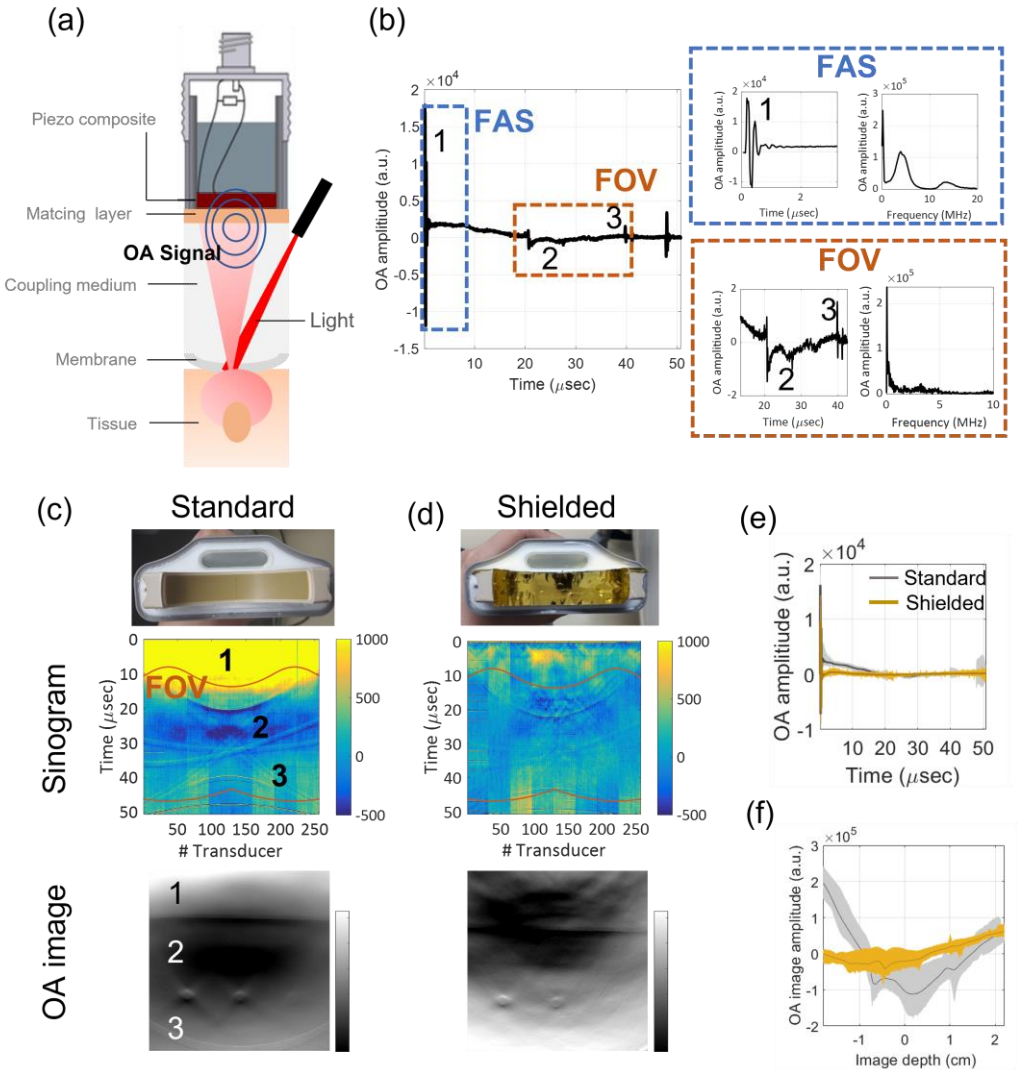

Figure 4.1. Light interference within the transducer. (a) Schematic of the light interference within the transducer in the handheld probe. A fraction of light is reflected at the tissue surface and interferes with the transducer, leading to parasitic noise in the detected OA signal. (b) Parasitic signal detected from a single transducer, showing the first arriving signal (1, FAS), the low frequency oscillations in the field of view (2, FOV) and the reflection artifact (3, FOV). Magnification of the signals in time and frequency domain. (c) Parasitic signal in the sinogram and in the reconstructed OA image of a phantom. (d) Improvement in the sinogram and in the reconstructed image of the phantom by optically shielding the transducer with a space blanket. (e) Comparison of the detected OA signal from a single transducer before and after shielding. (f) Comparison of the OA amplitude image profile before and after shielding, demonstrating a reduction in negative values after transducer shielding.

Fig. 4.1.c shows an example of parasitic signals in the sinogram and in the reconstructed image of an OA phantom mimicking bulky breast tissue, with three transversal inclusions acquired with a handheld detector (MSOT Acuity Echo system). As demonstrated here, the first arriving signals (1), the low frequencies oscillations (2) and the reflected OA signals (3) are respectively projected in the image domain as high OA values in the coupling medium, low frequencies negative values in the first 1.5 cm of the tissue, and an arc artifact in the bottom part of the field of view.

Fig. 4.1d shows the improvement in the sinogram and in a reconstructed image of the phantom after applying an optical shielding layer on the transducer surface, in this case a space blanket. Notably, the parasitic signals in the OA signal are reduced after transducer shielding (Fig. 4.1e). Furthermore, the OA image amplitude profiles in Fig. 4.1f show a substantial reduction in negative values after shielding.

4.1.3 Methods

Transducer optical shielding

The preliminary results reported in Fig. 4.1d drove the requirements for a new transducer design with optical shielding to reduce parasitic signals. To remove parasitic signals, the ideal detector for OA applications should: 1) have high optical reflectivity to reduce absorption of the light at the transducer surface; 2) have low optical transmission to avoid electromagnetic interference between the light and the piezocomposite; 3) be acoustically transparent to acoustic wave propagation.

For this purpose, different transducer coating materials and transducer mock-ups were tested to evaluate the best OA performance for the final handheld transducer array. Three different coating materials – gold (Au), silver (Ag) and a new orange pigmented material (O 2ML) – were considered for optical shielding of the transducer (Fig. 4.2a) and compared with a standard matching layer material (Standard). Metalized coatings with gold and silver were selected accordingly due to the high optical reflectance of these two materials in the NIR and obtained by physical vapor deposition of 1 µm layer of metal on the transducer matching layer.

First, the optical properties (i.e., optical transmission and reflection) of the different coating materials were measured in the wavelength range 660-980 nm, which is the typical range used in MSOT. The optical transmission was calculated by measuring the amount of laser energy transmitted though the material samples via an energy meter (EnergyMax-USB J-25MB-HE,

Coherent, Germany). The optical reflection was estimated using a commercially available device (Mountain Photonics GmbH, Germany).

Afterwards, the OA performance of each mock-up with different coating materials was tested. Fig. 4.2d shows the measurement setup used for the characterization including the mock-up (MU), the laser fiber for direct illumination of the sample, and an external transducer (ET, IW-5-10 5MHz transducer, Sonotec GmbH, Germany) located at 2 cm distance from the mock-up. The mock-up and the external transducer were connected to an oscilloscope to measure respectively the parasitic signals acquired on the mock-up due to direct illumination and the OA signal generated by the mock-up that propagates towards the external transducer. All the experiments were conducted in water and the laser wavelength was fixed at 800 nm.

OA characterization of the gold coated transducer array

Due to the higher optical shielding properties, the gold-coated configuration was chosen for the final transducer handheld design, and the sensitivity field of the array before and after coating was tested. The sensitivity field for both configurations was measured by illuminating a single polyethylene microsphere of 100 µm in certain position of the field on view and by plotting the energy of the detected OA signal. The array was moved in different positions to cover a field of view of 30 mm x 30 mm centered on the geometrical focus of the array (40 mm distant from each element), for a total of 9 x 9 grid locations.

Phantom and *in vivo* experiments

To systematically quantify the OA performance of the gold-coated transducer versus the standard one, two different OA phantoms – one mimicking muscle tissue and the other mimicking breast tissue at 800 nm– were considered (Fig. 4.4a). Transparent tubes with 3 mm diameter were positioned at different depths (5mm, 8 mm, 13 mm,18mm, 23mm and 28 mm) to simulate transversal blood vessels, as reported in Fig. 4.4b. The OA phantoms were produced with 3% (w/v) agar (Fluka Analytical, Germany) and 6% (v/v) intralipid (20% stock solution; Sigma Aldrich, Germany), which together show similar scattering properties as the average tissues (~10 cm^{-1}); Indian ink (Higgins Ink, Leeds, MA, USA) was added to the agar to tune the optical absorption to match the different tissue types, i.e., of breast, muscle and blood at 800 nm. The optical properties of the different tissues ($\mu_a + \mu_s'$) and the relative OD at 800 nm are reported in Fig. 4.4c.

OA signals of the phantoms were acquired at 800 nm with the commercially available MSOT Acuity Echo (iThera Medical, Munich, Germany) and a handheld detector before and after coating. The images were reconstructed using a standard back-projection algorithm.

In vivo OA and ultrasound images of different human anatomical sections (carotid, arm, and abdomen) were acquired to evaluate the image quality improvement on clinical images.

4.1.4 Results

Transducer optical shielding

Fig. 4.2b, c shows the optical properties (i.e., optical transmission and reflection in the wavelength range 660-980 nm) for the different proposed coating materials of the transducer. As expected, the standard matching layer material shows poor optical shielding, with the highest optical transmission (43 % at 800 nm) and the lowest optical reflection (only 52% at 800 nm). The gold coated sample performs the best with the lowest optical transmission (only 0.9% at 800 nm) and the highest optical reflection (88% at 800 nm), followed by the silver and the orange pigmented samples (see Table 1). In particular, the metallic coating reduces the optical transmission by -32 dB and increases the optical reflection by +4 dB at 800 nm.

After assessing the optical properties of the different coating materials, the corresponding transducer mock-ups were tested, and the parasitic signals generated by the direct illumination of the mock-ups were compared.

The measurements from the mock-up and the external transducer were collected to measure the parasitic signals on the mock-up (Fig. 4.2e) and the OA signals generated by the mock-up that propagate towards the external transducer (Fig. 4.2f), respectively.

The optical shielding of the transducer demonstrably reduces the parasitic signals when compared with the standard transducer, with the gold coated transducer performing the best, followed by the silver coating. Notably from Fig. 4.2d, the amplitude of the first arriving signal (FAS) is reduced by -11 dB with the gold coating (OA signal on MU in Table 2), and the low frequency oscillations that noticeably affect the acoustic detection in the standard transducer configuration are removed after shielding. As expected, a reduction in the generated OA signal from the shielded mock-ups is also detected by the external transducer (Fig. 4.2e and Table 2) by approximately -15 dB for both metallic coatings silver and gold.

Although the gold- and silver-coated transducers perform similarly well on reducing the FAS and the low frequency components, the gold-coated transducer was chosen for the final handheld array configuration due to higher stability on ultraviolet light and water exposure (i.e., an aging test).

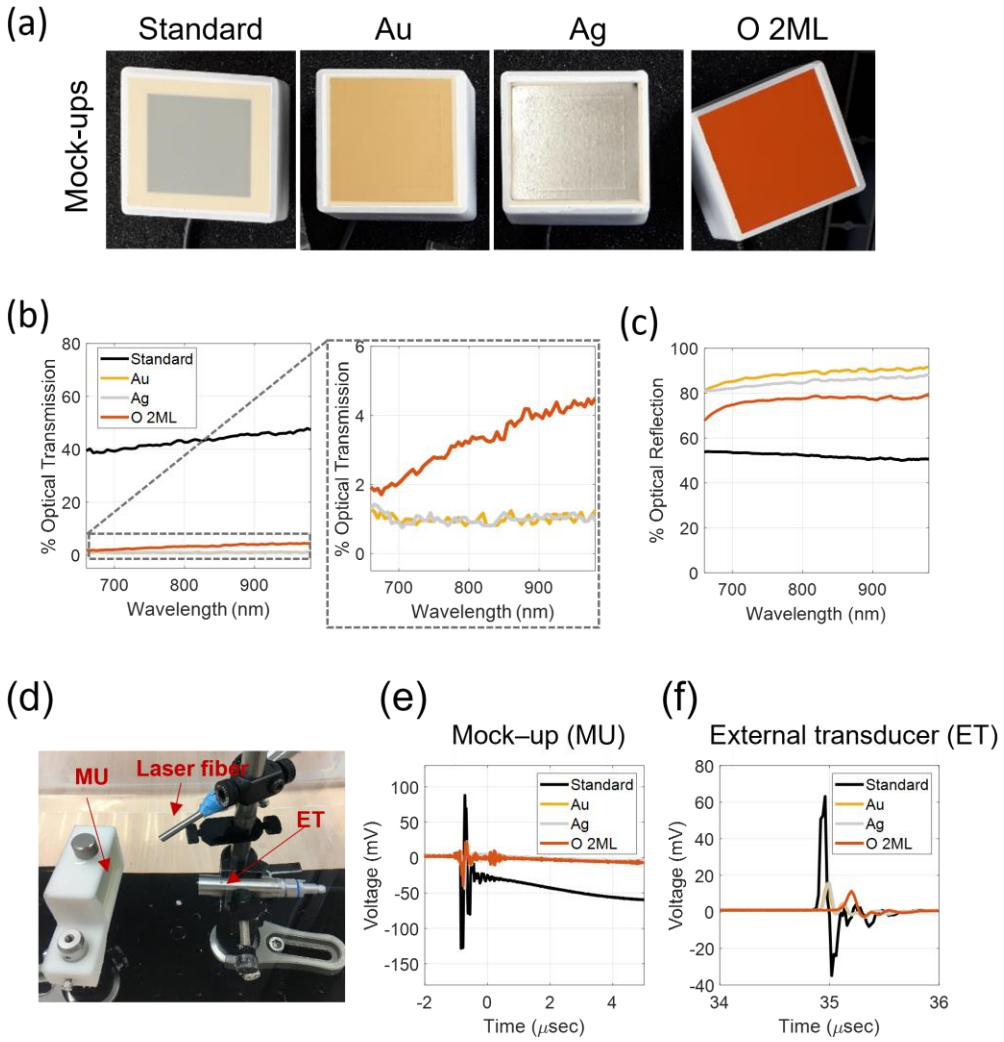

Figure 4.2. Transducer optical shielding. (a) Transducer mock-ups with different coating materials: standard, gold (Au), silver (Ag) and orange pigmented material (O 2ML). (b) Optical transmission and (c) optical reflection of the different transducer coating materials in the NIR 680-980 nm. (d) Measurement setup for the characterization of the mock-ups (MU), including a laser fiber for direct illumination of the sample and an external transducer (ET) for generated OA signal detection. (e) Direct OA signal detected on the mock-ups due to illumination of the sample and (f) OA signal generated by the mock-ups and acquired by the external transducer.

@ 800nm	Standard	Au	Ag	O 2ML
Transmission (%)	43	0.9 (-32.7dB)	1 (-32.6dB)	3.2 (-22.4dB)
Reflection (%)	52	88(+4.6 dB)	84(+4.2 dB)	76 (+3.3dB)

Table 1. Optical properties of different transducer coating materials at 800 nm. The comparison with the standard transducer is reported in parentheses.

Vpp (mV) @ 800 nm	Standard	Au	Ag	O 2ML
OA signal on MU (FAS)	216	54 (-11dB)	66 (-10dB)	103 (-6dB)
OA signal on ET	97	18 (-14dB)	18 (-14dB)	13 (-16dB)

Table 2. OA signal detected on the mock-ups (MU) and OA signal generated by the mock-ups and detected by the external transducer (ET) at 800 nm. The comparison with the standard transducer is reported in parentheses.

OA performance of the gold coated transducer

Fig. 4.3a shows the gold coated transducer array (Gold) for handheld systems, which was fabricated through physical vapor deposition of 1 µm layer of gold on the standard transducer (Standard). The OA performance of the transducer array (frequency response and sensitivity field) were tested before and after metallization.

Fig. 4.3b shows the frequency response of the single transducer element in receive mode obtained from the KLM model before (black curve) and after (yellow curve) gold deposition. Although the central frequency of the transducer is decreased by -2.9% after metallization (from 3.39 MHz to 3.29 MHz) and the sensitivity of the transducer is slightly reduced at the higher frequencies above 5 MHz, no substantial difference was reported for the transducer bandwidth after coating.

Fig. 4.3c reports the comparison of the acoustic sensitivity field for a single transducer element of the array before and after gold coating. The sensitivity field of the coated transducer at -6dB (FWHM) shows no differences compared to the uncoated transducer (31.5 mm). However, a -12% average reduction in sensitivity was measured from the transducer array after gold coating.

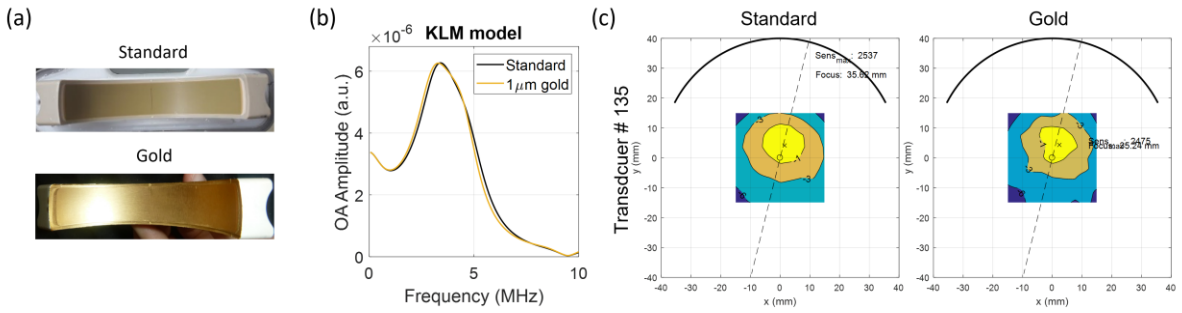

Figure 4.3. OA characterization of standard vs. gold coated transducer array. (a) Standard and gold coated transducer array. (b) Electrical impulse response estimated from the KLM model. (c) Sensitivity fields of a single transducer element before and after gold coating (element 135), with a FOV of 30 mm x 30 mm centered in the focal point of the array.

Image quality and SNR improvement in OA phantoms

Fig. 4.4d shows the OA reconstructed images for the two phantoms mimicking breast and muscle tissue with blood inclusion at 5 and 23-mm depth. From the reconstructed images, three different metrics were extrapolated to quantify image quality improvement at different depths introduced by the transducer optical coating (Fig. 4.4e): mean OA amplitude intensity in the inclusion (OA Intensity); SNR estimated as the mean OA amplitude intensity in the inclusion divided by the standard deviation of the noise; contrast to noise ratio (CNR) estimated as the difference between the inclusions and the signal background and divided by the standard deviation of the noise.

As expected, a decrease in the OA intensity, SNR and CNR is observed with increasing depth of the inclusions for both coated and uncoated transducers. However, a two-fold SNR and CNR improvement is reported after coating for both phantoms. The mean increase in SNR at depth was reported to be +8.6 dB for breast and +10.9 dB for muscle, while the CNR increased by + 5.5 dB in breast and +1.6 dB in muscle. The phantom experiments demonstrated that image contrast, SNR, and penetration depth substantially increase after optical coating of the transducer.

Image quality improvement in *in vivo* clinical imaging

To evaluate the image quality improvement in clinical application of the new coated transducer compared with the standard one, OA and ultrasound images of three different anatomical sections were considered: the neck region with the carotid, the upper arm with muscle, and the abdomen with the intestine wall.

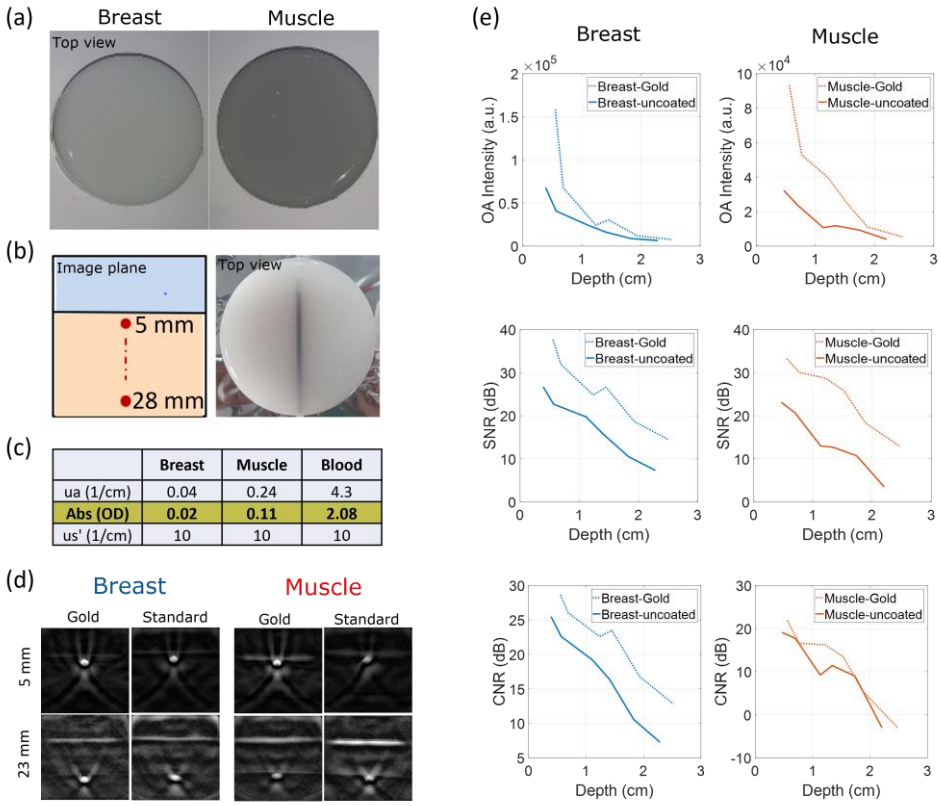

	Breast	Muscle	Blood
ua (1/cm)	0.04	0.24	4.3
Abs (OD)	**0.02**	**0.11**	**2.08**
us' (1/cm)	10	10	10

Figure 4.4. Performance of the gold coated transducer array on OA phantoms. (a) OA phantoms simulating breast and muscle bulky tissue (Top view). (b) Schematic of the phantoms in the image plane with inclusions at different depths and top view of the breast phantom with the inclusion. (c) Optical properties of the phantoms, inclusions (Blood) and bulky tissues (Muscle and Breast). (d) OA reconstructed images for breast and muscle phantoms with the inclusion at 5- and 23-mm depth acquired with the standard and gold coated transducer. (e) OA intensity, SNR, and CNR of the inclusions at different depths before and after gold coating.

The effectiveness of the new transducer design was tested by comparing the acquired sinograms as well as the OA reconstructed images before and after optical coating.

Fig. 4.5a shows the reduction in the FAS and the suppression of the low frequency oscillations in the OA signal after transducer coating. As expected, the sinogram acquired with the gold coated transducer in Fig. 4.5c is less noisy compared to the one acquired with the standard transducer in Fig. 4.5b, and the OA signals from structures of interest in the field of view (red arrows) are enhanced after low frequencies oscillations removal.

Fig. 4.5d reports the reconstructed OA and ultrasound images from different anatomical sections acquired with standard and gold coated transducer. While ultrasound image quality remained unaltered after coating, a substantial improvement is observed for OA images. Notably, OA images acquired with the gold coated transducer show higher contrast, SNR, and penetration depth as well as lower artifacts.

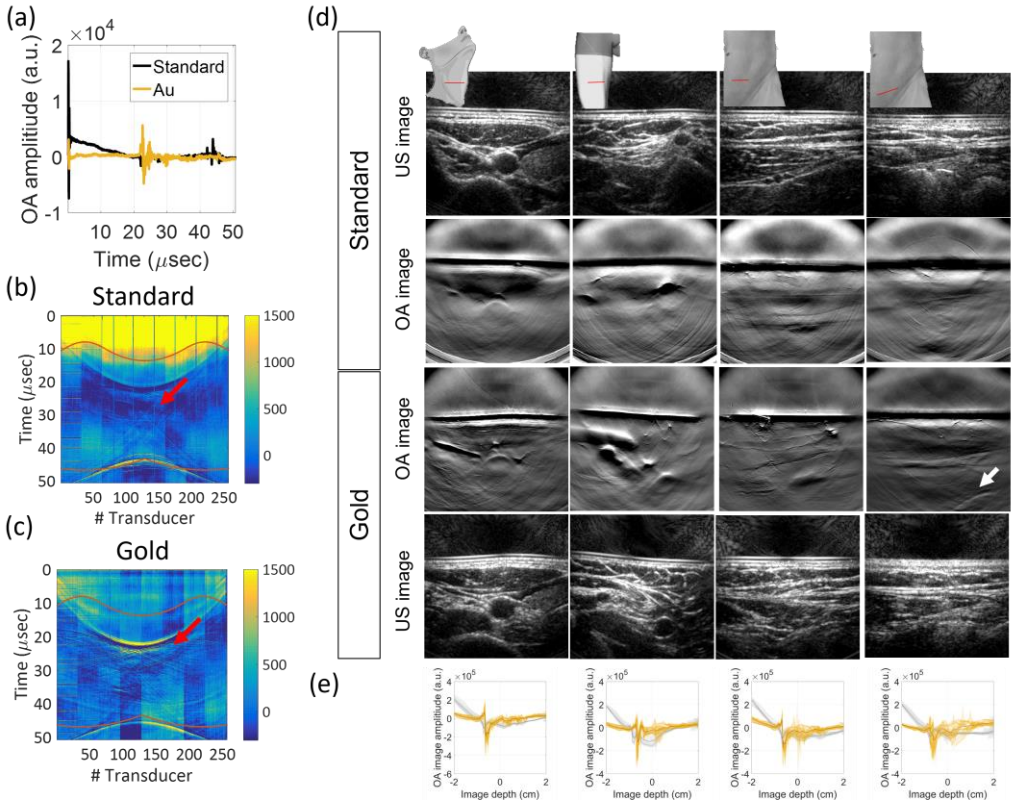

Figure 4.5. Signal and image quality improvement in clinical OA images. (a) Comparison of the acquired OA signal from before and after gold coating showing parasitic noise reduction and signal enhancement. Examples of sinogram from the abdomen section acquired with (b) a standard transducer and (c) a gold coated array. (d) Ultrasound and OA reconstructed images for different anatomical sections (left to right: carotid, arm, and two positions of the abdomen) acquired before and after gold coating. White arrow indicates the intestine wall at 3 cm depth. (e) OA image amplitude profiles along the depth showing negative value reduction in the image field of view after gold coating (yellow curve).

Specifically, anatomical structures of interest – which are otherwise hidden by low frequency parasitic signals – are enhanced. Arc artifacts that are otherwise particularly noticeable in the

second half of the image field of view with the standard transducer are suppressed when using the gold coated transducer. Deep structures, e.g., intestine wall at 3 cm depth, are clearly visible with high contrast. Better quantifiability of the field of view is also demonstrated, with a reduction in negative values in the reconstructed images as shown from the OA amplitude image profile in Fig. 4.5e.

4.1.5 Discussion and Conclusions

In this work, a series of experiments have been performed to investigate the effect of parasitic signals due to light interaction within the transducer in the acquired OA signals and reconstructed images.

Different materials and transducer mock-ups were explored to reduce parasitic signals in the detected OA signals. Different methods were developed to test the optical and OA performance of the mock-ups, which have shown that both metallic coating and pigmentation of the matching layer are efficient to reduce parasitic signals. This is accomplished by reducing light transmission and absorption at the transducer surface without changing the acoustic behavior of the detector. The gold metallization was chosen for its high durability against ultraviolet light and water exposure.

Therefore, a first prototype of an array with gold coating was realized and tested. It was shown that the electro-acoustic behavior and the sensitivity of the transducer in receive mode were only slightly impacted by the metallization. However, measurements on OA phantoms demonstrated a two-fold SNR and image contrast improvement compared to the standard transducer array. This enhancement was then translated in OA clinical images to allow a better capacity to visualize and recognize structures of interest. Notably, due to the high reflectivity of the gold coating, the optical energy that is delivered to the tissue is maximized. This increases the penetration depth of the imaging system, as already reported in [153]. Furthermore, less negative values in OA images were also reported after gold metallization, thus improving the quantifiability of the entire field of view.

In summary, a new transducer design for OA applications to remove parasitic signals is proposed in this work. Results on clinical OA images clearly showed that the new design has the potential to provide clinically valuable enhancement compared with standard handheld transducers by reducing parasitic noise and simultaneously increasing both SNR and image penetration depth.

Further envisioned technical advancements described here are aimed towards more quantitatively accurate analysis.

4.2 Breathing motion quantification and automated correction in preclinical MSOT imaging.

4.2.1 Introduction

Commercially available OA systems for small animal imaging usually operate at 10 Hz frame rate and require several laser pulses to collect multiple images. Since breathing in mice appear at a rate of up to 3 Hz, acquired images are often affected by motion artifacts that lead to 1) image blurriness and resolution loss, and 2) inaccurate quantification.

Fig.4.6a reports the OA images of the mouse chest, kidney, and lower abdomen sections acquired at two breathing points of exhalation and inhalation. These images demonstrate that, depending on the relative position to the lungs, OA images can be differently affected by breathing motion artifacts. Anatomical regions close to the chest are more affected by respiratory motion, and this is demonstrated by the low structural similarity index of 0.11 between the images acquired at the two different breathing points. On the other hand, anatomical sections in the lower abdomen are less prone to breathing artifacts, as indicated by a higher structural similarity index of 0.71 between images acquired at the two respiratory acts.

In applications where multi-frame image analysis is required - such as for 3D whole-body imaging, multispectral analysis, or temporal analysis - the tissue is excited by multiple pulses, and each image is acquired at a different point in the mouse's breathing cycle. Thus, breathing motion correction is essential to improve not only image quality but also signal quantification and interpretation.

Furthermore, breathing motion correction is necessary in applications that require frame averaging to increase image SNR. While increasing the OA image frame rate (e.g., by increasing laser pulse repetition rate) could solve the breathing motion problem in living subjects, this is limited by the laser safety regulations on light deposition inside the tissue and by hardware constraints. Furthermore, in hybrid OA systems where ultrasound imaging is also integrated, the data acquisition speed is further slowed down.

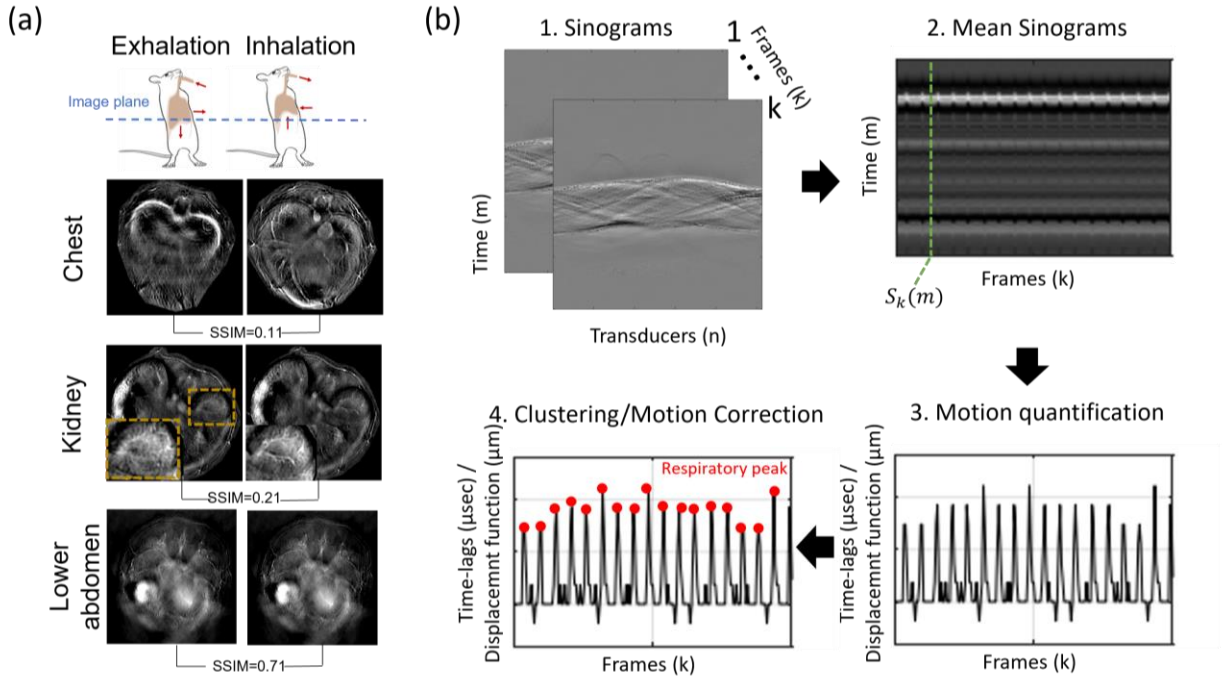

Figure 4.6. Breathing motion artifacts in *in vivo* OA images of mouse. (a) Acquired OA images of the chest, kidney, and lower abdomen at two breathing phases (exhalation and inhalation), showing breathing motion artifacts in different anatomical sections. Structural similarity index (SSIM) between the OA frames acquired at the two breathing points to quantify breathing motion artifacts is also indicated. (b) Schematic of proposed breathing motion correction algorithm.

Therefore, different retrospective approaches have been proposed to remove breathing motion artifacts by monitoring the mouse breath either directly [154] or indirectly [155, 156] and by clustering the acquired frames to a specific breathing cycle. While these methods successfully report 2D and 3D OA image quality improvement in terms of image sharpness, to date there are no studies that have also assessed SNR and image quantification improvement for the following applications: 1) spectral quantification, 2) spectral unmixing, and 3) temporal analysis (e.g., kinetics of exogenous contrast agent). Therefore, an algorithm that is fully automated, can be applied on different acquisition schemas, and is independent from the anatomical section and wavelengths is required.

Herein, a new breathing motion correction algorithm that is flexible with respect to different acquisition methods is proposed. The underlying hypothesis is that breathing movements in mice

result in a displacement of the acquired OA signals between sinograms. Therefore, by measuring the phase-lags between a reference sinogram and the others acquired at different time points, it is possible to track and quantify breathing motion and ultimately correct for it. Hence, the acquired sinograms are sorted and clustered according to the respiratory phase, and the OA images of the animal at each breathing cycle are subsequently reconstructed from the corresponding cluster.

The performance of the new algorithm was evaluated for different OA applications. First, we demonstrated that breathing motion correction improves OA image quality by increasing image SNR and image sharpness. Next, we demonstrated quantification improvement on multiwavelength datasets by comparing the OA spectrum and spectral unmixing before and after breathing motion correction. Finally, we showed that breathing gating improves temporal analysis in OA, thus enabling visualization of dynamic phenomena, such as physiological changes as well as kinetics or uptake of contrast agents.

4.2.2 Methods

Breathing motion quantification and correction

The new proposed algorithm aims to quantify and correct breathing motion in living mice from the acquired OA signals. A schematic of the breathing motion quantification and correction algorithm is reported in Fig. 4.6b. The acquired signals are generally arranged into sinograms, where every sinogram represents a single frame. Each sinogram consists of a matrix $m \times n$, with m rows representing the time-samples of each signal and n columns representing the n^{th} transducer of the array.

For a fixed transducer position and for a fixed wavelength, k consecutive frames are acquired over time. A minimum number of 15 frames must be acquired to adequately capture a complete breathing cycle and correct for breathing motion. The algorithm is structured as follows:

1) For each acquired sinogram that corresponds to a single frame, the mean value of the sinogram along the columns (transducers) is estimated. Therefore, each frame is represented with the mean sinogram, which is a vector with dimension $m \times 1$.
2) For a fixed transducer position and for each wavelength, the k vectors containing the mean sinogram are rearranged into a 2D matrix $m \times k$. This represents the entire sequence of k frames acquired at each transducer position for each wavelength.

3) The first mean sinogram is taken as the reference, and the time-lags $\tau_{estimated}$ between the reference and the (k - 1) mean sinograms are estimated from the cross-correlation functions as follow:

$$Corr(\tau) = \sum_{t=0}^{m-1} s_1(t)\, s_k(t-\tau) \quad (4.1)$$

$$\tau^* = arg\, \max_{\tau}(Corr(\tau)) \quad (4.2)$$

For breathing motion quantification, the displacement function is estimated by multiplying the time-lags τ^* for the average speed of sound in tissue (1480 m/sec).

4) For motion correction, the temporal positions and the frames corresponding to the respiratory peaks are identified from the plot of the time-lags τ^* as those with greater displacement values than the others.
5) The other frames are clustered and sorted accordingly with the respiratory peaks.
6) The frames corresponding to the same breathing phase, e.g., expiratory pause, are selected for multiframe analysis while the others discarded.

For 3D whole-body imaging or multiwavelength acquisition, the algorithm is iterated respectively along the different transducer positions or different wavelengths.

In vivo experiments

In vivo OA images were acquired using the small animal scanner device (inVision 256-TF, iThera Medical GmbH, Munich, Germany) at a frame rate of 10 Hz. All acquired data were filtered using a digital bandpass filter between 300 kHz and 8 MHz and reconstructed using a conventional back-projection algorithm.

OA images with different acquisition schemas were collected to demonstrate the robustness of the algorithm when used in different OA applications:

1) 3D whole-body imaging. OA signals from consecutive cross sections from the brain to the lower abdomen were acquired continuously at a single wavelength (800 nm) with 200 µm distances between consecutive cross sections and 20 repetitions for each cross section.
2) Multiwavelength acquisition. OA signals from single anatomic section were acquired at 12 different wavelengths (700, 740, 760, 780, 800, 820, 860, 900, 930, 950, 970 nm) with 15 repetitions for each wavelength.

3) Temporal acquisition. The kinetics of an exogenous contrast agent, i.e., gold nanoparticles (AuNPs), was considered for this application. OA signal from a single anatomic section was continuously acquired at a single wavelength (780 nm, peak absorbance of the contrast agent) before (3 minutes), during (15 sec) and after (6 minutes) 40 µL contrast agent injection.

The motion correction algorithm was applied to the acquired dataset and its performance was quantified. Different metrics were used to quantify image quality and quantification improvement accordingly with the various OA applications.

The structural similarity index (SSIM) was used as a metric to quantify the breathing motion artifacts between reconstructed images of the same cross section acquired at different time breathing points. Image SNR and image sharpness were selected to compare images before and after breathing motion correction and quantify image quality improvement.

OA spectra and oxygen saturation (sO2) values in different ROIs before and after breathing motion were used to assess image quantification improvement, while OA amplitude fluctuation (i.e., standard deviation) was used to quantify the improvement after breathing motion correction for temporal analysis.

For sO2 quantification, the linear unmixing algorithm was used to extrapolate the oxyhemoglobin (HbO2) and deoxyhemoglobin (Hb) absorption maps from multiwavelength acquisitions (see Sec. 2.2.3.2), and the sO2 map was estimated from the equation:

$$sO_2 = \frac{C_{HbO_2}}{C_{HbO_2}+C_{Hb}} \tag{4.3}$$

where C_{HbO_2} is the concentration of HbO2 and C_{Hb} is the concentration of Hb.

4.2.3 Results

Breathing motion quantification

Fig. 35a reports the breathing motion artifacts and quantification in OA whole-body mouse imaging. As expected, the breathing motion results in a displacement of the OA signals in the sinogram, and the amount of motion-related artifacts increases with proximity to the lungs. The displacement function employed in Fig. 4.7a quantifies breathing motion in different mouse

anatomical sections and reports an average value of movement of 900 μm in the chest region, 300 μm in the head and neck region, 250 μm in the abdomen, 200 μm in the pelvis and lower extremities. The Fourier transform of the displacement function in Fig. 4.7a shows the respiratory frequency of ~ 1 Hz and its harmonics.

Fig. 4.7b, c report the breathing motion quantification for multiframe single wavelength and multiframe multiwavelength acquisition, respectively. Based on the displacement functions, the implemented breathing motion correction algorithm sorts and clusters the acquired frames to the respective breathing phase, i.e., the respiratory peaks correspond to points of the maximum displacement and respiratory pauses correspond to the minimum displacement. Notably, for multiwavelength acquisition, the respiratory frequency and its harmonics in the spectra are modulated for the laser wavelength switching.

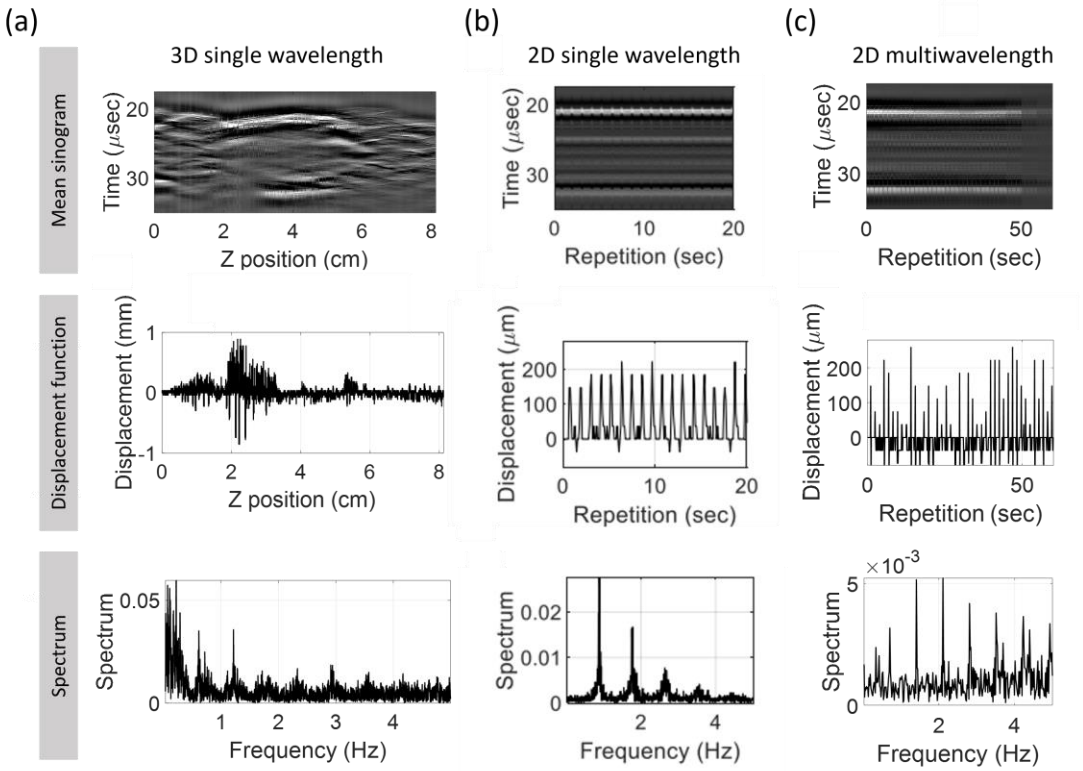

Figure 4.7. Breathing motion quantification for different OA acquisition schemas: (a) 3D and (b) 2D single wavelength acquisition, and (c) 2D multiwavelength acquisition. For each OA acquisition schema, the sinogram (mean sinogram), the displacement function, and their Fourier transform (Spectrum) are shown.

Breathing motion correction for OA image quality improvement

The effectiveness of the breathing motion correction algorithm to improve image quality and SNR was first demonstrated on 2D OA images of a mouse kidney section. Fig. 4.8a shows the OA image of the mouse kidney section acquired during the expiratory pause (Reference), which is taken as the reference, and compared with the OA images obtained by averaging all consecutive frames (Av. Cons. frames) or only the selected frames at the expiratory pause (Av. Selected frames).

The averaging of consecutive frames (Av. Cons. frames) results in substantially increased image blurriness due to destructive interference when frames from different points in the mouse breathing motion are averaged, while the averaging of the selected frames (Av. Selected frames) results in improved image sharpness. As exemplified in Fig 4.8a, the small vasculatures in the right kidney (red arrows) can be nicely distinguished after breathing motion correction but appears smeared in the OA image obtained from consecutive frames. The rejected frames image reveals artifacts responsible for distorting the consecutive frames image.

This observation is also confirmed by the higher entropy index of 0.03 measured in the selected frames image (and equal to the single frame image), compared with the lower ones measured in the consecutive frames image (0.028) and the rejected frames image (0.01).

Similarity, it is demonstrated that the motion correction algorithm strongly enhances SNR of anatomical structures. The positive difference between the selected frames image and the rejected frames image (Selected-Rejected>0) shows the gain in SNR introduced by breathing motion correction, from 2.1 to 2.48 dB. Furthermore, averaging selected frames also results in enhanced SNR when compared with single frame imaging, from 2.27 to 2.48 dB.

Image quality improvement was then demonstrated on 3D mouse whole-body imaging. Fig. 4.8b reports the 3D maximum intensity projection (MIP) OA image of a mouse with chessboard artifacts due to breathing motion, and the artifact-free 3D MIP OA image obtained after breathing motion correction. Notably, while the vertical vessels appear disrupted in the consecutive frames image, they appear regular and continuous in the selected frames image (yellow arrows).

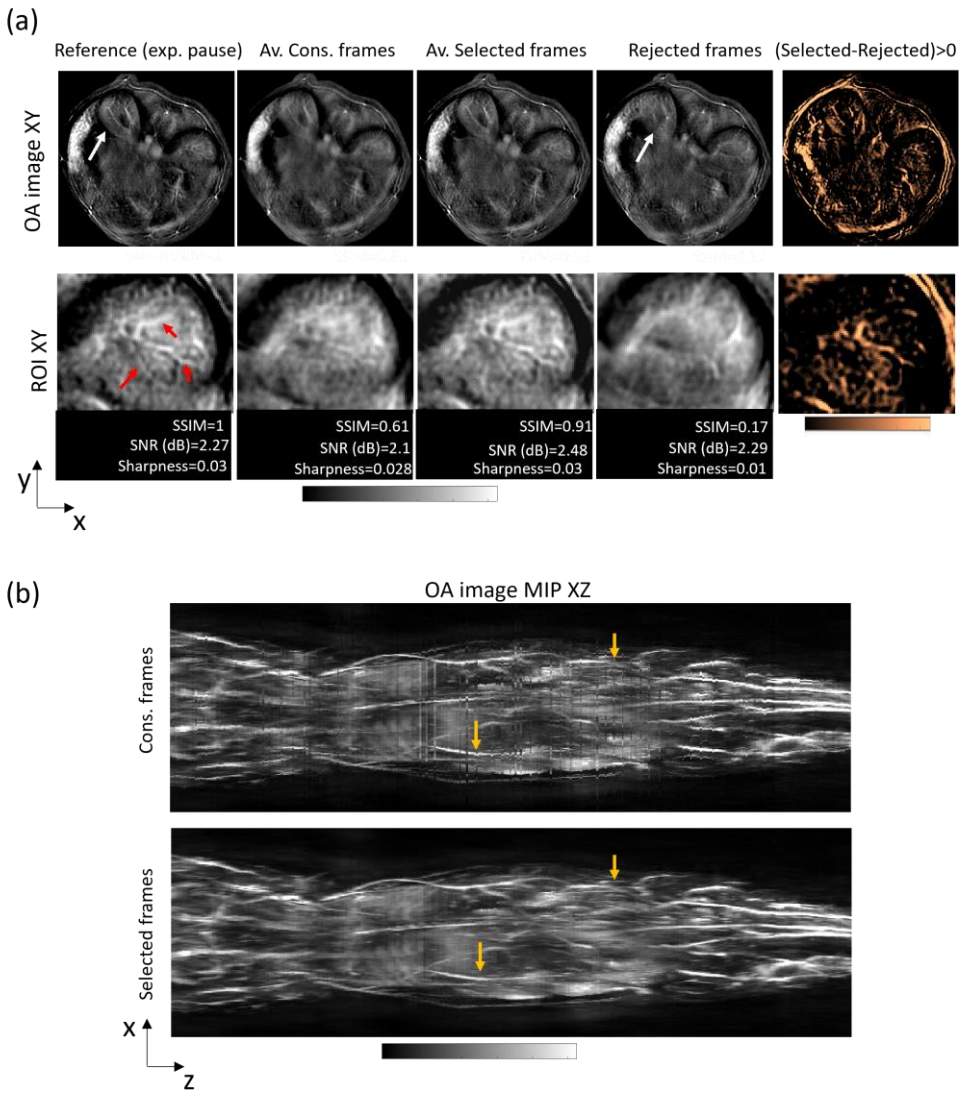

Figure 4.8. Validation of the proposed motion correction algorithm for image quality improvement in 2D and 3D single wavelength acquisition. (a) OA reconstructed images of a single cross-section in the mouse abdomen and magnifications of an ROI in the right kidney. The single frame image in the expiratory pause is taken as the reference and compared with the images obtained by averaging consecutive frames (Av. Cons. frames), by averaging selected frames in the expiratory pause (Av. Selected frames), and by averaging rejected frames (Rejected frames). SNR and entropy are used to quantify image quality improvement, while the SSIM index is used to quantify structural differences between images and the reference. The positive difference between the selected frames image and the rejected frames image ((Selected – Rejected)>0) is used to visualize image quality amelioration after breathing motion correction. Structural differences in small and large structures are marked with red and white arrows, respectively. (b) Sagittal maximal intensity projection (MIP) of volumetric images of the mouse before (Cons. frames) and after (Selected frames) breathing motion correction. Yellow arrows show disruption in the vessels due to chessboard artifacts and the improvement after breathing motion correction.

Breathing motion correction for OA image quantification improvement

To experimentally assess image quantification improvement due to breathing motion correction, a 2D cross-section image of the liver at different wavelengths was considered. Fig 4.9a shows the OA images at different wavelengths before and after applying the breathing motion correction algorithm.

Fig. 4.9b reports the improved OA spectrum in the two ROIs selected in Fig. 4.9a: one in the skin (ROI1) and the other in the abdomen aorta (ROI2). These ROIs more accurately resemble the spectra of melanin and HbO2 (respectively) after breathing motion correction (red curves).

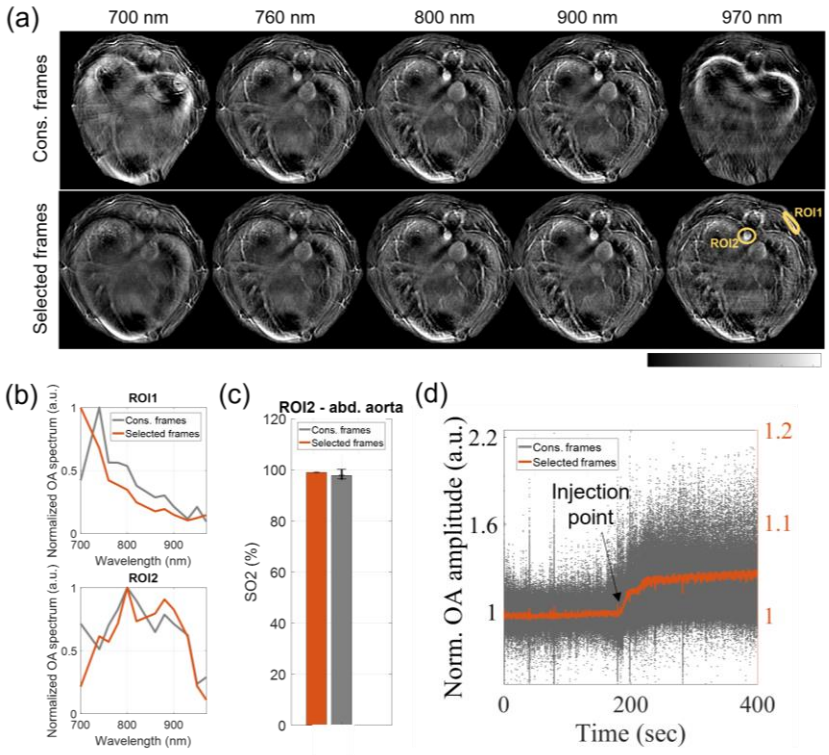

Figure 4.9. Validation of the proposed motion correction algorithm for OA image quantification improvement. (a) Multispectral OA images of the mouse liver section at different wavelengths before (Cons. frames) and after (Selected frames) implementation of the breathing motion correction algorithm. (b) OA spectra in two ROIs in the skin (ROI1) and in the abdominal aorta (ROI2), which show higher similarity to the OA spectra of melanin and HbO2 (respectively) after breathing motion correction. (c) sO2 quantification in the abdominal aorta, with reduced sO2 quantification error from 10% to 3% after breathing motion correction. (d) Normalized OA signal in the mouse abdomen across the AuNRs injection time point, showing breathing motion artifacts (grey curve) and visualization of the contrast agent perfusion after breathing correction (red curve).

Furthermore, improved sO2 quantification in the abdominal aorta (ROI1) is also reported in Fig. 4.9c. The estimated sO2 value in the abdominal aorta increases from 96% to 98%, and the mean sO2 error drops from 10% to 3% after breathing motion correction.

Finally, image quantification improvement was also demonstrated in OA applications that involve dynamic phenomena, such as when an exogenous contrast agent is injected into the mouse. Fig. 4.9d reports the normalized OA signal measured in a mouse cross-section before and after breathing motion correction during the injection of gold nanorods (AuNRs). As demonstrated, the fluctuation in the OA signal due to the physiological variations related to breathing obscures the kinetics of the exogenous contrast agent and prevents any quantification (grey curve). Instead, breathing motion correction (red curve) allows better visualization of the contrast agent perfusion and more accurate quantification of the OA signal, with an improvement in the mean OA amplitude error by 20% to 3%.

4.2.4 Discussion and Conclusions

In this section, breathing motion artifacts in living subjects has been quantified for different anatomical sections, and their effect on OA image quality and quantification has been reported for different OA applications where multiframe analysis is required.

It has been demonstrated for the first time that: 1) respiratory motion degrades image quality and resolution, and the effect is stronger in anatomical sections close to the lungs; 2) OA spectra and spectral unmixing are corrupted due to the misalignment between frames acquired at various wavelengths, where each frame corresponds to a different breathing phase; 3) OA signal quantification is affected, since the physiological variations related to breathing (i.e., concentration and oxygenation of hemoglobin) modulate the OA signal amplitude, and this is particularly crucial in applications where temporal analysis is required.

Therefore, a new automated motion correction algorithm that can be used for every acquisition schema has been proposed to improve OA image quality and quantifiability. The algorithm shows two significant advantages with respect to previous reported motion rejection approaches: motion correction is applied directly on the sinograms prior to image reconstruction, thus reducing memory requirement and complex post-processing algorithms; furthermore, the algorithm is flexible and can be applied to any acquisition schema. Indeed, compared with previous works, the suggested method has been successfully validated for different OA applications.

The new algorithm demonstrably improves image sharpness and SNR in single 2D cross-sections – as data acquired at the same respiratory phase can be constructively averaged – and removes chessboard artifacts in 3D MIP OA images generated from misalignment of consecutive frames.

Furthermore, breathing motion correction allows for better signal quantification and interpretation in OA imaging, thus enabling observation of biological processes in living mice with high fidelity and increasing sensitivity to biological mechanisms that are otherwise hindered by the natural breathing motions.

Notably, in this work, the respiratory motion is assumed to be (at least approximately) the same from cycle to cycle. This assumption is valid to a large extent, but there are certain variations in breathing motion that should be discussed and defined with relation to physiology literature.

In conclusion, the development and implementation of the breathing motion correction algorithm can benefit numerous OA imaging methods that rely on multiframe image analysis.

4.3 Disentangling the frequency content in optoacoustic imaging

Some of the text and results reported in this chapter are also presented in the following paper under review:

- *"Disentangling the frequency content in optoacoustics",* Antonia Longo, Dominik Jüstel, Vasilis Ntziachristos

I declare that the text utilized was written by myself.

4.3.1 Introduction

In contrast to ultrasonography, optoacoustic (OA) imaging systems generate acoustic signals with a rich frequency content due to ultrashort pulse illumination. Ultimately, this entire frequency content is important, since it carries information about structures on different scales (i.e., physical size). Therefore, advanced optoacoustic systems use broadband acoustic detectors to ensure that no structural information is lost. However, there are two major challenges to broadband acoustic signal detection and processing: scale dependent SNR and frequency dependent detector sensitivity.

First, as already discussed in Sec. 3.1.1, since the power of OA signals increases with illuminated volume, the contrast of small structures is obscured by the high SNR of bulk tissue. Consequently,

rendering all frequencies together biases the visual perception of the image towards larger structures by reducing the contrast of structural details. So far, standard optoacoustic image reconstruction techniques have failed to accurately render the rich multiscale information content of optoacoustics. Common filtered back-projection algorithms act as high-pass filters on the image, while delay-and-sum algorithms and model-based algorithms treat all frequencies equally, thereby penalizing the high frequencies. Both methods result in an oxymoron: achieving aesthetically pleasing images penalizes either the low or the high frequency content, leading to a lower fidelity to the biological structures being imaged.

Second, frequency dependent detector sensitivity leads to different frequency ranges being captured in "slices" of varying size, which may distort images through an increase in out-of-plane signals being detected. In addition, signals originating from structures on different scales have frequency contents that significantly overlap. The disentanglement of these overlaps is non-trivial. Therefore, disentangling the different signal components would enable multiscale contrast by separating both the contributions from different scales and out-of-plane from in-plane signals. Visualizing structures with better focus and high contrast on different scales will simplify the identification of structures of interest and therefore improve the preclinical and clinical impact of OA technologies.

Ultrabroadband OA imaging systems such as RSOM have achieved a clear separation of structures on different scales by separately reconstructing different frequency bands of signals [45]. However, due to the abovementioned signal entanglement in MSOT, enforcing band separation is not consistent with the underlying physics and results in artefacts (e.g., ring artefcats).

Separating different scales by applying 2D filters on the reconstructed images is not efficient since it is constrained to the reconstruction approach used, which up to now fails to render the full OA information content by either excluding the low frequencies (back-projection algorithms) or by penalizing the high frequency components (model-based algorithms). Furthermore, the 2D filters can enhance reconstruction artefacts emanating from limited view detection [106] or insufficient spatial sampling [37].

Separating out-of-plane from in-plane signals has been proposed by acquiring information from neighboring sections via suitable system design and scanning techniques, and by numerically

incorporating this information in 2D model based [47] or 3D back projection reconstructions [99]. These solutions to remove out-of-plane signals either oversimplify the problem (i.e., by not including transducer frequency dependent sensitivity), are impractical (i.e., require displacement of the transducer, frames alignment, etc.), or are computationally expensive. Therefore, there is a need for a method to disentangle different contributions to OA signals that is efficient in terms of computational and acquisition complexity (i.e., transducer displacement not required), consistent in terms of both the underlying physics and structural integrity, and flexible enough to address different problems within the same framework, such as numerical focusing (separating in-plane and out-of-plane signal) or multiscale representation (separating different feature scales).

Therefore, a method to decompose OA signal components that is (1) able to disentangle overlaps, (2) consistent with the underlying physical principles, and (3) guarantees structural integrity of the image components would be of great interest to the OA community.

In this work, we propose a frequency-band separated model-based (fbMB) reconstruction framework for OA tomography that untangles the overlapping frequency content of image components to improve resolution and overall image fidelity. The proposed method enables a unique frequency and scale contrast for OA imaging by: 1) imposing soft priors on the frequency content of the signals underlying the different image components, allowing the use of frequencies from other bands, if physics and structural integrity require it (disentanglement). Noteworthy, the effect of the soft priors is consistent with the underlying physics of OA, i.e., the frequency content of the OA signals from structures of different scales overlap; 2) reconstructing multiple images with the same model, such that these images sum up to a reconstruction of the full OA signal data (physics-compatible decomposition); 3) imposing non-negativity constraints on all reconstructed image components to ensure that artefacts in one component cannot be compensated by negative contributions in other components (structural integrity). The fbMB method is flexible because it is robust with respect to the choice of the filters used in the soft priors and can be used with any given linear model. Notably, the computational complexity increases only by a constant factor (linear in the number of components).

We demonstrate on both a synthetic phantom and real OA data that, with a suitable choice of filters, the new method can efficiently separate structures of different scales, as well as out-of-

plane from in-plane signals. Using 533 in vivo MSOT images of different anatomical sections of mice, we show that the new method generates OA images with lower reconstruction residuals and higher structural similarity index values compared with simple filter techniques, and improved image contrast and resolution compared with standard model-based algorithm.

We demonstrate that the method implements a unique multifrequency contrast in OA tomography, which combined with volumetric imaging, real-time acquisition, and multispectral contrast, enables the full range of optoacoustic mechanism contrast, thus providing superior imaging performance among the current biomedical imaging modalities.

By rendering the rich OA information content from the biological structures being imaged with high accuracy, fbMB could expand the applications of MSOT in both preclinical and clinical medicine.

4.3.2 Methods

Frequency-band separated model-based reconstruction

The new proposed fbMB framework allows decomposition of the OA signal in different components and reconstruction of multiple non-negative images with scale-specific contrast. Soft priors on the frequency content of signals generated on different scales steer the acoustic spectrum towards higher or lower frequencies, while allowing overlaps when required by the system model. Thus, for multiscale reconstruction, the matrix equation in Eq. 2.28 is modified as follows:

$$p = M(x_1 + \cdots + x_n), \tag{4.4}$$

where p is the broadband pressure signal recorded; and $x_1^*, \ldots, x_n^*$ are the unknown distributions of optical absorption at n scales.

Soft priors on frequency bands

In the framework of L^2 regularization, *a priori* information about the tissue being imaged can be included [123] to ensure convergence of the reconstruction algorithm to the correct optical absorption distribution on different scales. For this reason, soft priors on the frequency band separation are added into the inversion. The priors are considered “soft” because they do not force

a rigid frequency band separation, instead they allow overlap between frequency bands to preserve the physical accuracy of the solution.

The regularized inversion problem with soft priors can be written as:

$$(x_1^*, \dots, x_n^*) = \underset{(x_1,\dots,x_n)\geq 0}{\arg\min} \|p - M(x_1 + \cdots + x_n)\|_2^2$$

$$+ \lambda \|L(x_1 + x_2 + \dots + x_n)\|_2^2$$

$$+ \eta\mu_1 \|(id - F_1)Mx_1\|_2^2 + \cdots + \eta\mu_n \|(id - F_n)Mx_n\|_2^2, \tag{4.5}$$

where $F_1, \dots, F_n$ are the n bandpass filters, and $\eta, \mu_1, \dots, \mu_n$ the regularization parameters for the soft priors such that $\mu_1 + \cdots + \mu_n = 1$.

The regularized problem in Eq. 4.5 can be formulated in the same form as Eq. 2.32:

$$(x_1^*, \dots, x_n^*) = \underset{(x_1,\dots,x_n)\geq 0}{\arg\min} f(x_1, \dots, x_n) = \underset{x\geq 0}{\arg\min} \left\| \tilde{p} - \tilde{M}(x_1 + \cdots + x_n) \right\|_2^2 \tag{4.6}$$

with

$$\tilde{p} = \begin{pmatrix} p \\ 0 \\ \vdots \\ 0 \end{pmatrix} \tag{4.7}$$

and

$$\tilde{M} = \begin{pmatrix} M & \dots & \dots & M \\ \eta\mu_1(id - F_1)M & 0 & \dots & 0 \\ \vdots & \ddots & \ddots & \vdots \\ 0 & \dots & 0 & \eta\mu_n(id - F_n)M \\ \lambda L & \lambda L & \lambda L & \lambda L \end{pmatrix} \tag{4.8}$$

The Projected Conjugate Gradient [65] is used as a non-negative least square (NNLS) method to solve Eq. 4.5. Numerical inversions are usually computationally demanding, and imposing the additional an non-negative constraint increases the inversion time. However, the computational

complexity of fbMB is increased only by a constant factor (linear in the number of components) compared to standard model-based reconstruction, since the model must be evaluated once for every component x_j, and the filters must be applied.

Filters selection for the soft priors

Standard Butterworth bandpass filters are used as soft priors $F_1, \dots, F_n$ in Eq. 4.5. The low- and high-pass cutoff frequencies and the relative bandwidth are chosen to avoid ringing artifacts [45] such that:

$$\frac{BW_1}{f_{c1}} = \frac{BW_2}{f_{c2}} = \frac{BW_3}{f_{c3}} = \cdots \tag{4.9}$$

For two-scale decomposition, bandpass filters with frequency bands 0.1 - 1.23 MHz and 1.23 – 13.3 MHz are chosen in the soft priors, with 175% relative bandwidth. For three-scale decomposition, bandpass filters with frequency bands 100 - 500 kHz, 500 kHz - 1.23 MHz, and 1.23MHz-13.3MHz are selected, with a relative bandwidth of 136%.

Notably, the fbMB method is flexible because it is robust with respect to the choice of the filters used in the soft priors.

Experiments

OA measurements were conducted using a commercially available, real-time, MSOT small animal scanner (inVision 256-TF, iThera Medical, Munich, Germany).

OA images of an excised kidney from a nude mouse (4 weeks old) were acquired to demonstrate the enhancement of structures in an organ with well-defined features of varying scales through the new proposed algorithm fbMB. Ten minutes after animal euthanasia, the kidney was excised and embedded in a supporting turbid agar gel in a cylindrical mold (12 mm in diameter and 2.5 cm in height). The agar gel was made by mixing 1.6% w/m agar gel (Agar for microbiology, Fluka analytical) with 0.8% v/v Intralipid 20% (Sigma).

The multiscale capabilities of the new algorithm were tested with an *in vivo* mouse dataset, including 533 OA images from different anatomical sections, from the brain to the lower abdomen.

2D OA images were continuously acquired at single wavelength (800 nm) for anatomy visualization, or at multiple wavelengths (690 - 980 nm) for spectral unmixing quantification.

For 3D whole-body imaging, 2D images of consecutive anatomical sections were collected with 200 μm resolution between adjacent frames and then stacked together for volumetric imaging. Animal procedures were approved by the Government of Upper Bavaria. Nude mice (3 - 4 weeks old) were anesthetized and placed lying prone in the animal holder such that the transducer array faced the ventral side. After data acquisition, the mice were euthanized by cervical dislocation.

Signal pre-processing

For standard model-based reconstruction, the acquired OA signals are filtered prior to reconstruction by applying a Butterworth bandpass filter in the frequency range between 0.1 and 13.3 MHz to reject noise beyond the sensitivity of the transducers.

For simple filtering techniques, i.e., Butterworth and Wavelet, the OA signals are divided into different frequency bands by applying a bank of band pass filters and each frequency band reconstructed separately with standard model-based algorithm. For the simple Butterworth filtering technique, the bandpass filters are chosen in agreement with that selected in the soft priors. For the simple Wavelet filtering technique, the Matlab functions *swt* and *iswt* are used for two- and three-scale decomposition. The Daubechies mother wavelet with two vanishing moments 'db2' was selected, as already reported in [157]. The advantage of using Wavelet decomposition over standard filters is that it does not require the *a priori* knowledge of the frequency information contained in the signal and guarantees optimal temporal and frequency resolution for each band.

Quantification metrics

The efficiency of fbMB to separate different OA components was quantified against standard filtering techniques (i.e., Butterworth or Wavelet bandpass filters) in terms of physical and structural accuracy. For physical accuracy, we refer to the capability of the algorithm to reconstruct OA images at different scales, with the sum thereof explaining the acquired OA signals. For structural accuracy, we indicate the capability of the algorithm to compensate for potential ripples and artifacts generated by the frequency band separations.

Herein, we use the normalized reconstruction residuals as physical accuracy indicators. They are obtained by dividing the reconstruction residuals of both fbMB and standard filtering techniques for those obtained with standard model-based reconstruction.

Moreover, we use the structural similarity index (SSIM) [158] between the reference images (reconstructed with a standard model-based reconstruction) and the images obtained with the two different methods, i.e., fbMB and standard filtering techniques (sum of all components) to evaluate the structural accuracy.

To quantify image quality improvement of fbMB against standard model-based reconstruction, two different metrics are proposed: image entropy, as an objective indicator of the image information content; and perception-based image quality evaluator (PIQE) to account for human visual system perception [159]. The two indices were estimated on the three-channel RGB images.

To adjust image contrast, a histogram-based thresholding method was applied to all OA images by removing 0.5 % highest and 0.02% lowest pixel values. Note that the process was applied only to improve image visualization, and all quantification metrics were estimated on the raw images.

Regularization parameters

The Tickhonov regularization parameter λ was selected based on the L-curve and the reconstruction residuals curve. For standard model-based reconstruction, the L-curve is the plot between the penalty term $\|x\|_2$ against the norm of the residual $\|p - Mx\|_2$. The residuals curve is the plot of the normalized reconstruction residual errors for different values of the parameter λ. Fig. 4.10a, b show an example of the L-curve and residuals curve from standard model-based reconstruction of an *in vivo* OA image of mouse kidneys section. Usually, the optimal trade-off for λ is achieved close to the corner of the L-shaped curve. For this reason, a value of λ equal to 0.005 was selected, which also provides a good reconstruction residual error before it increases. Fig. 4.10c, d report the OA reconstructed images with standard model-based reconstruction and corresponding OA signal spectra for different values of λ. Notably, low values of λ lead to noisy OA images, while high values increase the reconstruction error by removing useful information from the low frequencies.

The regularization parameters $\eta, \mu_1, \ldots, \mu_n$ for the soft priors were instead chosen directly on the reconstruction residuals curve. First, the value of η was chosen by fixing the values of μ_i to be equal and by selecting the value of η in correspondence of which the residuals curve has a corner (red dot in Fig 4.10e). Then, the values of $\mu_1, \ldots, \mu_n$ were selected according to the configuration that gives the lowest reconstruction error, as shown in Fig. 4.10f (red dot). Based on this, a value of 10 was selected for the parameter η, while the values of 0.9 and 0.1 were selected for μ_1, μ_2 for the case of two-bands decomposition. The effect of different soft prior regularizers on OA images and spectra for two-bands decomposition is reported in Fig. 4.10g and Fig. 4.10h. As demonstrated, the selected parameters allow generation of OA images with scale-specific contrast and low reconstruction residuals.

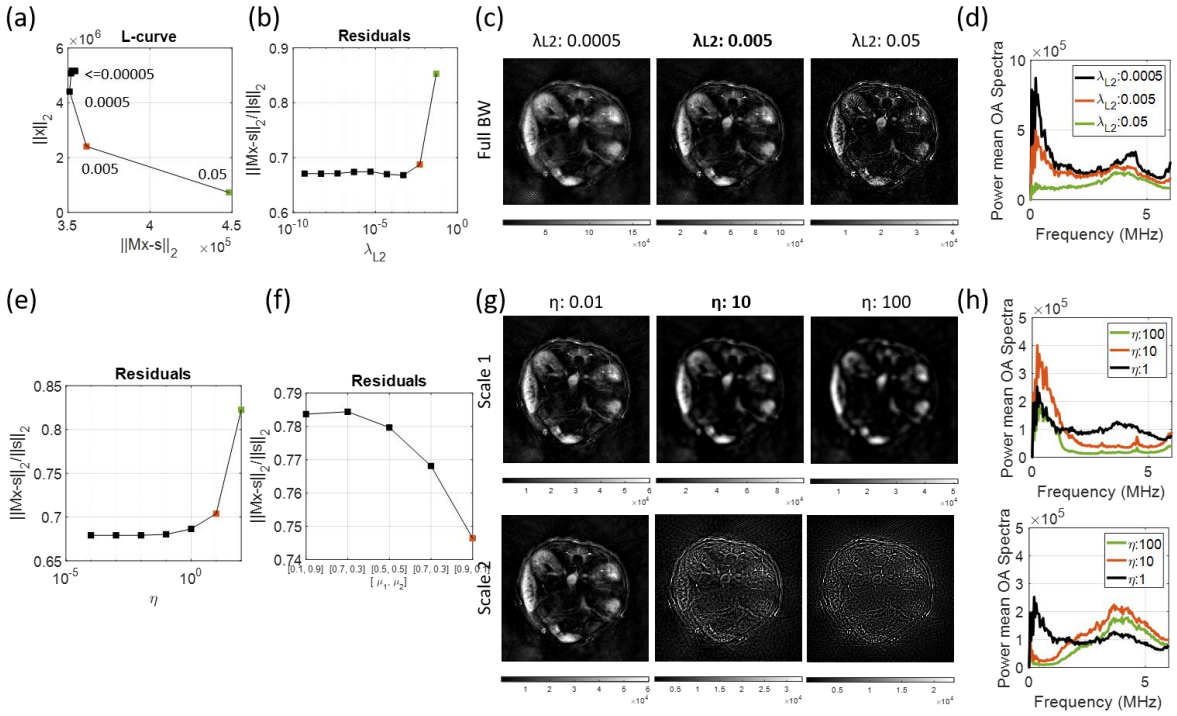

Figure 4.10. Effect of different regularization parameters and tuning in *in vivo* OA images. (a) L-curve for the Tickhonov regularization parameter λ for standard model-based reconstruction. (b) Reconstruction residual errors of standard model-based reconstruction for different values of λ. (c) *In vivo* OA images reconstructed with standard model-based reconstruction with different λ and (d) relative OA signal spectra. (e) and (f) reconstruction residuals for 2bMB for different values of soft prior regularizers η and $[\mu_1, \mu_2]$. (d) OA reconstructed images for two bands decomposition with different values of η and h) relative OA spectra.

4.3.3 Results

The proposed fbMB method separates OA signal contributions from different frequency bands by integrating the filtering process with soft priors into the model and by applying non-negativity constraints on all components. In the resulting multiscale images, anatomical structures of all sizes are more accurately represented in the preclinical setting. Fig. 4.11 reports a schematic of two-band model-based reconstruction (2bMB). The 2bMB reconstruction is applied to the OA signal acquired by the system and generates OA images of specific frequency band components: a low frequency image (Band 1, Image domain in Fig. 4.11) containing mainly signals from larger structures and a high frequency image (Band 2, Image domain in Fig. 4.11) corresponding to smaller structures. OA images with multiscale contrast are generated by color-coding and blending the different components (2bMB, Image domain in Fig. 4.11). Notably, the soft priors on the frequency content of the components allow each component to include frequencies from other bands if the model requires it (2bMB, Signal domain in Fig. 4.11).

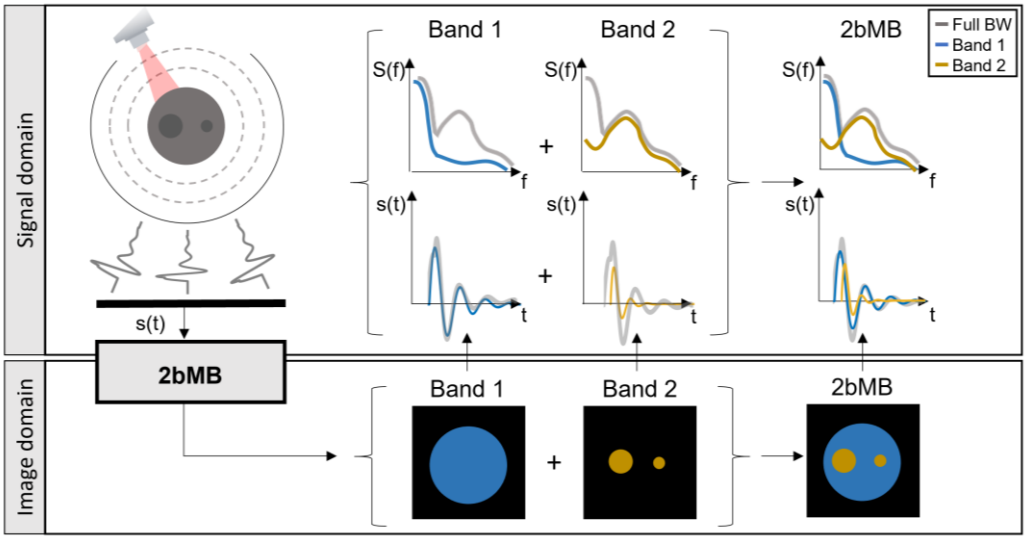

Figure 4.11. Schematic of two-band model-based reconstruction (2bMB).

In the following, we report our findings in phantoms, and in ex vivo and in vivo mouse data and support them with different figures of merit, such as the reconstruction residuals, the structural

similarity index measure (SSIM), the image entropy and the Perception-based Image Quality Evaluator (PIQE).

Section 4.3.3.1 details the effectiveness of the proposed method to separate different frequency band components in OA imaging. Sections 4.3.3.2 and 4.3.3.3 describe the validation of the method against standard signal filtering and simple model-based reconstruction. Section 4.3.3.4 reports spectral unmixing results to demonstrate multiscale quantification of specific chromophores.

4.3.3.1 Disentanglement of frequency content by fbMB

The capability of the algorithm to generate images with band-specific contrast is first demonstrated on a controlled synthetic phantom with well-defined features of different sizes (Fig. 4.12a). The phantom features a network of vessel-like structures with diameters ranging from 1.3 mm to 240 μm, which are embedded in a circular absorbing background that is 1.7 cm in diameter and absorbs 10 times less than the vessel-like structures (see Methods section). We tested two-band decomposition by applying a two-band model-based (2bMB) algorithm. For 2bMB, two band-pass filters with frequency bands 0.1-1.23 MHz and 1.23-15 MHz were chosen for the soft priors, with 175% relative bandwidth (see Methods section).

Fig. 4.12b shows images of the phantom that were reconstructed by the two-band model-based (2bMB) algorithm. The new algorithm successfully decomposes images into components on different physical scales. Low frequency images (Fig. 4.12b, Band 1) contain mainly signals from larger structures ranging from 1.6 cm to 600 μm in diameter, while high frequency images (Fig. 4.12b, Band 2) correspond to small structures that are less than 600 μm across. Color-coding and blending the frequency band components generates OA images with multiscale contrast (Fig. 4.12b, 2bMB). Compared with standard model-based reconstruction (MB in Fig. 4.12c), 2bMB affords a more accurate image and improved visualization of small features (red arrows in the ROIs). Fig. 4.12d reports the mean power spectra of the OA signals generated by the structures on different scales for the 2bMB algorithm, which demonstrate that the frequency contents of the different reconstructed components overlap significantly. This finding confirms that the new method achieves a more realistic disentanglement of different-sized structures compared with simple frequency filtering, which cannot model such overlapping frequency content. The

separation of this overlapping content is enabled by the soft priors on the filtering process in the reconstruction, which allows the components to integrate frequencies from other bands if the model requires it (see Methods section).

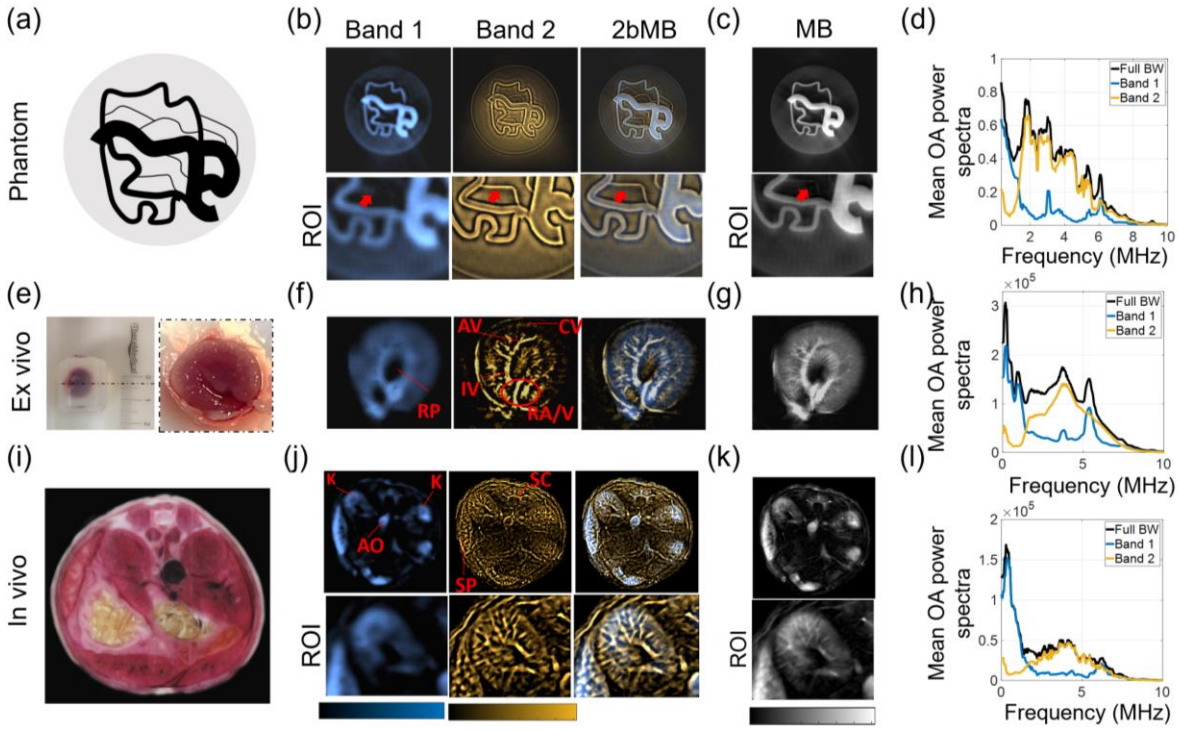

Figure 4.12. Frequency content disentanglement in OA imaging and frequency-band model based (fbMB) reconstruction. (a) A synthetic phantom with well-defined features of varying size. Reconstructed OA images of the phantom for (b) two-band model-based and (c) standard model-based reconstruction (MB). The 2bMB image was obtained by color-coding and blending the different frequency band components. The red arrows in the magnified ROIs indicate a small structure enhanced with the new method. (d) Mean power spectra of the OA signals corresponding to the two different frequency band components of the phantom showing frequency overlaps between the components due to soft priors in the reconstruction. (e) Ex vivo mouse kidney embedded in agar and magnification of the selected anatomical cross section in the middle segment. OA images of the kidney cross section reconstructed using (f) two-band model-based and (g) standard model-based reconstruction. (h) Mean power spectra of the OA signals corresponding to the two frequency band components. Visible anatomical details in the vascular network of the excised kidney for 2bMB: Main renal vessel (RA/V), interlobal (IV), arcuate (AV) and cortical (CV) vessels. j) Anatomical image of a mouse kidneys section including spleen and liver lobes. In vivo OA images of the mouse kidney section reconstructed by using (j) two-band model-based and (k) standard model- based reconstruction. Kidney (K), aorta (AO), spleen (SP) and spinal cord (SC). OA frequency content for the corresponding frequency band components for (l) two-band decomposition.

Next, the algorithm was applied to OA images of an ex vivo mouse kidney (Fig. 4.12e) to demonstrate the ability of frequency band contrast to reveal structures and vessels of different sizes in tissue. Fig. 4.12f shows an OA image after decomposition into two bands. As with the phantom, the algorithm efficiently separated the different anatomical components in the kidney. Low frequency components contain primarily OA signals from the organs and large vessels. High frequency components have better in-plane focus and show small vessel networks with high accuracy. Furthermore, as shown in Fig. 4.12h the OA spectra of the different bands overlap in the frequency domain, again confirming the effect of the soft priors on the reconstructed images, which enable each component to integrate frequencies from other bands to assure structural and consistency with the underlying physics. Blending the two bands (2bMB in Fig. 4.12f) afforded OA images in which fine details, such as small vasculature inside bulk tissue, were rendered with significantly higher contrast than possible with standard reconstruction (Fig. 4.12g).

The frequency disentanglement approach was then applied to reconstruct an image of a kidney section in a live mouse (Fig. 4.12i) to demonstrate image quality improvement and structural enhancement in vivo. Fig. 4.12j shows the different frequency band components of the mouse kidney section, obtained by applying 2bMB. The low-frequency bands contain signals from organs, such as the kidneys (K) and spleen (SP), or large structures, such as the abdominal aorta (AO), and the spinal cord (SC). The high-frequency components contain signals from small vessels, such as the microvasculature in the kidney, the splenic vessel (SPV), and the hepatic vessels (HEV). As expected, the OA signals from these structures again overlap in the frequency domain (Fig. 4.12l), supporting the physical fidelity of the reconstructed in vivo images. Finally, the OA images obtained by blending the different frequency band components (2bMB in Fig. 4.12j) visualize with high contrast the entire OA information content, which is not possible with the standard model-based reconstruction (MB in Fig. 4.12k).

Finally, we tested three-band model-based (3bMB) reconstruction in order to evaluate the effect of a finer frequency band decomposition on the image contrast. For 3bMB, three bandpass filters with frequency bands 100-500kHz, 500kHz-1.23MHz and 1.23MHz-13.3MHz were selected for the soft priors, with a relative bandwidth of 136% (see Methods). Similar to 2bMB, 3bMB successfully separates the different OA frequency band components in the images. Low frequency

images contain signal from bulky absorbing tissue and large structures, while the high frequency images contain signals from smaller structures (Fig. 4.13a,c,e). Furthermore, as shown in Fig. 4.13b,d,f, the individual bands overlap consistently in the frequency domain due to the soft priors in the reconstruction.

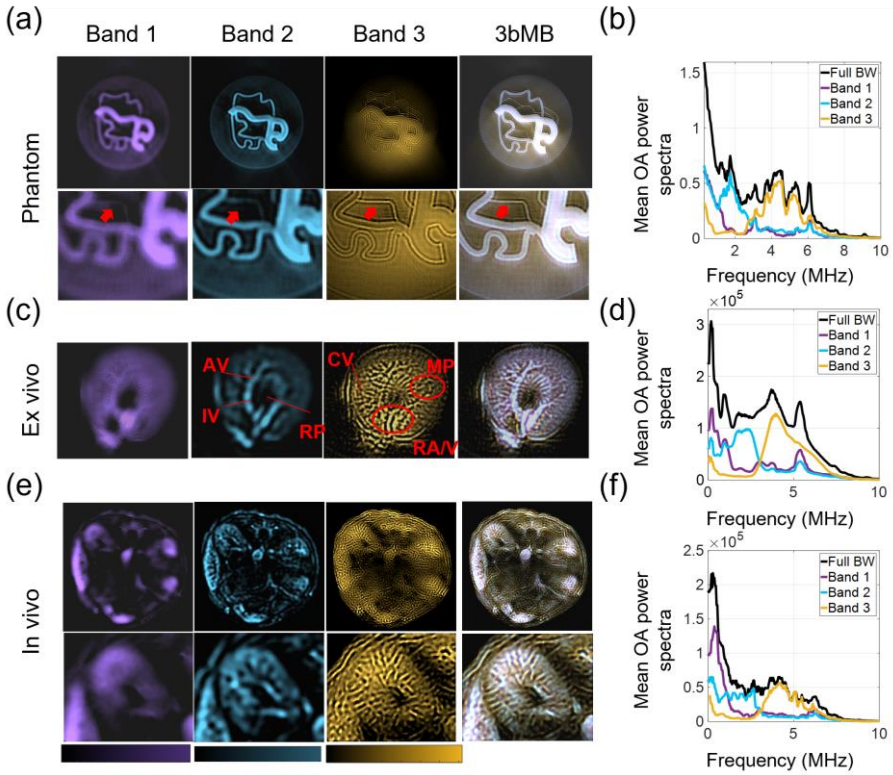

Figure 4.13. 3bMB reconstruction. a) Three-band decomposition of OA images of the synthetic phantom from Fig. 1b. The 3bMB images were obtained by color-coding and blending the three components. The red arrows in the magnified ROIs indicate a small structure enhanced with the new method. b) Mean power spectra of the OA signals of the phantom for three different frequency band components with frequency overlaps between the components due to soft priors in the reconstruction. c) 3bMB reconstructions of the excised kidney cross section shown in Fig. 1f. d) Mean power spectra of the OA signals corresponding to the three frequency band components. Visible anatomical details in the vasculature network of the kidney for 3bMB: Main renal vessel (RA/V), interlobal (IV), arcuate (AV) and cortical (CV) vessels. Renal cortex (RC), medullary pyramids (MP). e) In vivo 3bMB reconstructions of the mouse kidney section of Fig. 1j. f) OA frequency content of the three frequency band components.

By increasing the number of bands from two to three, we observed that the high frequency structures are further decoupled from the middle and low frequencies, thus demonstrating that by

finer decomposition of the signal, the image resolution further increases, and the visual perception of small structures improves. For example, the three-band reconstruction of the exvivo kidney section in 3bMB in Fig. 4.13c reveals further anatomical details of the vascular network of the kidney with high accuracy. A notable example is the main renal vessel (RA/V) entering the kidney and progressively branching into the interlobal (IV), arcuate (AV) and cortical (CV) vessels, which cannot be identified in the 2bMB image (2bMB in Fig. 4.12f) or the standard model-based reconstructed image (MB in Fig. 4.12g). 3bMB thus allows detailed visualization of the entire blood supply in the kidney.

4.3.3.2 Comparison of 2bMB against simple filtering techniques

Compared to standard filtering methods, the proposed algorithm achieves a significantly higher physical and structural integrity in the following sense. First, if an image is decomposed into a superposition of images on different scales, each component should comply with the underlying physics. We can quantify this property by comparing the residual errors of the signals that are generated by applying the system model to the sum of the components. Second, the superposition of the different scales should produce the same image as if we reconstructed just one image from the data. In particular, separating different scales should not introduce artefacts (e.g., ripples at edges). A metric for this kind of structural integrity is the structural similarity index compared to the standard model-based reconstruction. We validated the physical and structural integrity of the 2bMB reconstruction against standard signal filtering with Butterworth filters and Wavelet filters (Fig. 4.14) on a dataset of 533 OA images from different anatomical sections.

Fig. 4.14a displays exemplary multiscale OA images from a mouse liver section obtained with 2bMB reconstruction and with model-based reconstruction after the application of Butterworth and Wavelet bandpass filters. As shown in the images, all three methods separate the different frequency bands of OA contrast in the liver section, highlighting bulky tissue (Band 1) or vasculature (Band 2). However, as shown in Fig. 4.14b, 2bMB generates OA images with lower reconstruction residuals (mean value of 1.3) compared to Wavelet (mean values of 4.7) and Butterworth (mean value of 6.8). Therefore, the new proposed decomposition approach has only a small regularizing effect when compared to standard model-based reconstruction. Hence, the

new method assures a solution with the highest physical accuracy, i.e., the sum of the different OA components best explains the original OA signals.

In addition, as shown in Fig. 4.14c, the new algorithm generates images with the highest structural similarity index measure SSIM of 0.6 when compared with the reference reconstruction, while the filtering techniques achieve values of 0.39 (Wavelet) and 0.21 (Butterworth), respectively. Therefore, integrating the filtering process with soft priors into the inversion assures that no artefacts are generated by the decomposition and that the integrity of the structure being imaged is better preserved. The still low value of structural similarity of 0.6 for the 2bMB reconstruction is due to the regularizing effect of the frequency band decomposition.

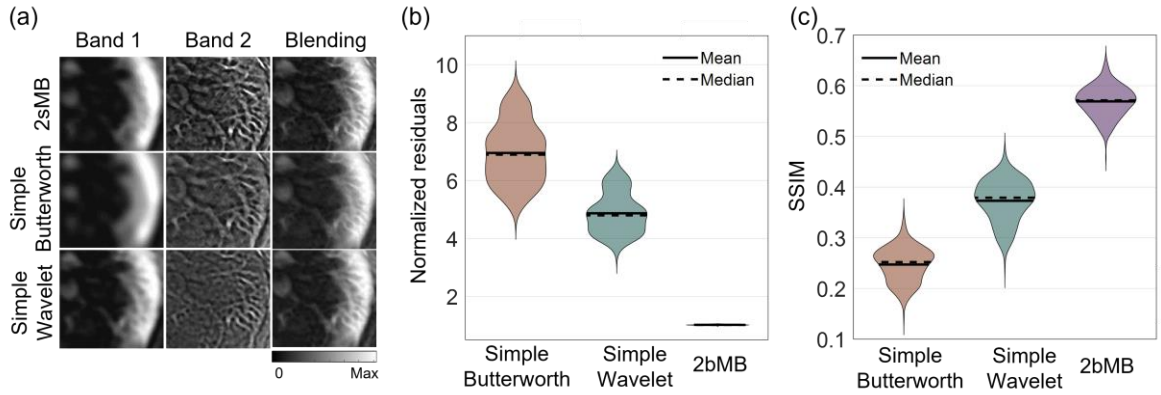

Figure 4.14. Comparison of 2bMB against simple filtering techniques. (a) Two-band decomposition of an in vivo OA image from a mouse liver section using 2bMB (top), simple Butterworth (middle), and SWT (bottom) filtering techniques. (b) Reconstruction residuals and (c) structural similarity index measure (SSIM) of 2bMB and simple filtering techniques, compared to standard model-based reconstruction

4.3.3.3 Comparison of 2bMB against standard model-based reconstruction

Fig. 4.15 demonstrates the effectiveness of 2bMB to separate anatomical structures on different scales in in vivo whole-body images of a mouse. The improved contrast of 2bMB image (obtained by color-coding and blending images at different scales) was quantified against a standard model based reconstructed image (MB) using two figures of merit: the image entropy and the Perception-based Image Quality Evaluator (PIQE).

Fig. 4.15a shows the maximum intensity projection (MIP) images of the mouse in the YZ and XZ planes for two-scales decomposition (Band 1 and Band 2) reconstructed with 2bMB algorithm. As expected, the low scale image contains OA signals from large anatomical structures, such as organs, muscles, and large vessels, while the high scale image shows the vasculature network inside of the mouse. Several anatomical structures can be identified in the low-frequency band image (blue), including the carotid artery and the jugular vein in the mouse neck, the aorta and the vena cava running parallel in the mouse abdomen and branching into the iliac artery/vein in the lower abdomen, the trapezius muscle in the upper part of the spine, the femoral muscle in the lower extremities of the mouse, the kidneys, and the liver lobes in the abdomen. Visible in the high-frequency band image (yellow) are the dorsal intercostal veins and arteries between the ribs, which provide blood supply in the thoracic wall, and the superficial epigastric artery and vein, both cranial and inferior. Fig. 4.15b shows the image quality improvement of 2bMB in both 3D and 2D mouse sections, compared to standard model-based reconstruction (MB). Clearly, the 2bMB images, obtained by color-coding and blending the different scales (Fig. 4.15a), show much clearer anatomical details and broadband OA contrast. In contrast, OA images reconstructed with standard MB reconstruction appear blurred and lack contrast for small structures. For example, the dorsal artery and vein are clearly visible in the 2bMB image but hidden in the MB images due to the proximity of liver and lungs. Fig. 4.15c,d report the values of entropy and PIQE estimated for 533 in vivo OA images from different mouse anatomical sections, which quantify the image quality improvement of 2bMB compared to standard MB reconstruction in a large dataset. The OA images reconstructed with the proposed method exhibit increases in entropy of 50%, demonstrating a better visual contrast, and a reduction in the PIQE index of 19%, implying an overall improved visual image quality.

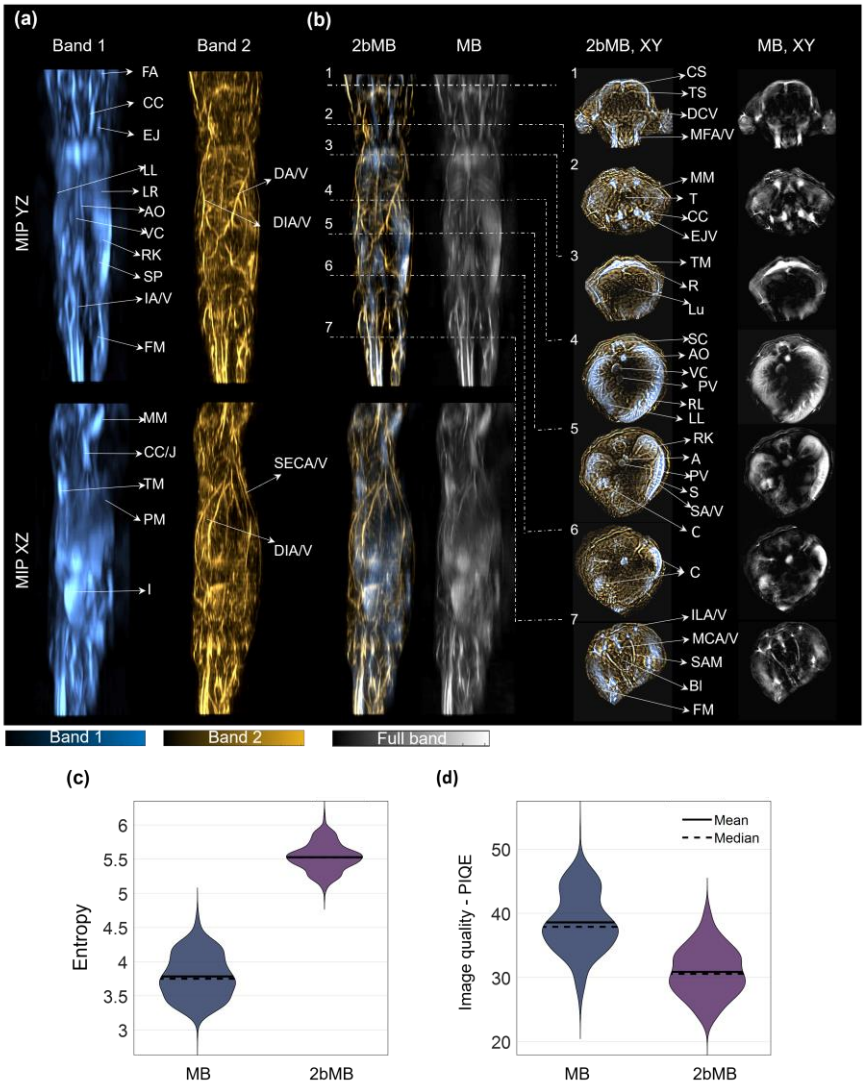

Figure 4.15. Comparison of 2bMB against standard model-based reconstruction. (a) MIP images of volumetric OA mouse data in the YZ and XZ planes for the two frequency band components obtained with 2bMB reconstruction. (b) Comparisons of 2bMB reconstructions to standard model-based (MB) reconstructions for both volumetric data (left) and 2D sections (right) of the mouse. Image quality indicators (c) entropy and (d) PIQE. 1 brain section; 2 neck section; 3 lungs section; 4 liver section; 5 kidneys section; 6 colon section; 7 lower abdomen. Facial artery (FA); Common carotid (CC); External jugular (EJ); Liver left (LL); Liver right (LR); Aorta (AO); Vena cava (VC); Right kidney (RK); Spleen (SP); Iliac artery and vein (IA/V); Femoris muscle (FM); Masseter muscle (MM); Common carotid/ jugular (CC/J); Trapezius muscle (TM); Pectoral muscle (PM); Intestine I; Dorsal artery and vein (DA/V) Dorsal intercostal artery and vein (DIA/V); Superficial epigastric cranial artery and vein (SECA/V); Confluence sinus (CS); Transverse sinus (TS); Deep cerebral vessel (DCV); Mandibula-facial arteries and veins (MFA/V); Trachea (T); Rib (R); Lungs (Lu); Spinal cord (SC); Splenic artery and vein (SA/V); Colon (C); Middle caudal artery and vein (MCA/V); Straight abdominal muscle (SAM); Bladder (Bl).

4.3.3.4 Spectral unmixing

2bMB also improves image quantification via spectral unmixing in OA imaging by utilizing the regularization effect of the decomposition to prevent negative values of big scales from compromising the signal quantification in small vasculature. Fig. 4.6a displays the absorption spectra of oxygenated hemoglobin (HbO2) and deoxygenated hemoglobin (Hb) in the range 800 – 980 nm. Fig. 4.6b shows the Hb and HbO2 spectral linear unmixing results for mouse cross sections of liver and kidneys, obtained from both 2bMB and standard MB reconstruction. Notably, the proposed method enables Hb and HbO2 quantification in small vessels, which are otherwise obscured by low frequency signals. The magnification of a region-of-interest (ROI) in the right lobe of the liver clearly shows the small vasculature that supply blood to the liver; the magnification of an ROI in the left kidney demonstrates Hb and HbO2 quantification in the splenic vessel, as well as in the small vasculature in the kidney cortex.

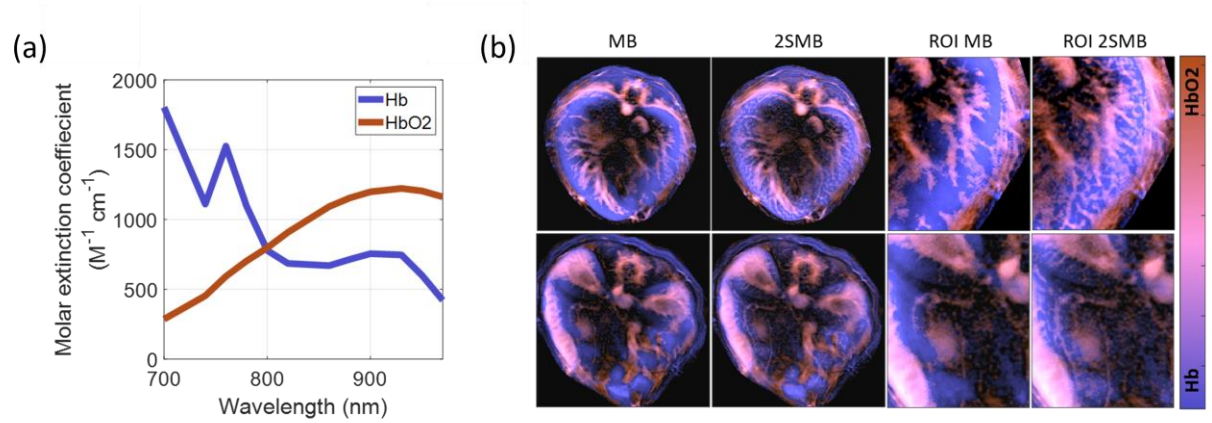

Figure 4.6. Spectral linear unmixing of in vivo mouse liver and kidneys sections. (a) Absorption spectra of oxygenated hemoglobin (HbO2) and deoxygenated hemoglobin (Hb) in the range 700 – 980 nm. (b) Spectral linear unmixing of Hb and HbO2 in mouse liver and kidneys sections obtained from OA images reconstructed with MB and 2bMB. Magnification of two ROIs in the left lobe of the liver and in the kidney-spleen region.

4.3.4 Discussion and Conclusions

OA imaging yields rich information content due to the detection of broadband acoustic signals. However, it is challenging in OA imaging to faithfully render objects in different size regimes with a single image, which compromises the accuracy subsequent physical and spectral analyses. Too

overcome this challenge, we developed fbMB, a method which employs soft priors on the frequency bands to generate OA images with scale specific contrast; low-frequency scale images contain bulk tissue, organs, and out-of-plane signals, while high-frequency scales images contain small vasculature and anatomical details. The method is a practical solution to the longstanding problem of how to efficiently separate optoacoustic absorbers at various scales and thereby counteract the bias towards low frequencies in optoacoustic imaging.

Contrary to standard back-projection and model-based reconstructions, the new algorithm allows, for the first time, access to the full structural content of broadband OA images, which is of great value for preclinical and clinical applications. In combination with the three spatial dimensions (3D), the time dimension (4D), and the optical wavelength dimension (5D), fbMB adds the sixth dimension to optoacoustic imaging which is the ultrasound frequency dimension (6D), thus enabling to analyze images over multiple scales.

The acquisition and visualization of six-dimensional OA data enables the full range of optoacoustic contrast mechanism, i.e., real time volumetric imaging at multiple wavelengths and multiple scales, offering a unique imaging performance among the current biomedical imaging modalities.

The ability of fbMB to separate different scales without generating artefacts was demonstrated on 533 *in vivo* OA images from different mouse anatomical sections. By imposing soft priors on the filters and allowing frequency bands overlap, the new method provides a unique solution to the decomposition problem, which is less prone to reconstruction errors and artefacts than rigid filtering. Moreover, fbMB generates OA images with richer informational content and better visual and structural perception compared to standard model-based reconstruction. The resulting more informative OA images allow the visualization of anatomical structures with high biological accuracy, increasing the biomedical value of OA imaging systems.

Spectral unmixing applied to fbMB reconstructions enables quantification of absorbers ranging from millimeter to micrometer resolution. Spectral unmixing algorithms are usually applied to OA images reconstructed with standard model-based algorithms due to their higher accuracy. However, a common problem for optoacoustic image quantification is that the negative values originating from larger scales or artefacts compromise the quantification of small-scale features. Here instead, the multiscale representation of the different chromophores through fbMB prevents

larger scales from interfering with smaller scales and enables label-free quantification of the vasculature down to the capillary level. This result may extend applications of optoacoustic image quantification in, for example, cardiovascular imaging by providing anatomical information from macro- to micro- vasculatures; in cancer imaging, by detecting angiogenesis and tissue perfusion; in neuroimaging, by mapping the hemodynamics in the brain vasculatures with high resolution.

The method is very flexible as it is robust with respect to the choice of the filters and allows a broad range of applications and extensions. For instance, beyond multiscale contrast and numerical focusing (i.e., separating the out-of-plane from the in-plane signal), one could include the spectral dimension into the reconstruction and, e.g., do simultaneous unmixing to enable multiscale quantification of specific chromophores in the same schema. A variation of the introduced method could also help to decouple absorption and light fluence, which exhibits a global low spatial frequency component, thus potentially improving OA signal quantification in small vasculatures and in bulk tissue.

In addition, a dedicated filter design in the soft priors could improve the current results for specialty applications. Indeed, each of these scales has biological and clinical potential, ranging from non-invasive imaging of small animals and humans at the macroscopic scale to assessing processes in organs and bulky tissues to detecting physiological mechanisms at microscopic levels (e.g. in the microvasculature).

Notably, the method is also applicable to other image reconstruction problems that are based on a linear model of physical phenomena and suffer from the same bias towards low frequencies, such as confocal microscopy (optical aberration), MRI (bias field), Tissue Harmonic Imaging (THI, fundamental harmonic), or in multifrequency Diffuse Optical Tomography (DOT). Furthermore, the method can be easily rescaled and extended to optoacoustic microscopy and mesoscopy.

Recently, applications of machine learning in imaging have afforded real time implementations of previously computationally expensive reconstruction methods. By learning model-based reconstruction, such an implementation of the presented fbMB method would allow real time multiscale feedback to the system user in clinical applications. This would enhance the clinical usage of MSOT for screening and diagnosis.

The proposed method enables a unique frequency/scale contrast for OA imaging encoding the entire OA content in a single image. The improved image quality and visual perception of anatomical structures will advance the translation of OA technology in clinical practice.

5 *In vivo* validation method for vasculature enhancement algorithms

5.1 Introduction

The development of novel image contrast enhancement tools is essential in preclinical and clinical OA imaging, as they play a critical role in real-time visualization of structures to support accurate diagnosis and disease treatments. Enhancement algorithms may however introduce artifacts and amplify noise; therefore, investigation of these tools in the context of accuracy is crucial.

This is especially apparent in macroscopy, where images are more susceptible to background tissue absorption and vessels suffer from reduced contrast, leading to artifacts. Several algorithms have been developed to enhance small and complex vascular structures in OA images and quantify them. However, the wide use of these tools necessitates a careful analysis of their influence on image accuracy, which can be assessed by developing validation methods and defining the ground truths.

Different validation methods have been proposed in OA imaging, which involve physical phantoms, numerical simulations, or *ex vivo* samples.

Physical phantoms, extensively used for standardization due to their well-known and controllable properties, they generally lack the complexity that characterizes *in vivo* tissues. Numerical phantoms also offer an appealing alternative for validation; however, these models are very simple due to the neglected physical phenomena and hardly match with the physical measurements. Furthermore, validation methods involving imaging of *ex vivo* samples require tissue sectioning, which leads to changes in the tissue optical properties, thus making it difficult to generalize the conclusions to *in vivo* clinical data.

Therefore, there is a need on the development of *in vivo* validation methods in OA. Indeed, the development of these methods is important as OA imaging begins to establish in the clinics.

Defining *in vivo* validation methods is a challenging task due to the high inter-experimental variability and due to their highly application-specific nature in clinical contexts.

The aim of this work is to define a standardized method for the *in vivo* validation of vasculature enhancement algorithms in OA imaging. First, we describe a new method that provides the ground truth for vessel detection in *in vivo* mice by using AuNRs as an exogenous contrast agent to label vessels. After, we provide a validation metric – the SSIM – to assess the biological accuracy of the vasculature enhancement tools in comparison with the ground truth. Several challenges inherent to the *in vivo* validation in OA are also addressed in this chapter, which include selection and characterization of AuNRs, fluence problems, *in vivo* imaging protocol, breathing motion, and further image post-processing for the ground truth extraction.

The proposed *in vivo* validation method will enable assessment of the performance and limitations of vasculature enhancement algorithms in OA and will supporting their validity and applicability in clinical practice. The Application section reports an example in which the proposed validation method was used to assess the accuracy of a vasculature enhancement filter widely used in OA.

5.2 Gold nanorods as exogenous contrast agent for vasculature enhancement in *in vivo* OA imaging

The main advantage of using exogenous contrast agents in OA imaging, particularly in macroscopy, is that they increase the detection sensitivity by minimizing the influence of the signal from endogenous chromophores [160, 161]. Furthermore, depending on their shape and size, exogenous contrast agents can bond with specific molecules or selectively propagate or accumulate in certain organs or structures of interest inside the body

Among all OA contrast agents, gold nanoparticles (AuNPs) have been widely used for the selective enhancement of vasculatures in OA imaging, enabling users to image small vessels in *in vivo* OA imaging with greater clarity and detail [162]. When the AuNPs are illuminated with a light source, the electric field causes the oscillation of the conduction-band electrons at the surface of the particle, which is the so-called surface plasmon resonance (SPR) effect. The electromagnetic field can enhance both the radiative and nonradiative properties of the AuNPs. Indeed, plasmons can either decay nonradiatively or radiatively, resulting in absorption or light scattering, respectively. By changing the size, shape, and internal structure of the AuNPs, the relative magnitude of light

being absorbed and scattered can be tuned, and optical absorbing-dominant AuNPs are more valuable for OA imaging.

Due to their strong and facile tunable optical absorption in the NIR region, AuNRs find large application in MSOT imaging. Their cylindrical conformation (Fig. 5.1a) allows the free electrons around the nanorods to oscillate along both the long and short axis in the presence of an electromagnetic field. The oscillation of the long axes (also called longitudinal bond, L-SPR) contributes to the specific absorbance wavelengths in the NIR, which is of interest in MSOT imaging. The oscillation of the short axis (also called transversal absorption band, T-LSR) is constant at around 520 nm. AuNRs with aspect ratios between 3 and 4 have been found to be optimal, as the absorption predominates over scattering and the specific absorbance peaks fall into the NIR optical window.

Compared to standard NIR-absorbing dyes, AuNRs offer several advantages: they show grater absorbance (orders of magnitude higher), they are not susceptible to photobleaching, and they cannot easily extravasate from the circulatory system due to a larger physical size. However due to the poor tissue penetration and clearance, these particles often accumulate in the reticuloendothelial system, thus yielding poor biocompatibility [162].

In this work, commercially available AuNRs *Ntracker D12M-10-780-50* (Nanopartz Inc., Loveland, CO) were chosen as an exogenous contrast agent for vessel enhancement in mice. These particles have an aspect ratio of 3.8 and an absorption peak at 780 nm in the NIR window. Their dimensions of 10 nm x 38 nm assure that the particles cannot be easily extravasated from the circulatory system, and therefore are optimal for vasculature enhancement. Furthermore, the particles are coated in a dense layer of hydrophilic polymers that shield the gold surface, improving OA efficiency conversion and photostability [162].

Before *in vivo* experiments, the AuNRs were characterized as follows: the absorption spectrum of AuNRs was measured either with a spectrometer (LS-1-cal, USB40000; Oceanoptics, Germany) or by MSOT system (inVision 256-TF, iThera Medical, Munich, Germany). The measurement with the spectrometer was performed at 780 nm on 1 optical density (OD) stock solution of AuNRs and 5 dilutions. The measurements with MSOT were performed on the 5 dilutions of the AuNRs. The different dilutions were inserted in a transparent plastic tube (insertion diameter: 3 mm) and

placed into a cylindrical MSOT phantom (1.3% agar, 6% intralipid μs~10 cm^{-1}) to determine the OA spectra.

Fig. 5.1b shows the normalized surface plasmon absorption spectra of AuNRs measured with a spectrophotometer (420 - 980 nm) in gray and MSOT (700 - 920 nm) in red, for 1 OD concentration of AuNRs at 890 nm. As shown, the particles have two distinct absorption peaks, at 510 nm (L-SPR) and 780 nm (T-SPR). In the NIR region between 700 - 920 nm, the MSOT spectrum resembles the spectrum from the spectrophotometer. Fig. 5.1c reports the reconstructed image of the OA phantom with the 3 mm inclusion containing AuNRs at different concentrations. Fig. 5.1d reports the linear correlation (R^2 = 0.962) between OA absorption and AuNRs concentration (related to OD) at 780 nm, demonstrating the linear dependency between OA signal intensity and AuNRs concentration, reported here as OD.

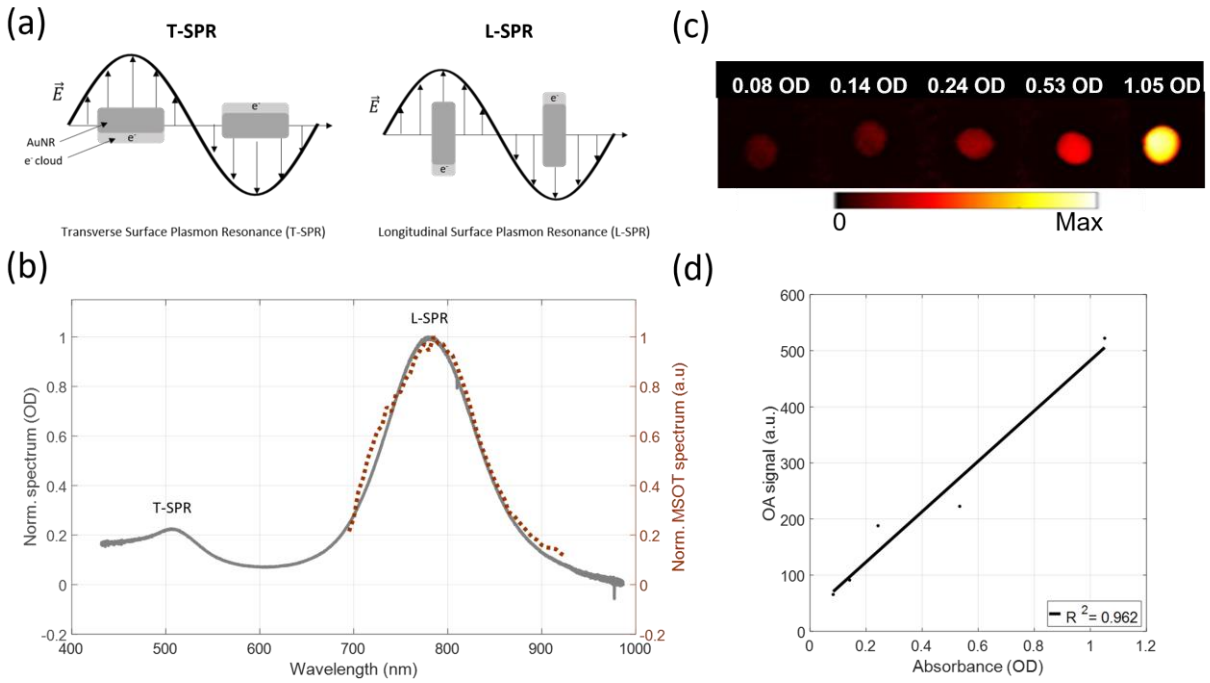

Figure 5.1. AuNRs as an exogenous contrast agent for vasculature enhancement in OA imaging. (a) SPR in AuNRs due to the oscillation of the short and long axes of the nanorods in an applied electromagnetic field. (b) Normalized surface plasmon absorption spectra of AuNRs measured with a spectrometer (420 - 980 nm) in gray and MSOT (700 - 920 nm) in red. (c) Reconstructed OA images from phantoms with different AuNRs concentration. (d) Linear correlation (R^2 = 0.962) between OA absorption and AuNRs concentration (OD) at 780 nm.

5.3 *In vivo* challenges

Several challenges needed to be addressed while performing *in vivo* experiments, which were related to both the injection of the exogenous contrast agent as well as to normal physiological changes in living mice.

First, the correct amount of AuNRs to be injected was experimentally investigated with *in vivo* imaging to provide enough signal enhancement compared to endogenous absorbers while avoiding light fluence. For the experiments, two nude mice M1 (4 weeks old, 19.9 g) and M2 (4 weeks old, 18.7 g), were anesthetized, placed in the animal chamber, and imaged with MSOT. The two mice were injected with a different dose of AuNRs solution (78 nM), 100 µL for M1 and 40 µL for M2. In both mice, an abdomen section showing the left and right kidneys was chosen as the anatomical ROI for OA imaging. The OA images of M1 acquired before and after 100 µL AuNRs injection are reported in Fig. 5.2a, b and compared with the OA images from M2, which was injected with a lower AuNRs dose, 40 µL (Fig. 5.2d, e). Notably, the OA image after 100 µL AuNRs injection shows a reduction in the OA signal from deeper structures due to the light fluence. Instead, the OA image acquired after 40 µL injection (Fig. 5.2e) noticeably demonstrates a global OA signal enhancement – from superficial vessels to deeper structures.

Fig. 5.2c and Fig. 5.2f report the images of the enhanced OA signal in the abdomen section after 100 µm and 40 µL injection respectively, which were obtained by subtracting the OA images before and after injection. While for 40 µL injection (Fig. 5.2f) a homogeneous signal enhancement over the entire mouse section is reported, for 100 µL injection a higher OA signal is detected from superficial structures, although this signal quickly drops after a few millimeters' depth due to light fluence. Indeed, the higher AuNRs concentration inside the mouse body results in an increased amount of light absorbed in the first centimeter of tissue, which reduces the amount of light that is able to penetrate deeper into the mouse. Based on these results, 40 µL (78 nM) was defined as the amount of AuNRs to be injected in a 4-week-old nude mouse of weight around 20 g to enhance OA signal in vessels while preserving anatomical structures.

Second, a breath-gating strategy was applied to the acquired frames to reduce motion artifacts due to respiration as well as signal amplitude variations due to changes in blood oxygenation during breathing (see Chapter 4.2)

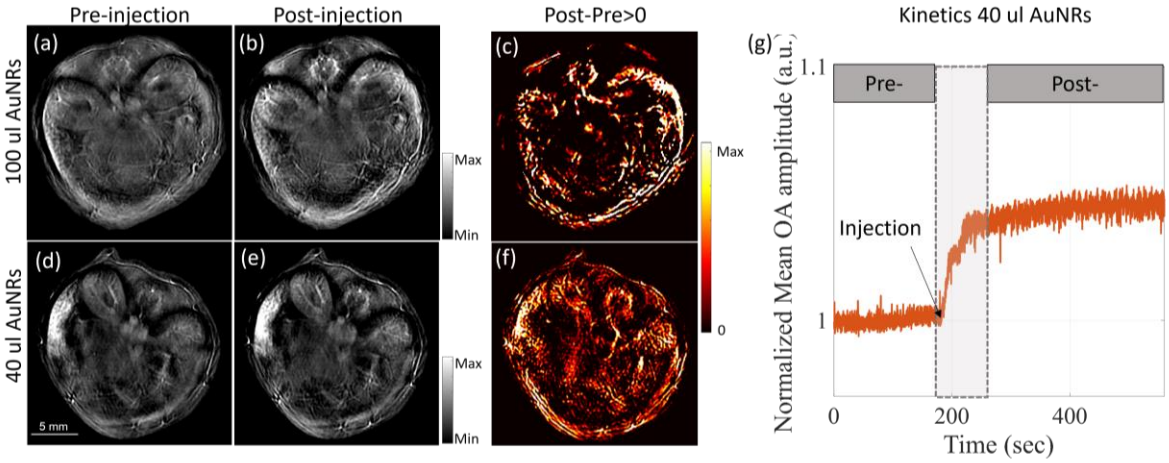

Figure 5.2. *In vivo* challenges of using AuNRs as a contrast agent to label vessels. Mouse abdomen section before (a) and after (b) injection of 100 µL AuNRs, showing OA signal reduction in deeper tissue due to fluence. Mouse abdomen section before (d) and after (e) injection of 40 µL AuNRs, showing signal enhancement of vasculatures. OA enhanced images for 100 µL (c) and 40 µL (f) estimated by taking the positive difference between the image Post- and Pre- injection. (g) kinetics of AuNR perfusion in *in vivo* mouse after 40 µL injection, showing a fast increase of the OA signal intensity after AuNR injection, followed by a plateau after 1 min.

Third, the *in vivo* imaging protocol was carefully considered based on the specific requirement of using AuNRs for vessels labeling. Indeed, for vasculature enhancement, the OA images must be acquired in a precise time window during and after injection to ensure that 1) AuNRs are distributed in the full circulatory system of the mouse and 2) they are not already extravasating and accumulating within the organs. Fig. 5.2g. reports the kinetics of AuNRs perfusion for the 40 µL injection in M2. The kinetics curve was obtained by plotting the normalized mean OA signal intensity of the images acquired before, during, and after the injection time point (frame rate of 10 Hz) at the expiratory pauses. As shown, the OA signal intensity quickly increases after AuNRs injection and reaches a plateau value after 1 min, demonstrating that there is a transient time before all the AuNRs are distributed in the full circulatory system. For this reason, the images acquired during and 1 min after the injection point were discarded from the analysis. Furthermore, to avoid excessive data collection and AuNR extravasation, the acquisition time after the injection was fixed at 6 min. Indeed, as reported in [162] after 1 h from the time of injection, the AuNRs start accumulating in the main organs, in particular the kidneys, liver, and spleen, thus reducing the accuracy of the nanorods to specifically enhance only vasculatures.

The last *in vivo* challenge was related to the expected versus measured OA signal enhancement for certain amounts of injected particles. The optical absorption of whole blood at 780 nm is reported around 3 OD [55], and assuming that the total amount of blood in a mouse is around 2 mL in volume and 40 µL of AuNRs at 78 nM (68 OD at 780 nm) were injected, the expected increase in the blood absorption due to AuNRs was around 1.3 OD. However, an enhancement in absorption of only 5% was reported *in vivo* (Fig. 5.2g), while an enhancement of 40% was expected according to the calculation. This discrepancy is probably due to biological effects.

5.4 Proposed *in vivo* validation method for vasculature enhancement.

After addressing all the challenges related to the OA *in vivo* imaging with AuNRs, the final protocol for the *in vivo* validation method was defined and is schematically reported in Fig. 5.3a. The nude mouse was injected with 40 µL (78 nM) AuNRs, an amount that our pilot studies indicated can provide high optical contrast while preventing fluence attenuation effects in the mouse abdomen based on the mouse weight. The OA data was continuously acquired at 780 nm (AuNR peak) for a period before (3 min), during (15 sec) and after (6 min) the AuNRs bolus injection, resulting in a total of 5400 frames (frame acquisition rate of 10 Hz with laser repletion rate of 10 Hz).

A post-processing breath-gating strategy was implemented to find the best aligned frames before and after AuNR injection. Pre- and post-injection images were accurately aligned as follows. First, all acquired frames were clustered according to the breathing cycle (see Chapter 4.2). Subsequently, the frames at the expiratory pauses were extracted and averaged to increase SNR (Av Frame Pre and Av Frame Post), while frames corresponding to inhalation, respiratory peak and exhalation were discarded. The alignment accuracy between the pre- and post-injection images was quantified using the SSIM index. The positive difference image obtained by subtracting the aligned frames before and after injection provided the ground truth for vessel detection. Fig. 5.3b reports the averaged aligned frames pre and post injection, and the ground truth image for vessel detection in an in vivo moue abdomen section (Fig. 5.3b).

To validate a generic vessel enhancement algorithm, the algorithm is applied to the OA image pre-injection and the resulting vessel enhanced image is compared with the estimated vessel ground truth, as previously described. The SSIM between the vessel enhanced image and the ground truth is used to quantify the accuracy of the algorithm to enhance vessels.

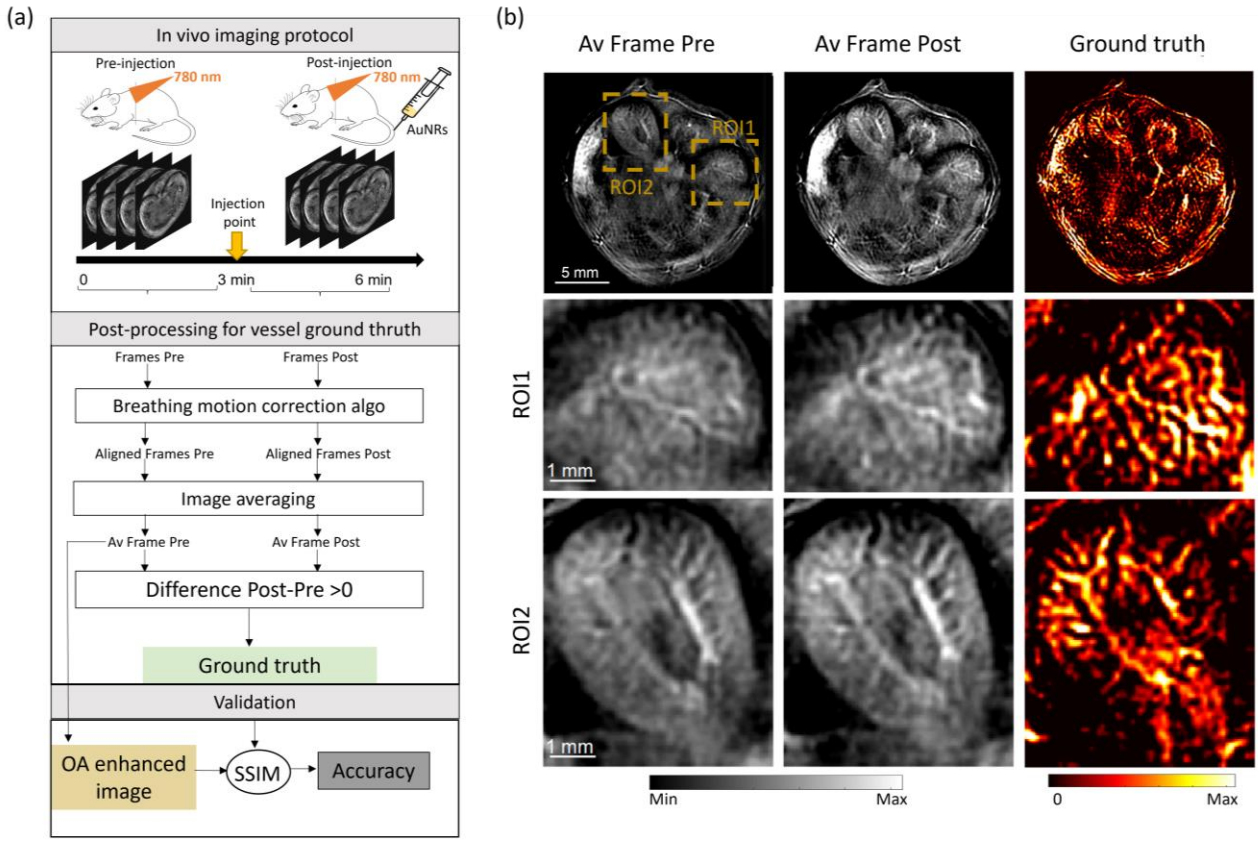

Figure 5.3. In vivo validation method for vasculature enhancement algorithms. (a) The mouse is injected with 40 µL (78 nM) AuNRs and OA data are continuously acquired at 780 nm for 3 min before injection (Pre-injection) and 6 min after injection (Post-injection). A post-processing breath-gating strategy is implemented to find the best aligned frames before and after AuNR injection. Only the frames at the expiratory pause are selected (Aligned Frames Pre and Aligned Frames Post) and averaged to increase SNR (Av Frame Pre and Av Frame Post). The positive difference image obtained by subtracting the aligned frames before and after injection provides the ground truth for vessel detection. The resulting vessel enhanced image is compared with the estimated vessel ground truth. The SSIM between the vessel enhanced image and the ground truth is used to quantify the algorithm accuracy to enhance vessels. (b) Averaged frames pre and post injection, and ground truth image for vessel detection in an in vivo moue abdomen section. Magnification of two region of interests in the right (ROI1) and left (ROI2) kidney with enhanced vasculatures in the ground truth images.

5.5 Discussion and Conclusions

As OA technologies advance and more biological applications arise, there is an increased need for *in vivo* standardized approaches to evaluate the accuracy of the tools being developed.

Here, a new *in vivo* validation approach to assess the accuracy of vasculature enhancement algorithms in OA is proposed. The validation method developed is meant to provide a ground truth image of the vasculatures inside the mouse body, which can be used as a biological reference to quantify the validity and applicability of the enhancement algorithms. While the current work focuses on OA macroscopy – which is more affected by background noise and artifacts – the proposed approach could be easily rescaled and extended to mesoscopy and microscopy. Furthermore, the framework can be used not only to evaluate the performance and the limitation of other imaging algorithms, but the results of the validation studies can also help in improving image-processing performances.

The validity of the proposed *in vivo* validation methods is demonstrated with a real OA application, as presented in the following chapter.

5.6 Application: Assessment of Hessian-based Frangi filter in OA for vasculature enhancement

The results in this chapter are also presented in the publication entitled:

- *"Assessment of hessian-based Frangi vesselness filter in optoacoustic imaging"*, Antonia Longo, Stefan Morscher, Jaber Najafababdi, Dominik Jüstel, Christian Zakian, Vasilis Ntziachristos

5.6.1 Introduction

OA images typically employ the Hessian-based Frangi vesselness (HFV) filter [137] for enhancing the visualization of vasculature [163-167]. The filter is applied on a per image voxel and is based on eigenvalue decomposition of the local Hessian matrix of the image. Therefore, the local structure of a voxel (i.e., tubular, blob-like or plate-like) at each scale is encoded in the sign and amplitude of the Hessian eigenvalues. By selecting specific eigenvalues and defining a vesselness function, the contrast of vessels is enhanced, while non-vascular structures and background noise are suppressed.

Although the Hessian-based Frangi vesselness (HFV) filter is an established tool in OA imaging, the *in vivo* accuracy evaluation of HFV filters in OA imaging is still an unexplored challenge. Indeed, simple experimentation with the HFV filter reveals that different filter parameters (scales) produce markedly different images (Fig. 5.4). This finding introduces an inherent uncertainty in relation to which of the images generated is the most reliable representation of the object imaged. Assuming that only one of the images generated after HFV processing is an accurate representation, other images with a higher filter scale contain then artefacts, in particular in the sense of artefactual vessels. This performance and conditions have not been systematically assessed so far.

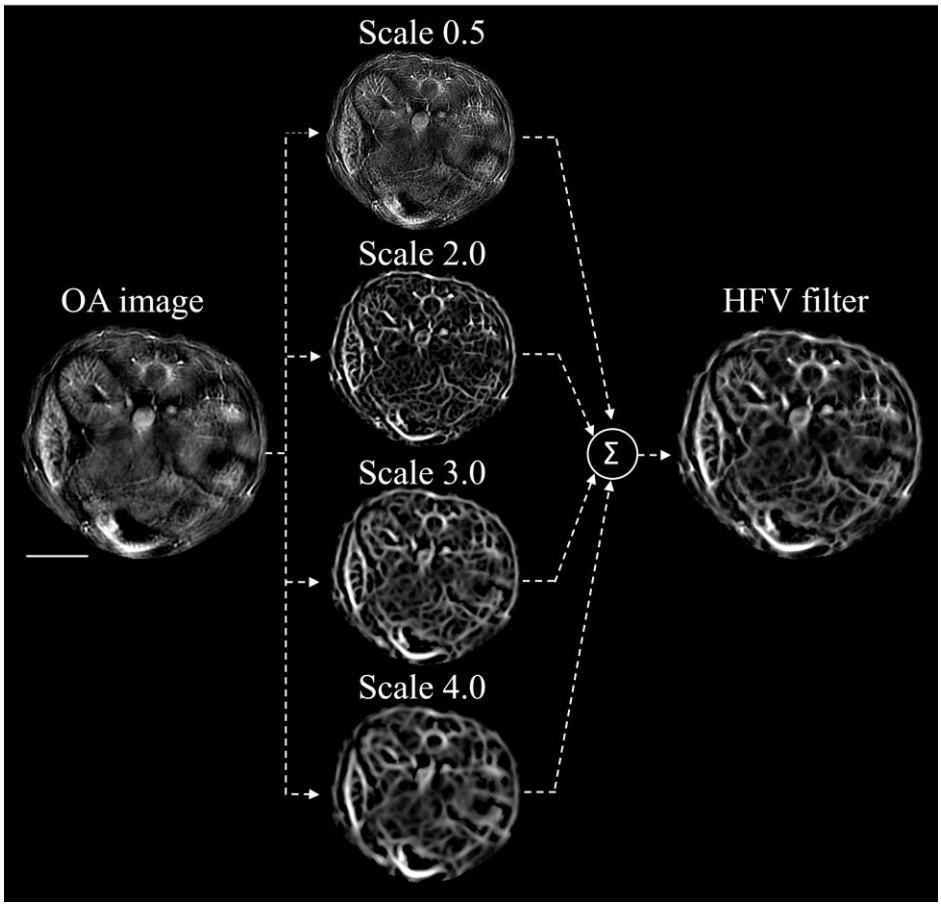

Figure 5.4. Effect of different filter scales on the performance of the HFV filter in in vivo OA image of mouse kidney section. Reconstructed OA image of a mouse abdomen section (OA image) and HFV filtered image for scales 0.5 (Scale 0.5), 2.0 (Scale 2.0), 3.0 (Scale 3.0) and 4.0 (Scale 4.0), respectively, to enhance vessel diameters ranging from one half to six times the system resolution of 165 µm. Resulting multi-scale blend (average) of the HFV filtered images of the mouse abdomen.

Guided by the observation of Fig. 5.4, we hypothesized that the HFV filter can generate artefactual vessels on the processed images and compromise the accuracy and fidelity of the OA images. Therefore, we performed a critical assessment on whether improvements in the visual appearance of the image collected are done at the expense of image accuracy.

Using experimental measurements on phantoms, we systematically evaluate the contribution appearance of artefacts on the images as a function of HFV filter parameters. Furthermore, we studied the accuracy achieved with HFV filtering as a function of sample/tissue type, optoacoustic set-up employed, motion and other experimental parameters. Understanding of the effects of these parameters allows us to make recommendations on the use of the HFV filter.

To assess the biological accuracy, we introduce a novel method for in vivo validation of the HFV filter in OA imaging using gold nanorods (AuNRs) as contrast agent to label vessels in mice. We discuss the implications of using the HFV filter to improve real vessel detection in relation to preserving image features in vivo.

5.6.2 Hessian-based Frangi filter in OA imaging

The Hessian-based Frangi filter extracts tubular structures from an OA image by classifying the eigenvalues of the Hessian matrix via a vesselness function. A two-dimensional OA reconstructed image $I(\bar{x})$ is observed at a scale $s > 0$ by convolution with a Gaussian kernel $G_s(\bar{x})$ with standard deviation s. The normalized Hessian matrix $H(\bar{x}, s)$ of the resulting image $I_s(\bar{x}) = I * G_s(\bar{x})$ at scale s is then given by:

$$H(\bar{x}, s) = B \frac{\partial^2}{\partial \bar{x}^2} I_s(\bar{x}) = B \left(\frac{\partial^2}{\partial \bar{x}^2} G_s \right) * I(\bar{x}), \tag{5.1}$$

where B is a normalization factor, and the second equality follows by partial integration and is used for implementation. The 2D Frangi vesselness function for vessels with bright contrast (as in OA) is defined as:

$$v(\bar{x}, s) = \begin{cases} 0 & if\ \lambda_2(\bar{x}, s) > 0 \\ \exp\left(-\frac{R_b^2(\bar{x}, s)}{2\beta_1^2}\right)\left(1 - exp\left(-\frac{S^2(\bar{x}, s)}{2\beta_2^2}\right)\right) \end{cases} \tag{5.2}$$

where $\lambda_1(\bar{x},s)$ and $\lambda_2(\bar{x},s)$ are the sorted eigenvalues ($|\lambda_1(\bar{x},s)| < |\lambda_2(\bar{x},s)|$) of the image Hessian at position $\bar{x}$ at scale s; $R_b^2(\bar{x},s) = \frac{|\lambda_1(\bar{x},s)|}{|\lambda_2(\bar{x},s)|}$ and $S^2(\bar{x},s) = \sqrt{\lambda_1(\bar{x},s) + \lambda_2(\bar{x},s)}$ are the *blobness* and *structureness* measures [168], respectively used to distinguish vessels from blob-like structures and noise/background; parameters $\beta_1$and β_2 tune the sensitivity of the filter to the measures R_b and S.

The values of β_1 and β_2 are set heuristically to suppress blob-like structure and background noise ($i.e. \beta_1 = 1; \beta_2 = \frac{\max_{\bar{x}} S^2(\bar{x},s)}{2}$), in agreement with [138, 168]. The range of scales *s* are selected to enhance vessels from one half to six times the system resolution of 165 μm (i.e., scaled between 2 and 10 pixels). Other filter parameters were set to classify vessels and suppress blob-like structures and noise as in previous studies [168]. The final vessel-enhanced image is obtained by analyzing the vesselness function in equation (2) at different scales *s* and by blending (summing) the filter responses.

Therefore, the performance of the HFV filter was quantified using the SSIM [158] between all unfiltered OA images and corresponding HFV-filtered images.

5.6.3 Methods

All phantoms and *in vivo* OA experiments were conducted using a commercially available, real-time, multispectral optoacoustic tomographic (MSOT) small animal scanner device (inVision 256-TF, iThera Medical GmbH, Munich, Germany). All acquired data were filtered using a digital band-pass filter between 300 kHz and 8 MHz and reconstructed using a conventional backprojection algorithm. Then the HFV filter was applied to the reconstructed images during post-processing.

To adjust image contrast, a histogram-based thresholding method was applied to all OA and HFV filtered images by removing 0.5 % highest and 0.02 % lowest pixel values. Note that the process was applied only to improve image visualization, and all quantification metrics were estimated on the raw images.

<u>Phantom experiments</u>

Phantom experiments were performed to independently investigate the effect of filter scales, light fluence, limited tomographic angular coverage, out-of-plane signal, proximity to air cavities, and image CNR. A standard OA phantom with the highest CNR was obtained by embedding a black

vessel-like shape printed on white paper in 12 mm-diameter turbid agar cylinders. The turbid agar cylinder was made with 3% w/m agar gel (Fluka Analytical, Germany) and 6% v/v intralipid-20% (Sigma Aldrich, Germany) to ensure similar scattering properties as in biological tissues (~10 cm^{-1}). This phantom was used to investigate the effects of filter scales, light fluence, and limited tomographic view on the filter performance.

To evaluate the effects of different CNR values, two additional phantoms were obtained by changing the absorption of the agar and the color of the vessel-like shape (black and gray): 0.05 OD of India ink was added to the turbid agar for middle CNR (black vessel-like printed shape) and low CNR (grey vessel-like printed shape) phantoms.

To investigate the influence of out-of-plane signal, a black transversal line was printed on white paper and positioned at the image plane, while the out-of-plane signal was produced by placing the grey vessel-like printed phantom 700 nm away from the image plane. In another phantom, an air cavity was introduced by producing a tubular hole along the agar cylindrical phantom to investigate the effect of strong acoustic reflection.

The HVF filter was applied on the OA reconstructed images with scales ranging between 2 and 10 pixels. Other filter parameters were set to classify vessels while reducing the enhancement of blob-like structures and noise as in previous studies [168]. All unfiltered OA images and corresponding HFV-filtered images were qualitatively compared using the structural similarity index SSIM.

The CNR in a region of interest was calculated by subtracting signal in the background from a non-vessel region within the phantom and dividing the difference by the standard deviation of the noise from a region outside the phantom.

In vivo experiment

The *in vivo* validation of the HFV filter in OA imaging was obtained by following the procedure reported in Sec. 5.4. A section through the mouse abdomen was chosen as the anatomical region of interest for optoacoustic imaging and AuNRs were injected into the mouse for labeling vessels and generating the ground truth image containing vasculatures. The estimated vessel ground truth was compared with the resulting vessel enhanced image (i.e., HFV-filtered image) obtained by applying the HVF filter on the optoacoustic reconstructed image of the mouse abdomen. The SSIM was used to quantify the accuracy between the vessel enhanced image and the ground truth.

The renal pelvis of the left kidney was taken as the background region for CNR calculations in the pre-injection image, as no OA signal is expected in this area. The noise standard deviation was calculated from a region outside the mouse section.

5.6.4 Results

Measurements in stable phantoms were used to independently assess the impact of different variables on HFV filter accuracy, including CNR, tomographic angular coverage, out of plane signal, presence of air cavity in the image, fluence and filter scales.

Indeed, since tomographic optoacoustic images often lack in contrast and exhibit poor signal to noise ratio, we first tested the performance of the filter under different CNR conditions. For this purpose, three phantoms consisting of vessel-like shapes printed on white paper were embedded in a turbid scattering agar cylinder and imaged with inVision 256-TF (iThera Medical, Munich, Germany). OA images of different CNR were considered by changing the absorption of the agar and the printed phantom, as described in the Methods section.

Fig. 5.5a,b shows the optoacoustic image and corresponding HFV filtered image obtained without background absorption, resulting in a CNR of 44.8 dB. By adding background absorption in steps of 0.05 optical density and changing the absorbing phantom from black to grey, we also obtained images at CNR of 32.9 dB (Fig. 5.5c, d) and CNR of 26.3 dB (Fig. 5.5e, f). As clear on the images, application of the HFV filter results in the appearance of artefactual blood vessels. For example, observation of Fig. 5.5f shows that the appearance of the printed structure improves. Nevertheless, we also observe the appearance of a multitude of interconnected small vessels throughout the image, which although they appear realistic, they show up in areas of the object where only white paper exists. A similar effect is observed also in Fig. 5.5d. In fact, the creation of artificial vessel structures from background absorption results in a reduced structure similarity index (SSIM) value, obtained by comparing the optoacoustic image with the HFV filtered version.

The generation of artificial vessel structures from background absorption results in a reduced SSIM value as the CNR decreases.

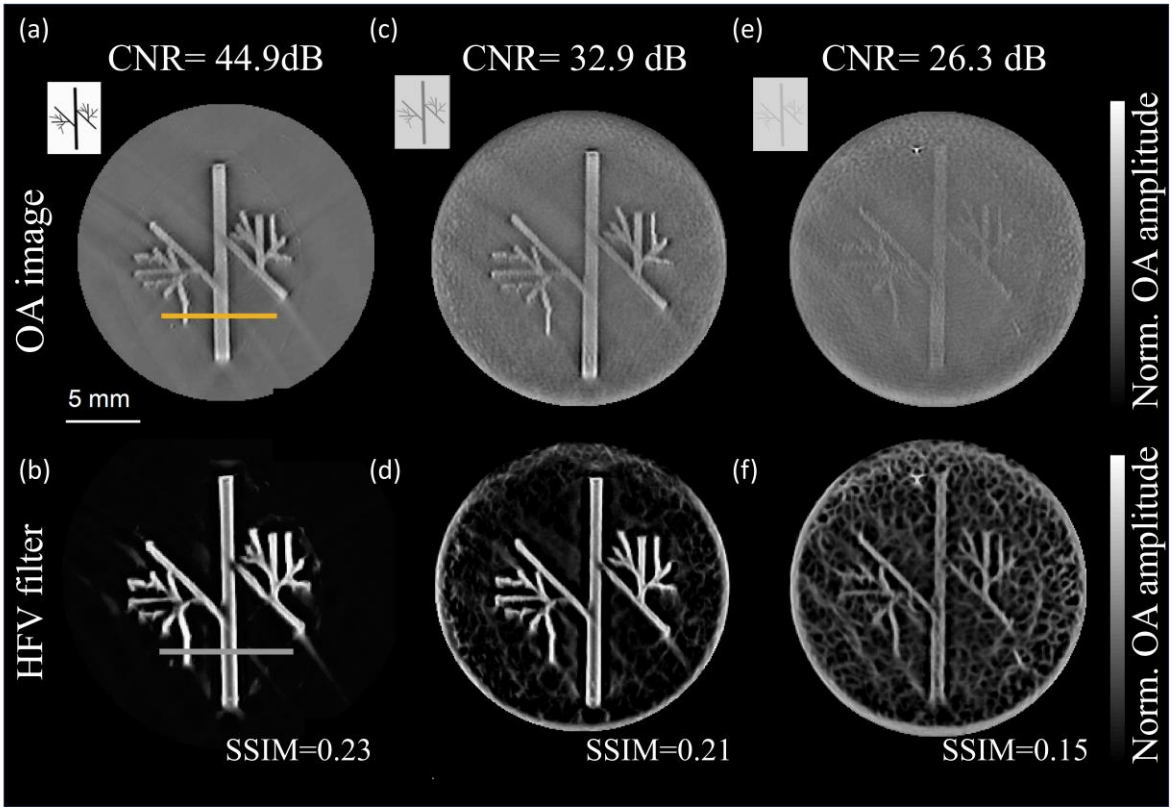

Figure 5.5. Effect of CNR in the performance of the HFV filter in OA imaging. Experimental validation of the HFV filter application to OA phantom images with different CNR (a, c, e) and corresponding HFV filtered images (b, d, f). The insets at the upper left of panels (a), (c) and (e) show the vessel-like printed papers used to simulate different OA absorption (black and grey) and the corresponding absorbing agar phantoms. HFV: Hessian-based Frangi vesselness, SSIM: structure similarity index, CNR: contrast-to-noise ratio.

Having established that the HFV filter can perform poorly and generate artefact depending on the image CNR, we examined whether this unreliability was even stronger in the more realistic situation of limited-view coverage. All commercial optoacoustic tomography systems collect data from less than 360 degrees around the sample for practical reasons, meaning that artefacts arisen from the reconstruction algorithms propagate in the post-processed HFV filtered images. For this purpose, limited tomographic views were tested by reducing the number of reconstructed channels for the phantom with highest CNR from 270° (original, Fig. 5.5a) to 125° (Fig. 5.6a). As shown in Fig. 5.6b, ray artefacts due to limited view reconstruction of Fig 5.6a are highlighted by the filter, thus suggesting a careful use of the filter when full angular coverage in not guaranteed.

We also investigated the influence of out of plane signals on the HFV filter performance; although cylindrically focused transducers are usually employed in tomographic systems to minimize the sensitivity out of the image plane as already discussed in Sec. 2.2.2.4, low frequencies signals from different planes are still detectable from the transducer. To demonstrate this effect, a black transversal line was printed on white paper and positioned at the image plane, while the out-of-plane signal was produced by placing the grey vessel-like printed phantom 700 nm away from the image plane. No out-of-plane effects were observed for separations above 1 mm from the image plane (data not shown), which corresponds to the elevation resolution of the transducer array. Fig 5.6c,d shows the low frequency content of the out of plane signal from the vessel-like printed shape and the HFV filtered image. As shown in the figure, structures out of the image plane and not in focus can be falsely enhanced, and appear as double structures.

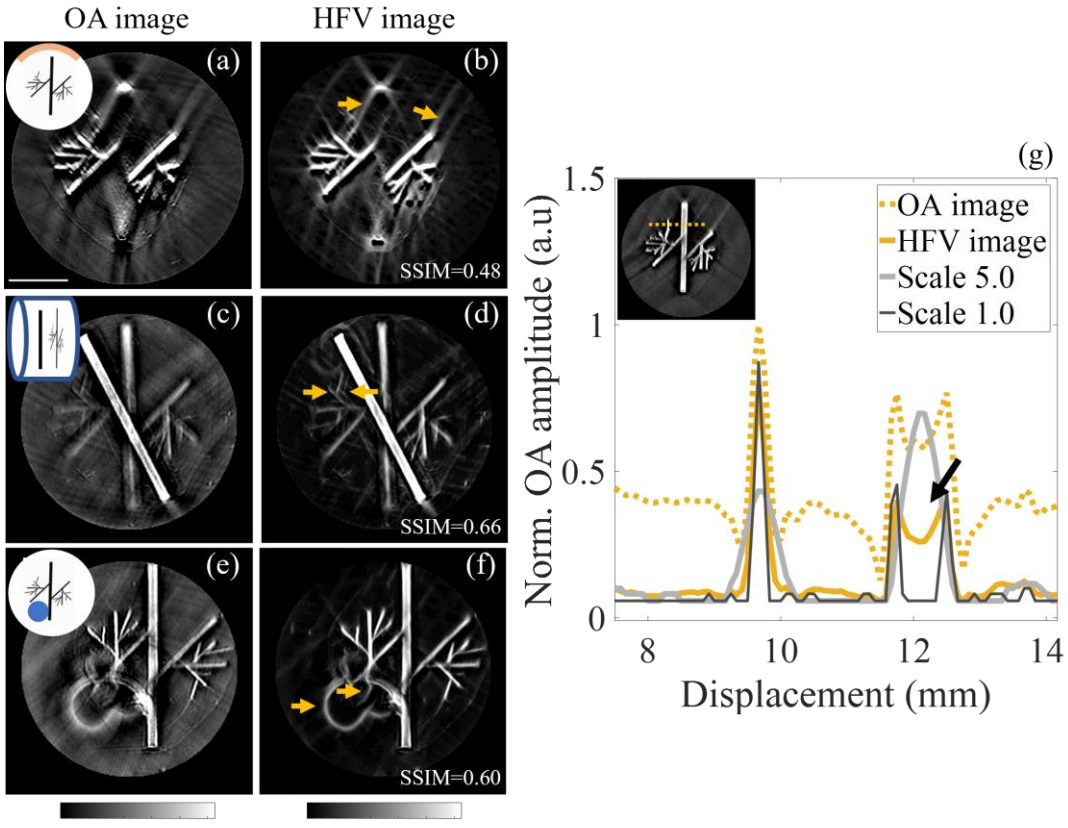

Figure 5.6. Effect of different system variables on the performance of the HFV filter in experimental OA phantoms. (a, b) Limited tomographic view, (c, d) out-of-plane signal (c, d) presence of an air cavity, and (g) different filter scales and contrast variation in a large vessel. Arrows show artifact enhancement after application of the HFV filter.

A further analysis was then performed to demonstrate the effect of air cavities in proximity of the image plane. In optoacoustic tomography, especially for small animal systems, organs of interest in the abdomen sections such as liver or kidneys are in the same field of view of certain regions containing air like lungs, stomach or intestine; Indeed, no OA signal is expected from these regions and additional acoustic reflections may be generated due to acoustic mismatch. For this purpose, an air cavity was introduced in the vessel-like printed phantom by producing a tubular hole of 3 mm diameter along the agar cylinder. Fig. 5.6f displays the enhanced artefacts in the HFV filtered image due to strong ultrasound reflections at the air cavity boundary where no OA signal is expected.

Furthermore, the effect of different filter scales on image resolution was investigated. Fig. 5.6g shows the intensity line profiles of the unfiltered and corresponding HFV-filtered OA images of the phantom with the highest CNR, and the effect of two filter scales, i.e., small scale (Scale 1.0) and large scale (Scale 4.0). As shown in the figure, while the large scales compromise the resolution of small structures, the small scales enhance only structural edges. Moreover, a depth-dependent contrast variation in a large vessel due to light fluence, arrow in Fig. 5.6g, can be also enhanced by the filter using small scales if not corrected. These examples demonstrate that, although filter scales are carefully chosen, the response of the filter is typically not uniform between vessels of different radii.

After assessing the performance of the filter under different conditions, we rigorously validated our findings in vivo. In particular, the ability of the HFV filter to improve real vessels detection while preserving image features was questioned.

For this purpose, AuNRs were selected as an exogenous contrast agent to label vessels and injected in a nude mouse. The differential OA image obtained by subtracting the image pre-injection from the image post-injection was used as gold standard for vessel localization (as previously described in Sec. 5.4) and compared with the HFV filtered image:

Fig. 5.7 shows the in vivo validation of the HFV filter. The positive difference image (Diff) was calculated by subtracting pre-injection image from post-injection ones and compared with the optimized HFV-filtered pre-injection image (HFV Pre) using SSIM. Optimized HFV filter was

also applied to the Diff image (HFV Diff) for comparison and the SSIM between HFV Diff and Diff image is reported.

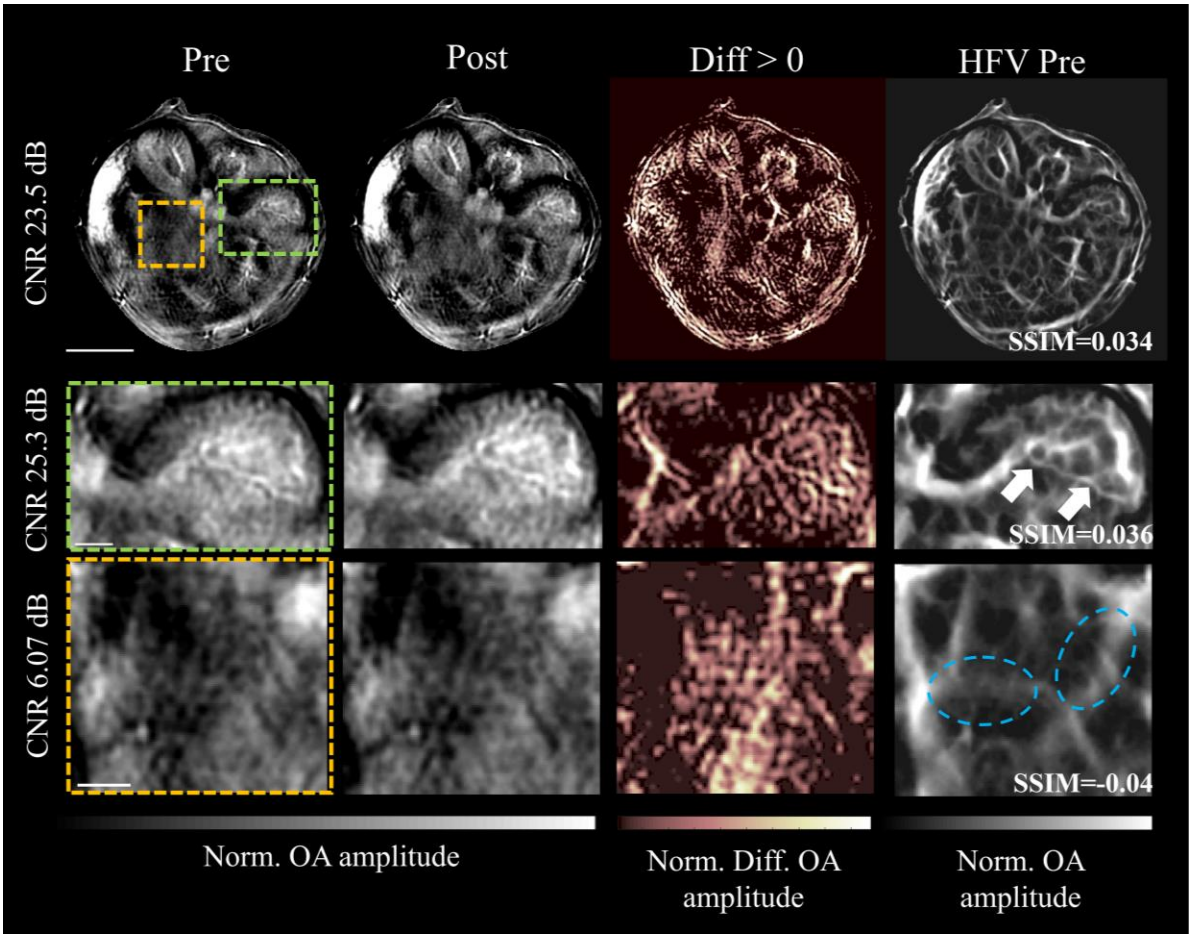

Figure 5.7. In vivo validation of the HFV filter in mouse abdomen at 780 nm. Top row: unfiltered OA images of the mouse abdomen. The boxes indicate regions of interest also analyzed as zoomed-in views. Middle and lower rows: Zoomed-in views of the two regions of interest with different CNRs: a region in the right kidney with CNR 25.33 dB, and a region closer to the stomach with CNR 6.07 dB. Vessel-enhanced images (Diff), generated as described in the text, were compared with the optimized HFV-filtered pre-injection image (HFV Pre) in terms of the structure similarity index (SSIM). Enhancement of real vessels after HFV filter are marked with white arrows. False vessel-like structures generated from background noise are marked with cyan circle.

Two regions of interest (ROIs) within the abdomen section were selected and magnified for further analysis: a region in the right kidney with higher CNR (25.3 dB), and a region closer to the stomach

with a lower CNR (6.07 dB). The in vivo validation results show an overall visual improvement in the OA contrast after HFV filtering at the expense of biological accuracy. In the right kidney region (CNR=25.3 dB), the vascular network is enhanced by filtering (SSIM=0.036, white arrows in the figure); in the region close to the stomach with lower CNR (CNR=6.07 dB), false vessel-like structures are created from the background (cyan circles in the figures), leading to a negative SSIM index of -0.04. Indeed, the comparison between the HFV Pre image and HFV Diff image highlights the importance of adequate CNR for accurate representation of vessel structure using HFV filter.

5.6.5 Discussion and Conclusions

In this work, we examined whether application of the common HFV filter, used to enhance vessel contrast, compromises optoacoustic image fidelity. The study included both controlled phantom measurements and animal images obtained under different experimental conditions. We demonstrated that the performance of the filter varies with the CNR and morphological features of the image, and that this variation can result in the appearance of distorted or non-existent vasculature. Notably, we observed both in phantoms and in vivo that the filter generates false vessel-like structures from random patterns of background tissue absorption in optoacoustic tomographic images. The HFV filtered images at separate scales raise uncertainty in the biological accuracy of the filter for in vivo application, also confirmed by the low SSIM index at each scale. These findings call into question the whether the HFV filter can be accurately applied in in vivo optoacoustic imaging. Therefore, a critical assessment whether improvements in the visual appearance of the image is done at the expense of image accuracy is reported.

Using optoacoustic phantoms, we studied the effect of different parameters on the HFV filter performance. We demonstrated for the first time the importance of appropriate angular coverage and the avoidance of air cavities in the sample to prevent artifacts enhancement in the HFV filtered image. We showed that false vessel-like structures are created from bulky tissue absorption. We further confirmed that the artifacts observed are more pronounced as the CNR in the image drops. Therefore, since the CNR's of optoacoustic images vary with depth, the findings herein imply that the performance of the HFV filter is also depth-dependent and artifactual vessels can be generated in deeper fields of view.

We validated the performance of the HFV filter in vivo by comparing filtered optoacoustic images of a mouse abdomen to unfiltered images of the same region after enhancement of the real vessels with injected gold nanorods. When compared to the nanorod-labelled vessels, it was clear that the vasculature network was not faithfully reproduced in the HFV-filtered images (Fig. 5.7). Furthermore, this in vivo experiment confirmed our ex vivo observations that the HFV filter behaves unreliably in regions of interest with low CNR, such as close to the stomach or intestines, or in regions containing only pure background tissue absorption. Therefore, identifying the limits and capabilities of the filter in a common in vivo experimental scenario may drive future researches in the accurate use of HFV filter without compromising the biological accuracy of the OA images.

In conclusion, we have demonstrated here that the HFV filter produces inconsistent or misleading results when applied to optoacoustic images of non-ideal subjects. Specifically, the filter does not cope well with variations in depth and contrast index. The filter is also susceptible to errors when a limited-view detector is used, or when air pockets are present in the subject. To mitigate erroneous interpretation of optoacoustic tomographic images, we recommend that the HFV filter should be employed with the following limitations: transducer angular coverage higher than 270°; avoidance of air cavity in the image plane or strong acoustic reflection artefacts in the acquisition; depth-dependent contrast compensation to account for light attenuation primary, and acoustic attenuation secondly; CNR value above 24 dB for the in vivo biological accuracy.

To conclude, this study may serve as a foundation to guide future standardization of OA system performance, which will improve technological advancement, clinical translation, and regulatory evaluation of OA imaging.

6 Summary and outlook

6.1 Summary and conclusions

This dissertation reports original work in image quality and visualization improvement in OA tomographic imaging. The contribution can be summarized as follows.

We reported a detailed analysis on image quality degradation in OA imaging. We demonstrated that the degradation process may occur at every level of the imaging formation chain, from signal generation and detection to the *in vivo* imaging and system operation. This contribution provides a technical guidance for the future design and development of new systems and algorithms for OA

imaging. Furthermore, the reported findings can support biologists and clinicians on better OA image interpretation (i.e., artifacts recognitions), experimental protocol design, and system use.

We presented new standard methods to improve image quality while assuring biological accuracy in OA imaging. The proposed approaches tackle different levels of the image formation chain in OA.

1) Signal detection. We proposed a new transducer design with optical shielding to reduce parasitic noise and assure accurate sensing of the OA signal. This improvement is in high demand, since OA signal has weak amplitude (Pa or sub- Pa range, primarily limited by the maximum light permissible exposure) and it is often obscured by broadband noise. The proposed solution represents a crucial advancement in the transducer technologies for OA applications, as this approach increases system sensitivity, SNR, and image penetration depth and enables broadband signal detection without information loss.
2) *In vivo* imaging. We implemented an automatic breathing motion correction algorithm to improve image quality and quantifiability. The proposed method enables enhancement of small anatomical details in 2D and 3D images and increases the fidelity of the structures being imaged. Furthermore, by improving quantification and signal unmixing, this method increases the system sensitivity to detect biological processes in living mice that are otherwise hidden by physiological changes related to breathing.
3) Image reconstruction and visualization. We introduced fbMB reconstruction to separate frequency-band-specific OA image components during image formation, thereby enabling structures of all sizes to be rendered with high fidelity. fbMB produces OA images with improved contrast and fidelity, which reveal anatomical structures in *in vivo* images of mice in unprecedented detail. These enhancements further improve the accuracy of spectral unmixing in small vasculature. By offering a precise treatment of the frequency components of OA signals, fbMB improves the quality, accuracy, and quantification of OA images and provides a method of choice for OA reconstructions.

To the best of our knowledge, this is the first work that brings together image quality and quantification improvements and demonstrates their strong interconnection. Although the primary

goal of the thesis was image quality improvement, we have demonstrated that the achievement thereof had the side benefit of also improving image quantifiability.

Finally, we discussed and presented the implications and the challenges on developing standard methods to assess the biological accuracy and efficiency of image processing tools for image quality improvement in *in vivo* OA imaging.

We believe that the methods developed in this work represent a unique contribution in biomedical OA imaging towards the improvement of image contrast while assuring biological accuracy. Furthermore, the findings reported in this dissertation can be easily rescaled and extended to OA mesoscopy and microscopy or adapted for other medical imaging modalities.

The image quality improvement will enable high-fidelity information extraction from MSOT images. The enhanced image contrast and visual perception of anatomical structures will pave the way for more biological and clinical applications and ultimately advance the translation of OA technologies into clinical practice.

6.2 Outlook

OA imaging has rapidly grown in the last two decades, owing to great developments in the technologies as well as in data processing capabilities. However, the performance of OA technologies and their impact on biological and medical applications can be further improved. The envisioned next steps can be summarized as follow.

Regarding algorithms, strong advancements have been made on modelling and incorporating tissue and transducer properties into the reconstruction frameworks. These methods remove artifacts and provide images with increased contrast and accuracy, ultimately for a better image interpretation. However, the issue remains that, due to their complexity, these reconstruction approaches are computationally expensive and require long running times. Therefore, the present challenge is to make these tools available for real-time imaging so that clinicians can have direct feedback on structures being imaged.

To further improve biological accuracy in OA imaging, information from other medical imaging modalities could be included in the reconstruction algorithms. For example, a particular concern in clinical OA images is the appearance of reflection artifacts due to the intrinsic acoustic properties of the tissue being imaged, which mislead image interpretation. To mitigate these

artifacts, acoustic properties of the tissue could be retrieved from ultrasound images and integrated in the OA reconstruction frameworks.

Another challenge in OA imaging is represented by the development of fluence correction algorithms, whose applicability is strongly limited by the uncertainty in the optical properties of biological tissue. Therefore, fluence correction remains an unsolved issue in OA imaging, and the corresponding solution could result in significant performance improvement.

Further efforts in OA imaging must be focused on increasing image penetration depth by optimizing tissue illumination and by employing advanced image analysis and machine learning tools. This will open the perspective of OA imaging to new clinical applications in biomedicine.

Besides instrumentation and image processing, there is a growing need in the development of both verification and validation tools, i.e., methods to accurately evaluate the performance and stability of the OA systems and new implemented algorithms. Development of these tools is of utmost importance and represents a necessary step towards the consolidation of OA technologies in the clinics.

Appendix - Scientific contributions

Papers:

- **A. Longo,** D. Justel, V. Ntziachristos, „Disentangling the frequency content in optoacoustics", under review in IEEE Transactions on Medical Imaging, http://arxiv.org/abs/2104.14966
- **A. Longo**, S. Morscher, J. Najafababdi, D. Justel, C. Zakian, V. Ntziachristos, „Assessment of hessian-based Frangi vesselness filter in optoacoustic imaging", Photoaocsutics, vol. 20, 2020

Patent:

- S. Morscher, J. Konradl, A. Urich, **A. Longo,** P. Smole, "Probe and system for optoacoustic imaging and method for controlling such a probe", US-2020129074-A1, 2018.

Conference proceedings:

- **A. Longo**, S. Morscher, D. Justel, C. Zakian, V. Ntziachristos, "Assessment of the Hessian-based vesselness filter for vasculature enhancement in OA tomography", SPIE Photonics West, Photons Plus Ultrasound: Imaging and Sensing 2020, 1-6 February 2020, San Francisco, California, United Statess
- **A. Longo,** D. Justel, V. Ntziachristos, "Frequency content disentanglement in optoacoustic imaging", 16th European Molecular Imaging Meeting EMIM 2021, Image Processing and Quantification, 24-27 August 2021, Göttingen, Germany

Acknowledgement

I would like to thank and express my gratitude to all the people who, in different ways, have been close to me and have supported and encouraged me in this journey.

This work is the result of a jointly research collaboration between the Institute of Biological and Medical Imaging and iThera Medical GmbH, and I am grateful to have been part of both teams who have contributed to enrich me personally and professionally.

First and foremost, I would like to thank my supervisor Prof. Vasilis Ntziachristos for giving me the opportunity to work in such an inspiring and cutting-edge field which is OA. I would like to thank him for his constructive inspiring advice and for his outstanding supervision during the project.

I would like to express my sincere gratitude to my mentors Dr Christian Zakian, Dr Dominik Jüstel and Stefan Morscher, for guiding and supporting me over the PhD years, especially during the hard moments. Their encouragement and scientific support have extremely influenced the outcome of this work.

I would like to thank all the members of the Institute of Biological and Medical imaging for the insightful discussions. I would like to thank Dr. Kaushik Basak Chowdhury, Jan Kukacka, Suhanyaa Nitkunanantharajah, Christopher Dehner, Maximilian Bader, Maria Begona Rojas Lopez, Zak Ali, Parastoo Afshari, Dr. Jaeber Malekzadeh Najafababdi and Dr. Vipul Gujrati for their cooperation and their generous sharing of knowledge; Susanne Sterne, Lidia Seidl, Dr. Andreas Hillmair, Prof. Karl-Hans Englmeier and Dr. Doris Bengel for helping me with administration; Pia Anzenhofer and Sarah Glasl for their technical support; Dr. Robert Wilson and Dr. Katherine Erlich for their attentive reading and improvements of the papers and the thesis.

I would like to further express my gratitude to my colleagues in iThera Medical, Dr. Alexander Urich, Alican Kurutupe, Dr. Ami Lin, Avotra Rakotondrainibe, Awny Shammout, Edouard Coussoux, Dr. Elena Mercep, Dr. Guillaume Zahnd, Josef Konradl, Dr Katja Haedicke, Dr. Neal C. Burton, Dr. Patricia Smole, Quinn Barber, and Dr. Yi Qui. It has been an honor to be part of a such multidisciplinary team where I have learned a lot from, and I am thankful for the friendly and supportive environment in which they have surrounded me.

I am extremely grateful to the iThera management team, Christian Wiest and Dr. Philipp bell, to the European Union's Horizon 2020 research and innovation programme, and to the entire FBI consortium for giving me this unique opportunity to work on a such interesting project with extraordinary people. I would like also to acknowledge the team of Imasonic SAS for the fruitful discussions and collaboration. I thank my second supervisor Prof. Bjoern Menze for supporting me at various stages of the dissertation with critical and constructive advice.

I am lucky to have wonderful friends – Andrea Presutti, Valeria Mallozzi, Zaira Marcovecchio, Ami Lin, Awny Shammout - who have supported me with positive and constructive attitude and have made my days more carefree. I am grateful to my partner Guillermo Orozco Gijon for his kindness and caring, and for being present in the victories as well as in the failures.

Finally, I would like to thank my beloved parents Olga e Remo, and my brother Rocco, who have always been on my side encouraging me to empower myself. My successes are their successes.

I am grateful to all those people with whom I started and spent this journey, with whom I exchanged thoughts, ideas, discussions, failures, successes, and laughs, and people from whom I received positive energy. Grazie.

Bibliography

[1] A. Karlas, et al., "*Cardiovascular optoacoustics: From mice to men – A review*", Photoacoustics, vol. 14, pp. 19-30, 2019.

[2] S. V. Ovsepian, I. Olefir, G. Westmeyer, D. Rayansky, V. Ntziachristos, "Pushing the Boundaries of Neuroimaging with Optoacoustics", Neuron, vol. 96, no. 5, pp. 966-988, 2017.

[3] S. Gargiulo, S. Albanese, M. Mancini, "*State-of-the-Art Preclinical Photoacoustic Imaging in Oncology: Recent Advances in Cancer Theranostics*", Contrast Media and Molecular Imaging, vol. 3, pp.1-14, 2019.

[4] J. Xiam, L. V. Wang, "*Small-animal whole-body photoacoustic tomography: a review*", IEEE Transactions Biomedical Engineering, vol. 61, no. 5, pp. 1380-1389, 2014.

[5] J. Xia, C. Kim, J.F. Lovell, "*Opportunities for Photoacoustic-Guided Drug Delivery*", Curr. Drug Targets, vol. 16, no. 6, pp. 571-581, 2015.

[6] A. Attia, et al., "*A review of clinical photoacoustic imaging: Current and future trends*", Photoacoustics, vol. 16, 2019.

[7] S. Manohar, M. Dantuma, "Current and future trends in photoacoustic breast imaging", Photoacoustics, vol. 16, 2019.

[8] N. Nyayapathi, J. Xia, "*Photoacoustic imaging of breast cancer: a mini review of system design and image features*", Journal of Biomedical Optics, vol. 24, no. 12, 2019.

[9] J. Aguirre, M. Schwarz, D. Soliman, A. Buehler, M. Omar, V. Ntziachristos, "*Broadband mesoscopic optoacoustic tomography reveals skin layers*", Optics Letters, vol. 39, no. 21, pp. 6297-6300, 2014.

[10] M. Schwarz, A. Buehler, J. Aguirre, v. Ntziachristos, "*Three-dimensional multispectral optoacoustic mesoscopy reveals melanin and blood oxygenation in human skin in vivo*", Journal of Biophotonics, vol 1, no. 1-2, pp. 55-60, 2016.

[11] J. Aguirre, et al., "*Precision assessment of label-free psoriasis biomarkers with ultra-broadband optoacoustic mesoscopy*", Nature Biomedical Engineering, vol. 1, 0068, 2017.

[12] S. Y. Chuah, et al., "*Volumetric multispectral optoacoustic tomography for 3-Dimensional reconstruction of skin tumors: a further evaluation with histopathologic correlation*", J. Invest Dermatol., vol. 139, no. 2, pp. 481-485, 2019.

[13] A. Taruttis, et al., "*Optoacoustic imaging of human vasculature: feasibility by using a handheld probe*", Radiology, vol. 281, no. 1, 2016.

[14] M. Masthoff, et al., "*Use of multispectral optoacoustic tomography to diagnose vascular malformations*", JAMA Dermatology, vol. 154, no. 12, pp. 1457-1462, 2018.

[15] J. Jo, et al, "*Photoacoustic tomography for human musculoskeletal imaging and inflammatory arthritis detection*", Photoacoustics, vol. 12, pp. 82-89, 2018.

[16] A. P. Regensburger, et al., "*Detection of collagens by multispectral optoacoustic tomography as an imaging biomarker for Duchenne muscular dystrophy*", Nature Medicine, vol. 25, no. 12, pp. 1905-1915, 2019.

[17] F. Knieling, et al., "*Multispectral optoacoustic tomography for assessment of Crohn's disease activity*", New England Journal of Medicine, vol. 376, no. 13, pp. 1292-1294, 2017.

[18] M. J. Waldner, et al., "*Multispectral optoacoustic tomography in Crohn's disease: noninvasive imaging of disease activity*", Gastroenterology, vol. 151, no. 2, pp. 238-250, 2016.

[19] A. Karlas, M. A. Pleitez, J. Aguirre, V. Ntziachristos, "*Optoacoustic imaging in endocrinology and metabolism*", Nat. Rev. Endocrinology, vol. 17, no. 6, pp. 323-335, 2021.

[20] N. A. Fasoula, et al., "*Multicompartmental Non-invasive Sensing of Postprandial Lipemia in Humans with Multispectral Optoacoustic Tomography*", Molecular Metabolism, vol. 47, 2021.

[21] Y. Qu, et al., "*Transvaginal fast-scanning optical-resolution photoacoustic endoscopy*", J. of Biomedical Optics, vol. 23, no. 12, 121617, 2018.

[22] A. Rosenthal, V. Ntziachristos, D. Razansky, "*Acoustic Inversion in Optoacoustic Tomography: A Review*", Curr. Med. Imaging Rev., vol. 9, no. 4, pp. 318-336, 2013.

[23] B. T. Cox, J. G. Laufer, P.C. Beard, S. R. Arridge, "*Quantitative spectroscopic photoacoustic imaging: a review*" J. of Biomedical Optics, vol. 17, no. 6, 061202, 2012.

[24] A. Trauttis, V. Ntziachristos, "*Advances in real-time multispectral optoacoustic imaging and its applications*", Nature Photonics, vol. 9, pp. 219-227, 2015.

[25] V. Ntziachristos, D. Razansky, "*Molecular imaging by means of multispectral optoacoustic tomography (MSOT)*", Chem. Rev, vol. 110, no. 5, pp. 2783-94, 2010.

[26] A. Sun, H. Guo, Q. Gan, L. Yang, Q. Liu, L. Xi, "*Evaluation of visible NIR-I and NIR-II light penetration for photoacoustic imaging in rat organs*", Optics Express, vol. 28, no. 6, pp. 9001-9013, 2020.

[27] P. K. Upputuri, M. Pramanik, "*Recent advances in photoacoustic contrast agents for in vivo imaging*", WIREs Nanomedicine and Nanobiotechnology, vol. 12, no. 4, 2020.

[28] G. J. Diebold, T. Sun, m. Khan, "*Photoacoustic monopole radiation in one, two, and three dimensions*", Phys Rev Lett., vol. 67, no. 24, pp. 3384-3387, 1991.

[29] A. Rosenthal, D. Razansky, V. Ntziachristos, "*Fast semi-analytical model-based acoustic inversion for quantitative optoacoustic tomography*", IEEE transactions on medical imaging, vol. 29, no. 6, pp. 1275-1285, 2010.

[30] L. V. Wang, H. I. Wu, "*Biomedical Optics: Principles and Imaging*", Wiley-Interscience, 2007.

[31] T. Szabo, "*Diagnostic Ultrasound Imaging: Inside Out*", Academic Press, 2013.

[32] X. L. Deán-Ben, V. Ntziachristos, D. Razansky, "*Effects of small variations of speed of sound in optoacoustic tomographic imaging*", Med Phys. Vol. 41, no. 7, 2014.

[33] X. L. Deán-Ben, D. Razansky, V. Ntziachristos, "*The effects of acoustic attenuation in optoacoustic signals*", Phys Med Biol., vol. 56, no. 18, pp. 6129-48, 2011.

[34] A. B. Buhler, "*Multi-Spectral Optoacoustic Tomography: Methods and Applications*", Thesis dissertation, TUM, 2013.

[35] D. Razansky, "*Multispectral Optoacoustic Tomography—Volumetric Color Hearing in Real Time*", IEEE Journal of Selected Topics in Quantum Electronics, vol. 18, no. 3, PP. 1234-1243, 2012.

[36] Laser Institute of America. American national standard for safe use of lasers. 2000; Z136:1–2000.

[37] C. Li, L. V. Wang, "*Photoacoustic tomography and sensing in biomedicine*", Phys Med Biol, vol. 54, no. 19, pp. 59-97, 2009.

[38] G. Wissmeyer, M. A. Pleitez, A. Rosenthal, V. Ntziachristos, "*Looking at sound: optoacoustics with all-optical ultrasound detection*", Light: Science and Applications, vol 7, no. 53, 2018.

[39] A. M. Winkler, K. Maslov, L. V. Wang, "*Noise-equivalent sensitivity of photoacoustics*", J. of Biomedical Optics, vol. 18, no. 9, 2013.

[40] R. O. Esenaliev, A.A. Karabutov, A.A. Oraevsky, "*Sensitivity of laseropto-acoustic imaging in detection of small deeply embedded tumors*", IEEE Journal of Selected Topics in Quantum Electronics, vol. 5, no. 4, pp. 981-988, 1999.

[41] Y. Qui, et al., "*Piezoelectric micromachined ultrasound transducer (PMUT) arrays for integrated sensing, actuation and imaging*", Sensors, vol. 15, pp. 8020-8041, 2015.

[42] B. T. Khuri-Yakub, O. Oralkan, "*Capacitive micromachined ultrasonic transducers for medical imaging and therapy*", J. Micromech Microeng., vol. 21, no. 5, pp. 54004-54014, 2011.

[43] W. A. Smith, "*Piezocomposite Materials for Acoustical Imaging Transducers*", Jones J.P. (eds) Acoustic Imaging, Springer, Boston, vol. 21.

[44] G. Fleuty, C. Gondard, "*Improvements of ultrasonic inspections through the use of piezocomposite transducers*", 6th European Conference on Non Destructive Testings, VOL. 1, no. 9, 1996.

[45] M. Omar, et al., "*Pushing the optical imaging limits of cancer with multi-frequency-band raster-scan optoacoustic mesoscopy (RSOM)*", Neoplasia, vol. 17, no. 2, pp. 208-214, 2015.

[46] T.D. Khokhlova, I.M. Pelivanov, A.A. Karabutov, "*Optoacoustic tomography utilizing focused transducers: The resolution study*", Applied Physics Letters, vol. 92, no. 2, 2008.

[47] G. Paltauf, R. Nuster, "*Artifact removal in photoacoustic section imaging by combining an integrating cylindrical detector with model-based reconstruction. Journal of Biomedical Optics*", J. of Biomedical Optics, vol. 19, no. 2, 2014.

[48] K. P. Kostli, P. C. Beard, "*Two-dimensional photoacoustic imaging by use of Fourier-transform image reconstruction and a detector with an anisotropic response*", Applied Optics, vol 42, no. 10, pp. 1899-908, 2003.

[49] A. Rosenthal, V. Ntziachristos and D. Razansky, "*Model-based optoacoustic inversion with arbitrary-shape detectors*", Medical Physics, vol. 38, no. 7, pp. 4285-95, 2011.

[50] J. A. Jensen, N. B. Svendsen, "*Calculation of pressure fields from arbitrarily shaped, apodized and excited ultrasound transducers*", IEEE Trans Ultrason Ferroelectr Freq Control, vol. 39, no. 2, pp. 262-267, 1992.

[51] M. Xu, L.V. Wang, "*Analytic explanation of spatial resolution related to bandwidth and detector aperture size in thermoacoustic or photoacoustic reconstruction*", Physical Review E, vol. 67, 2003.

[52] A. Dima, N.C. Barton, V. Ntziachristos, "*Multispectral optoacoustic tomography at 64, 128, and 256 channels*", J of Biomedical Optics, vol 19, no. 3, 2014.

[53] S.L. Jacques, B. W. Pogue, "*Tutorial on diffuse light transport*", J. of Biomedical Optics, vol. 13, no. 4, 2008.

[54] W.C. Vogt, C. Jia, K. A. Wear, B. S. Garra, T. J. Pfefer, "*Biologically relevant photoacoustic imaging phantoms with tunable optical and acoustic properties*", J of Biomedical Optics, vol. 21, no. 10, 2016.

[55] S. L. Jacques, "*Optical Properties of Biological Tissues: A Review*", Physics in Medicine and Biology, vol. 58, no. 11, 2013.

[56] M. Xu and L. V. Wang, "*Universal back-projection algorithm for photoacoustic computed tomography*", Physical Review E., vol. 71, no. 1, 016706, 2005.

[57] K. E. Thomenius, "*Evolution of ultrasound beam formers*", IEEE Int. Ultrasonics Symposium, vol. 2, pp. 1615–1622, 1996.

[58] A. Rosenthal, D. Razansky and V. Ntziachristos," *Fast semi-analytical model-based acoustic inversion for quantitative optoacoustic tomography*", IEEE Transactions on Medical Imaging, vol. 29, no. 6, pp. 1275-1285, 2010.

[59] X. L Deán-Ben, V. Ntziachristos and D. Razansky, "*Acceleration of optoacoustic model-based reconstruction using angular image discretization*", IEEE Transactions on Medical Imaging, vol. 31, no. 5, pp. 1154-1162, 2012.

[60] K. C. Chowdhury, M. Bader, C. Dehner, D. Jüstel, and V. Ntziachristos," *Individual transducer impulse response characterization method to improve image quality of array-based handheld optoacoustic tomography*", Optics Letters, vol. 46, no. 1, pp. 1-4, 2021.

[61] K. Wang, et al., "*An imaging model incorporating ultrasonic transducer properties for three-dimensional optoacoustic tomography*", IEEE Trans. Med Imaging, vol. 30, no. 2, pp. 203-214, 2011.

[62] K.B. Chowdhury, J. Prakash, A. Karlas, D. Justel, V. Ntziachristos, "*A Synthetic Total Impulse Response Characterization Method for Correction of Hand-Held Optoacoustic Images*", IEEE Transactions on Medical Imaging, vol. 39, no. 10, pp. 3218-3230, 2020.

[63] C. Huang, K. Wang, L. Nie, L. V. Wang, "*Full-Wave Iterative Image Reconstruction in Photoacoustic Tomography With Acoustically Inhomogeneous Media*", IEEE Transactions on Medical Imaging, vol. 32, no. 6, pp. 1097-1110, 2013.

[64] S. Bu, et al., "*Model-Based Reconstruction Integrated With Fluence Compensation for Photoacoustic Tomography*", IEEE Transactions Biomedical Engineering, vol. 59, no. 5, pp. 1354-63, 2012,

[65] L. Ding, et al., "*Efficient non-negative constrained model-based inversion in optoacoustic tomography*", Physics in Medicine and Biology, vol. 60, no. 17, pp. 6733-50, 2015.

[66] S. Tzoumas, V. Ntziachristos, "*Spectral unmixing techniques for optoacoustic imaging of tissue pathophysiology*", Philo Trans A Math Phys Eng ScI, vol. 375, NO. 2107, 2017.

[67] S. Tzoumas, N. Deliolanis, S. Morscher, V. Ntyiachristos, "*Un-mixing Molecular Agents from Absorbing Tissue in ultispectral Optoacoustic Tomography*", IEEE Transactions in Medical Imaging, vol. 33, no. 1, 2014.

[68] D. Razansky, et al., "*Multispectral opto-acoustic tomography of deep-seated fluorescent proteins in vivo*", Nature Photonics, vol. 3, no. 7, 2009.

[69] A. Samykutty, A. Thomas, M. McNally, A. Chiba, L. R. McNally, "*Osteopontin-targeted probe detects orthotopic breast cancers using optoacoustic imaging* ", Biotech Histochem, vol. 93, no. 8, pp. 608-614, 2018.

[70] N. C. Burton, et al., "*Multispectral opto-acoustic tomography (MSOT) of the brain and glioblastoma characterization*", NeuroImage, vol. 65, pp. 522-528, 2013.

[71] I. Olefir, W. Mercep, N. C. Burton, S. V. Ovsepian, V. Ntziachristos, "*Hybrid multispectral optoacoustic and ultrasound tomography for morphological and physiological brain imaging*", J. of Biomedical Optics, vol. 21, no. 8, 2016.

[72] C. Wu, Y. Zhang, Z. Li, C. Li, Q. Wang, "*A novel photoacoustic nanoprobe of ICG@PEG-Ag2S for atherosclerosis targeting and imaging in vivo*", Nanoscale, vol. 25, 2016.

[73] Y. Pan, et al., "*Annexin V-Conjugated Mixed Micelles as a Potential Drug Delivery System for Targeted Thrombolysis*", Biomacromolecules, vol. 18, no. 3, pp. 865-876, 2017.

[74] W. Li et al., "*Fast Noninvasive Measurement of Brown Adipose Tissue in Living Mice by Near-Infrared Fluorescence and Photoacoustic Imaging*", Analytical Chemistry, vol. 92, no. 5, pp. 3787-3794, 2020.

[75] N. Bhutani, et al., "*Noninvasive Imaging of Colitis Using Multispectral Optoacoustic Tomography*", The Journal of Nuclear Medicine, vol. 58, no.6, pp. 1009-1012, 2017.

[76] N. Beziere, et al., "*Optoacoustic imaging and staging of inflammation in a murine model of arthritis*", Arthritis Rheumatl, vol. 66, no. 8, pp. 2071-8, 2014.

[77] N-Y. Kang, et al., "*A macrophage uptaking near-infrared chemical probe CDnir7 for in vivo imaging of inflammation*", Chemical Communications, vol. 50, 2014.

[78] I. Stoffels, et al., "*Metastatic status of sentinel lymph nodes in melanoma determined noninvasively with multispectral optoacoustic imaging Metastatic status of sentinel lymph nodes in melanoma determined noninvasively with multispectral optoacoustic imaging*", Science Translational Medicine, vol. 7, no. 317, 2015.

[79] Y. Goh; et al., "*Multispectral Optoacoustic Tomography in Assessment of Breast Tumor Margins During Breast-Conserving Surgery: A First-in-human Case Study*", Clin Breast Cancer, vol. 18, no. 6, pp. 1247-1250, 2018.

[80] G. Balasundaram, et al., "*Optoacoustic characterization of breast conserving surgery specimens – A pilot study*", Photoacoustics, vol. 19, 2020.

[81] A. Dima, V. Ntziachristos, "*Non-invasive carotid imaging using optoacoustic tomography*", Optics Express vol. 20, no. 22, pp. 25044-25057, 2012.

[82] A. Dima, V. Ntziachristos, "*In-vivo handheld optoacoustic tomography of the human thyroid*", Photoacoustics, vol. 4, no. 2, pp. 65-69, 2016.

[83] M. J. Moore, et al., "*Photoacoustic F-Mode imaging for scale specific contrast in biological systems",* Communication Physics, vol. 2, no. 30, 2019.

[84] Y. Bai, B. Cong, X. Gong, L. Song, C. Liu, "*Compact and low-cost handheld quasibright-field linear-array probe design in photoacoustic computed tomography*", J of Biomedical Optics, vol. 23, no. 12, 2018.

[85] T. Sowers, H. Yoon, S. Emelianov, "*Investigation of light delivery geometries for photoacoustic applications using Monte Carlo simulations with multiple wavelengths, tissue types, and species characteristics*", J. of Biomedical Optics, vol. 25, no.1, 2020 .

[86] J. Laufer, E. Zhang, G. Raivich, P. Beard, "*Three-dimensional noninvasive imaging of the vasculature in the mouse brain using a high resolution photoacoustic scanner*", App Opt, vol. 48, no. 10, 2009.

[87] A. Ron, X. L Deán-Ben, S. Gottschalk, D. Razansky, "*Volumetric Optoacoustic Imaging Unveils High-Resolution Patterns of Acute and Cyclic Hypoxia in a Murine Model of Breast Cancer*", Cancer Research, vol. 79, no. 18, 2019.

[88] S. Liu, et al., "*Development of a Handheld Volumetric Photoacoustic Imaging System With a Central-Holed 2D Matrix Aperture*", IEEE Transaction on Biomedical Imaging, vol. 67, no. 9, pp. 2482-2489, 2020.

[89] K. Nagae, et al., "*Real-time 3D Photoacoustic Visualization System with a Wide Field of View for Imaging Human Limbs*", F1000 Research, vol. 7, 2018.

[90] L. Lin, et al., "*High-speed three-dimensional photoacoustic computed tomography for preclinical research and clinical translation*", Nature Communications, vol. 12, no. 882, 2021.

[91] L. Lin, et al., "*Single-breath-hold photoacoustic computed tomography of the breast*", Nature Communications, vol. 9, no. 2352, 2018.

[92] Y.-J. lee, et al., "*Photoacoustic imaging probe for detecting lymph nodes and spreading of cancer at various depths*", J. of Biomedical Optics, vol. 22, no. 9, 2017.

[93] Y. Wang, R. S. A. Lin, H. Zhang, N. Nyayapathi, K. W.Oh, J. Xia, "*Optimizing the light delivery of linear-array-based photoacoustic systems by double acoustic reflectors*", Scientific Reports, vol. 8, no. 13004, 2018.

[94] K. Sivasubramanian, V. Periyasamy, K. K. Wen, M. Pramanik, "*Optimizing light delivery through fiber bundle in photoacoustic imaging with clinical ultrasound system: Monte Carlo simulation and experimental validation*", J. of Biomed Optics, vol. 22, no. 4, 2017.

[95] D. Marti, R. N. Aasbjerg, P. E. Andersen, A. K. Hansen, "*MCmatlab: an open-source, user-friendly, MATLAB-integrated three-dimensional Monte Carlo light transport solver with heat diffusion and tissue damage*", J. of Biomedical Optics, vol. 23, no. 12, pp. 1-6, 2018.

[96] N. A. Rejesh, H. Pullagurla, M. Pramanik, "*Deconvolution-based deblurring of reconstructed images in photoacoustic/thermoacoustic tomography*", Journal of the Optical Society of America, vol. 30, no. 10, pp. 1994-2001, 2013.

[97] D. V. de Sompel, L. S. Sasportas, J. V. Jokerst, S. G. Gambhir, "*Comparison of Deconvolution Filters for Photoacoustic Tomography*", PLoS one, vol. 11, no. 3, 2016.

[98] K. Mitsuhashi, K. Wang, M. A. Anastasio, "*Investigation of the far-field approximation for modeling a transducer's spatial impulse response in photoacoustic computed tomography*", Photoacoustics, vol. 2, no. 1, pp. 21-32, 2014.

[99] H. N. Y. Nguyen, W. Steenbergen, “Three-dimensional view of out-of-plane artifacts in photoacoustic imaging using a laser-integrated linear-transducer-array probe”, Photoacoustics, vol. 19, 2020.

[100] G. Paltauf, R. Nuster, “*Artifact removal in photoacoustic section imaging by combining an integrating cylindrical detector with model-based reconstruction*”, J. of Biomedical Optics, vol. 19, no. 2, 2014.

[101] M. H. Xu and L. H. V. Wang, “*Photoacoustic imaging in biomedicine*”, Review of Scientific Instruments, vol. 77, no. 4, pp. 041101, 2006.

[102] Z. Guo, C. Li, L. Song, L. V. Wang, *“Compressed sensing in photoacoustic tomography in vivo*”, J. of Biomedical Optics, vol. 15, no. 2, 2010

[103] S. Arridge, et al., “*Accelerated High-Resolution PhotoacousticTomography via Compressed Sensing*”, Physics in Medicine and Biology, vol. 61, 2016.

[104] N. Davoudi, X. L Deán-Ben, D. Razansky, “*Deep learning optoacoustic tomography with sparse data*”, Nature machine Intelligence, vol. 1, pp. 453.460, 2019.

[105] S. Antholzer, M. Haltmeier, J. Schwab, “*Deep learning for photoacoustic tomography from sparse data”,* Inverse Problems in Science and Engineering, vol. 27, no. 7, pp. 987-1005, 2017.

[106] Y. Xu, L. V. Wang, G. Ambartsoumian, P. Kuchment, “*Reconstructions in limited-view thermoacoustic tomography*”, Medical Physics, vol. 31, no. 4, pp. 724-33, 2004.

[107] A. Buehler, A. Rosenthal, T. Jetzfellner, A. Dima, D. Razansky, V. Ntziachristos, “*Model-based optoacoustic inversions with incomplete projection data*”, Medical Physic, vol. 38, no. 3, pp. 1694-704, 2011.

[108] J. Frikel, E. T. Quinto, “*Artifacts in Incomplete Data Tomography with Applications to Photoacoustic Tomography and Sonar*”, SIAM Journal on Applied Mathematics, vol. 75, no. 2, 2014.

[109] S. Arridge, et al., “*Accelerated high-resolution photoacoustic tomography via compressed sensing*”, Physics in Medicine and Biology, vol. 61, no. 24, 2016.

[110] L. Yao, H. Jiang, “*Photoacoustic image reconstruction from few-detector and limited-angle data*”, Biomedical Optics Express, vol 2, no. 9, pp. 2649-2654, 2011.

[111] J. Frikel, M. Haltmeier, “*Efficient regularization with wavelet sparsity constraints in PAT*”, Inverse Problems, vol. 34, no. 2, 2018.

[112] A. Hauptmann, et al., "*Model-Based Learning for Accelerated Limited-View 3-D Photoacoustic Tomography*", IEEE Transaction on Medical Imaging, vol. 37, no. 6, pp. 1382-1393, 2018.

[113] S. Guan, A.A. Khan, S.Sikdar, P.Chitnis, "*Fully Dense UNet for 2D Sparse Photoacoustic Tomography Artifact Removal*", IEEE Journal of Biomedical and Health Informatics, vol. 24, no. 2, 2020.

[114] I. Y. Khoury, G. B. Avinash, "*Method for removing streak artifacts in medical imaging*", US 5987347A, 1999.

[115] C. Dehner, et al., "*Deep learning based electrical noise removal enables high spectral optoacoustic contrast in deep tissue*", arXiv:2102.12960 [eess.IV].

[116] S. Tzoumas, et al., "*Spatiotemporal denoising framework for multispectral optoacoustic imaging based on sparse signal representation*", Medical Physics, vol.41, no. 11, 2014.

[117] A. Kazakeviciute, C. J. Hui Ho, M. Olivi, "*Multispectral Photoacoustic Imaging Artifact Removal and Denoising Using Time Series Model-Based Spectral Noise Estimation*", IEEE Transaction on Medical Imaging, vol. 35, no. 9, pp. 2151-2163, 2016.

[118] K. Wang, R. Su, A. A. Oraevsky, and M. A. Anastasio, "*Investigation of iterative image reconstruction in three-dimensional optoacoustic tomography*," Physics in Medicine and Biology vol. 57, no. 17, pp. 5399-5423, 2012.

[119] R. A. Kruger, P.Liu, Y.R. Fang, C.R. Aplledorn, "*Photoacoustic ultrasound (PAUS)-reconstruction tomography*", Medical Physics, vol.22, no. 10, pp. 1605-1609, 1995.

[120] J. Xia, "*Enhancement of photoacoustic tomography by ultrasonic computed tomography based on optical excitation of elements of a full-ring transducer array*", Optics Letters, vol. 38, no. 16, pp. 3140-3142, 2013.

[121] J. Jose, et al., "*Speed-of-sound compensated photoacoustic tomography for accurate imaging*", Medical Physics, vol. 39, no. 12, pp. 7262-7271, 2012.

[122] E. Mercep, J. L. Herraiz, X. L. Deán-Ben, D. Razansky, "*Transmission–reflection optoacoustic ultrasound (TROPUS) computed tomography of small animals*", Light: Science and Applications, vol. 8, 2019.

[123] H. Yang, et al., "*Soft ultrasound priors in optoacoustic reconstruction: Improving clinical vascular imaging*", Photoacoustics, vol. 19, 2020.

[124] A. Rosenthal, D. Razansky, V. Ntziachristos, "*Quantitative optoacoustic signal extraction using sparse signal representation*", IEEE Transactions on Medical Imaging, vol. 28, no. 12, pp. 1997-2006, 2009.

[125] B.T. Cox, S.R. Arridge, P. C. Beard, "*Estimating chromophore distributions from multiwavelength photoacoustic images*", J J Opt Soc Am A Opt Image Sci Vis., vol. 26, no. 2, pp. 443-455, 2009.

[126] Y. Han et al., "*Three-dimensional optoacoustic reconstruction using fast sparse representation*", Optics Letters, vol. 42, no. 5 pp. 979-982, 2017

[127] J. Prakassh, S. Mandal, D. Razansky, V. Ntziachristos, "*Maximum entropy based non-negative optoacoustic tomographic image reconstruction",* IEEE Transactions on Biomedical Engineering, vol. 66, no. 9, pp. 2604-2616, 2019.

[128] L. Yao, H. Jiang, "*Photoacoustic image reconstruction from few-detector and limited-angle data*", Biomedical Optics Express, vol. 2, no. 9, pp. 2649-2654, 2011.

[129] A. Rosenthal, T. Jetzfellner, D. Razansky, V. Ntziachristos, "*Efficient framework for model-based tomographic image reconstruction using wavelet packets*", IEEE Transactions on medical Imaging, vol. 21, no. 7, pp. 1346-1357, 2012.

[130] J. Frikel, M. Hatlmeier, "*Efficient regularization with wavelet sparsity constraints in PAT*", Inverse Problems, vol. 34, no. 2, 2018.

[131] K. Wang, et al., "*Limited data image reconstruction in optoacoustic tomography by constrained total variation minimization*", Proceeding Volume 7899, Photons Plus Ultrasound: Imaging and Sensing, SPIE BiOS, San Francisco, California, United States, 2011.

[132] S. Chaudhuri; et al., "*Detection of blood vessels in retinal images using two-dimensional matched filters*", IEEE Transactions on Medical Imaging, vol. 8, no. 3, pp.263-269, 1989.

[133] S. Dippel, M. Stahl, R. Wiemker, T. Blaffert, "*Multiscale contrast enhancement for radiographies: laplacian Pyramid versus fast wavelet transform*", IEEE Transactions Medical Imaging, vol. 21, no. 4, pp. 343-353, 2002.

[134] A. Laine; J. Fan, W. Yang, "*Wavelets for contrast enhancement of digital mammograp*hy", IEEE Engineering in Medicine, vol. 14, n0. 15, pp. 536-550, 1995.

[135] J. V. B. Soares, et al., "*Retinal vessel segmentation using the 2-D Gabor wavelet and supervised classification*", IEEE Transactions on Medical Imaging", vol. 25, no. 9, pp. 1214-1222, 2006.

[136] K. Sun, N. Sang, "*Morphological enhancement of vascular angiogram with multiscale detected by Gabor filters*", Electronics Letters, vol. 44, no. 2, 2008.

[137] R. F. Frangi, W, J. Niessen, K. Vincken, M. A. Viergever, "*MultiscaleVessel Enhancement Filtering*", In International Conference on Medical Image Computing and Computer-Assisted Intervention – MICCAI 1998, Springer, pp. 130-137. 1998.

[138] L. Li, L. Zhu, C. Ma, L. Lin, J. Yao, L. Wang, K. Maslov, R. Zhang, W. Chen, J. Shi, and L. V. Wang, "*Single-impulse panoramic photoacoustic computed tomography of small-animal whole-body dynamics at high spatiotemporal resolution*," Nature Biomedical Engineering , vol. 1, no. 0071, May 2017.

[139] M. A. Anastasion, et al., "*Half-time image reconstruction in thermoacoustic tomography*", IEEE Transaction on Medical Imaging, vol. 24, no. 2, pp. 199-210, 2005.

[140] S. Mandal, E. Mercep, X. L. Deán-Ben, D. Razansky, "*Optimal self-calibration of tomographic reconstruction parameters in whole-body small animal optoacoustic imaging*", Photoacoustics, vol. 2, no. 3, pp. 128-136, 2014.

[141] B. T. Cox, S. kara, S. R. Arridge, P. C. Beard," *k-space propagation models for acoustically heterogeneous media: Application to biomedical photoacoustics*", J Acoust Soc Am, vol. 121, no. 6, pp. 3453-3464, 2007.

[142] X. L. Deán-Ben, V. Ntziachristos, D. Razansky, "*Artefact reduction in optoacoustic tomographic imaging by estimating the distribution of acoustic scatterers*", J Biomedical Optics, vol. 17, no. 11, 2012.

[143] M. Jaeger, J. C. Bamber, M. Frenz, "*Clutter elimination for deep clinical optoacoustic imaging using localised vibration tagging (LOVIT)*", Photoacoustics, vol. 1, no. 2, pp. 19-29, 2013.

[144] M. Jaeger, et al., "*Deformation-compensated averaging for clutter reduction in epiphotoacoustic imaging in vivo*", J. of Biomedical Optics, vol. 17, no. 6, 2012.

[145] X. L. Deán-Ben, V. Ntziachristos, D. Razansky, "*Statistical optoacoustic image reconstruction using a-priori knowledge on the location of acoustic distortions*", Applied Physics Letters, vol. 98, no. 17, 2011.

[146] X. L. Deán-Ben, R. Ma, D. Razansky, V. Ntziachristos, "*Statistical Approach for Optoacoustic Image Reconstruction in the Presence of Strong Acoustic Heterogeneities*", IEEE Transactions on Medical Imaging, vol. 30, no. 2, pp. 401-408, 2011.

[147] X. L. Deán-Ben, R. Ma, A. Rosenthal, V. Ntziachristos, D. Razansky, "*Weighted model-based optoacoustic reconstruction in acoustic scattering media*", Physics in Medicine & Biology, vol. 58, no. 2013.

[148] M. K. A. Singh, W. Steenbergen, "*Photoacoustic-guided focused ultrasound (PAFUSion) for identifying reflection artifacts in photoacoustic imaging*", Photoacoustics, vol. 3, no. 4, pp. 123-131, 2015.

[149] H. N. Nguyen, A. Hussain, W. Steenbergen, "*Reflection artifact identification in photoacoustic imaging using multi-wavelength excitation*" Biomedical Optical Expressm vol. 9, no. 10, pp. 4613-4630, 2018.

[150] S. A. Emirov, et al., "*Laser optoacoustic imaging system for detection of breast cancer*", J. of Biomedical Optics, vol. 14, no. 2, 2009.

[151] A. A. Oraevsky, et al., "*Clinical optoacoustic imaging combined with ultrasound for coregistered functional and anatomical mapping of breast tumors*", Photoacoustic, vol. 12, pp. 30-45, 2018.

[152] P. D. Kumavor, et al., "*Co-registered pulse-echo/photoacoustic transvaginal probe for real time imaging of ovarian tissue*", J. Biophotonics, vol. 6, no. 6, pp- 475-485, 2013.

[153] B. Tavakoli, P. D. Kumarov, A. Aguirre, Q. Zhu, "*Effect of Ultrasound Transducer Face Reflectivity on Light Fluence Distribution inside Turbid Medium*", J of Biomedical Optics, vol. 15, no. 4, 2010.

[154] J. Xia, W. Chen, K. Maslov, M. A. Anastasio, L. V. Wang, "*Retrospective respiration-gated whole-body photoacoustic computed tomography of mice*" J. Biomedical Optics, vol. 19, no. 1, 2014.

[155] S. Gottschalk, T. F. Fehm, X. L. Deán-Ben, V. Tsytsarev, D. Razansky, "*Correlation between volumetric oxygenation responses and electrophysiology identifies deep thalamocortical activity during epileptic seizures*", Neurophotonics, vol. 4, no. 1, 2016.

[156] A. Ron, N. Davoudi, X. L. Deán-Ben, D. Razansky, "*Self-Gated Respiratory Motion Rejection for Optoacoustic Tomography*", Applied Science, vol. 9, no. 13, 2019.

[157] A. Taruttis, A. Rosenthal, M. Kacprowicz, N. C. Burton, V. Ntziachristos, "*Multiscale Multispectral Optoacoustic Tomography by a Stationary Wavelet Transform Prior to Unmixing*", IEEE Transactions Medical Imaging, vol. 33, no. 5, pp. 1194-1202, 2014.

[158] Z. Wang, A. C. Bovik, H. R. Sheigzh, E. P. Simoncelli, "*Image quality assessment: from error visibility to structural similarity*", IEEE Transaction on Image Processing, vol. 12, no. 4, pp. 600-3612, 2004.

[159] N. Venkatanath, et al., "*Blind Image Quality Evaluation Using Perception Based Features*", 2015 Twenty First National Conference on Communications (NCC), Mumbai, India, 2015.

[160] J. Weber, P. C. Beard, S. E. Bohndiek, "*Contrast agents for molecular photoacoustic imaging*", Nature Methods, vol. 13, no. 8, pp. 635-650, 2016.

[161] P. K. Upputuri, M. Pramanik, "*Recent advances in photoacoustic contrast agents for in vivo imaging*", Wiley Interdisciplinary Reviews Nanomedicine and Nanobiotechnology, vol. 12, no. 8, 2020.

[162] W. Li, X. Chen, "*Gold nanoparticles for photoacoustic imaging*", Nanomedicine, vol. 19, no. 2, pp. 299-320, 2015.

[163] T. Oruganti, J. Laufer, and B. E. Treeby, "*Vessel Filtering of Photoacoustic Images*", in Proceedings of SPIE 8581, Photons Plus Ultrasound: Imaging and Sensing, San Francisco, California, USA, 2013.

[164] D. Soliman, G. Tserevelakis, M. Omar, and V. Ntziachristos, "*Combined label-free optical and optoacoustic imaging of model organisms at mesoscopy and microscopy resolutions*," in Proceedings of SPIE 9708, Photons Plus Ultrasound: Imaging and Sensing, San Francisco, California, USA, 2016.

[165] D. Wang, Y. Wang, W Wang, D. Luo, U. Chitgupi, J. Geng, Y. Zhou, L.Wang, J.F. Lovell, J. Xia, " *Deep tissue photoacoustic computed tomography with a fast and compact laser system*," in Biomedical Optics Express, vol. 8, no. 1 , pp. 112-123 , Dec 2016.

[166] L. Li, A.A. Shemetov, M. Baloban, P. Hu, L. Zhu, D.M. Shcherbakova, R. Zhang, J.Shi, J.Yao, L.V. Wang and V.V. Verkhusha, " *Small near-infrared photochromic protein for photoacoustic multi-contrast imaging and detection of protein interactions in vivo*", in Nature Communications, vol. 9, n0. 2734, July 2018.

[167] P. Wray, L. Lin, P. Hu, L. V. Wang and D. Paulus, "*Photoacoustic computed tomography of human extremitis*," in J. of Biomedical Optics, Vol. 24, no. 2, pp. 1-8, Feb. 2019.

[168] S. Bouattour and D. Paulus, "*Vessel Enhancement in 2D Angiographic Images*", in International Conference on Functional Imaging and Modeling of the Heart – FIMH 2007, pp. 41-49, Salt Lake City, UT, USA, 2007.